

**A NUMERICAL STUDY OF WIND TURBINE WAKES UNDER  
VARIOUS ATMOSPHERIC STABILITY CONDITIONS**

by

Shengbai Xie

A dissertation submitted to the Faculty of the University of Delaware in partial fulfillment of the requirements for the degree of Doctor of Philosophy in Ocean Engineering

Winter 2016

© 2016 Shengbai Xie  
All Rights Reserved

ProQuest Number: 10055797

All rights reserved

INFORMATION TO ALL USERS

The quality of this reproduction is dependent upon the quality of the copy submitted.

In the unlikely event that the author did not send a complete manuscript and there are missing pages, these will be noted. Also, if material had to be removed, a note will indicate the deletion.



ProQuest 10055797

Published by ProQuest LLC (2016). Copyright of the Dissertation is held by the Author.

All rights reserved.

This work is protected against unauthorized copying under Title 17, United States Code  
Microform Edition © ProQuest LLC.

ProQuest LLC.  
789 East Eisenhower Parkway  
P.O. Box 1346  
Ann Arbor, MI 48106 - 1346

**A NUMERICAL STUDY OF WIND TURBINE WAKES UNDER  
VARIOUS ATMOSPHERIC STABILITY CONDITIONS**

by

Shengbai Xie

Approved: \_\_\_\_\_  
Mark A. Moline, Ph.D.  
Director of the School of Marine Science and Policy

Approved: \_\_\_\_\_  
Mohsen Badiy, Ph.D.  
Acting Dean of the College of Earth, Ocean, and Environment

Approved: \_\_\_\_\_  
Ann L. Ardis, Ph.D.  
Interim Vice Provost for Graduate and Professional Education

I certify that I have read this dissertation and that in my opinion it meets the academic and professional standard required by the University as a dissertation for the degree of Doctor of Philosophy.

Signed: \_\_\_\_\_

Cristina L. Archer, Ph.D.  
Professor in charge of dissertation

I certify that I have read this dissertation and that in my opinion it meets the academic and professional standard required by the University as a dissertation for the degree of Doctor of Philosophy.

Signed: \_\_\_\_\_

I. Pablo Huq, Ph.D.  
Member of dissertation committee

I certify that I have read this dissertation and that in my opinion it meets the academic and professional standard required by the University as a dissertation for the degree of Doctor of Philosophy.

Signed: \_\_\_\_\_

Dana Veron, Ph.D.  
Member of dissertation committee

I certify that I have read this dissertation and that in my opinion it meets the academic and professional standard required by the University as a dissertation for the degree of Doctor of Philosophy.

Signed: \_\_\_\_\_

Charles Meneveau, Ph.D.  
Member of dissertation committee

## ACKNOWLEDGEMENTS

I wish to thank all the people who have helped me along the way of finishing my dissertation. First, I would like to thank my adviser, Dr. Cristina L. Archer. She is not only an intelligent, knowledgeable and enthusiastic expert in wind energy and meteorology, but also a trustable and always generous friend, who helped me not only in research but also in my career development and in my life. It is always joyful and inspired to work with her. Second, I would like to thank my committee members, Dr. I. Pablo Huq, Dr. Dana Veron, and Dr. Charles Meneveau, who have provided valuable insights and suggestions to my research and assistance during my education. Dr. Meneveau served several times as a referee of my job application and pre-reviewed two of the research papers mentioned here before their publications. I also would like to thank my former colleagues, Dr. Niranjana Ghaisas, Dr. Di Yang, Dr. Yi Liu and Dr. Xin Guo, and my adviser of master degree at the Johns Hopkins University, Dr. Lian Shen, for their help and training during these years. Finally, I must say thank you to my parents, Fangqing Chen and Heli Xie, and my wife, Min Tang, for their everlasting love and for everything they did to support me. My wife has sacrificed a lot to follow me from China to USA, from JHU to UD, and she did everything she could to support the family and I would like to tribute this work to her and to our lovely daughter, Ruya.

## TABLE OF CONTENTS

<b>LIST OF TABLES</b> . . . . .	<b>viii</b>
<b>LIST OF FIGURES</b> . . . . .	<b>ix</b>
<b>ABSTRACT</b> . . . . .	<b>xvi</b>
 <b>Chapter</b>	
<b>1 INTRODUCTION</b> . . . . .	<b>1</b>
<b>2 SENSITIVITY ISSUES IN FINITE-DIFFERENCE LARGE-EDDY SIMULATIONS OF THE ATMOSPHERIC BOUNDARY LAYER</b> . . . . .	<b>4</b>
2.1 Abstract . . . . .	4
2.2 Introduction . . . . .	5
2.3 Numerical Methods . . . . .	9
2.3.1 Large-eddy simulation and subgrid-scale (SGS) models . . . . .	9
2.3.2 Numerical 3-D Navier-Stokes solver using finite-difference scheme . . . . .	11
2.3.3 Treatment of the boundary conditions . . . . .	13
2.3.4 Details of simulations and problem set-up . . . . .	14
2.4 Results . . . . .	16
2.4.1 Sensitivity to SGS model and convective scheme . . . . .	16
2.4.2 Sensitivity to resolution . . . . .	22
2.4.3 Sensitivity to filter type . . . . .	26
2.5 Conclusions . . . . .	32
<b>3 SELF-SIMILARITY AND TURBULENCE CHARACTERISTICS OF WIND TURBINE WAKES IN THE NEUTRAL ABL.</b> . . . . .	<b>35</b>
3.1 Abstract . . . . .	35

3.2	Introduction . . . . .	36
3.3	WiTTS: Numerical Methods and Modeling Approaches . . . . .	40
3.3.1	Governing equations and discretization . . . . .	40
3.3.2	Actuator line model for wind turbine aerodynamics . . . . .	40
3.4	Simulation Setup . . . . .	42
3.5	WiTTS Validation . . . . .	45
3.6	Results . . . . .	48
3.6.1	Mean velocity properties . . . . .	48
3.6.2	Turbulence properties . . . . .	62
3.7	Conclusions . . . . .	68
<b>4</b>	<b>WIND TURBINE WAKES UNDER VARIOUS ATMOSPHERIC STABILITY CONDITIONS . . . . .</b>	<b>70</b>
4.1	Abstract . . . . .	70
4.2	Introduction . . . . .	70
4.3	Numerical Methods . . . . .	73
4.4	Validations of WiTTS under Various Stability Conditions . . . . .	76
4.4.1	Convective planetary boundary layer . . . . .	76
4.4.2	Stable atmospheric boundary layer: the GABLS case . . . . .	77
4.5	Atmospheric Boundary Layers without Wind Turbines . . . . .	80
4.6	Atmospheric Boundary Layers with Wind Turbines . . . . .	84
4.6.1	Single-turbine wakes . . . . .	85
4.6.2	Wind farm simulations . . . . .	100
4.7	Conclusions . . . . .	108
<b>5</b>	<b>CONCLUSIONS . . . . .</b>	<b>111</b>
	<b>BIBLIOGRAPHY . . . . .</b>	<b>113</b>
	<b>Appendix</b>	
<b>A</b>	<b>DYNAMIC SGS MODELS . . . . .</b>	<b>127</b>
A.1	Planar-averaged scale-invariant (PASI) SGS model . . . . .	127

A.2	Lagrangian-averaged scale-invariant (LASI) SGS model . . . . .	128
A.3	Lagrangian-averaged scale-dependent (LASD) SGS model . . . . .	128
A.4	Test and second test filters in the physical space . . . . .	129
<b>B</b>	<b>COPYRIGHT PERMISSION . . . . .</b>	<b>130</b>

## LIST OF TABLES

3.1	Setup details of the seven cases simulated in this study. Cases 1-6 are numerical wind tunnel experiments using the WiTTS code and Case 7 is a full-scale simulation using SOWFA. $U_{hub}$ : the mean streamwise component of velocity in the free upstream at hub-height level; $u_*$ is the friction velocity; $z_0$ : surface roughness length; $\lambda$ : tip-speed ratio of rotor; $\Omega$ : rotational speed of rotor; $C_{D,nac}$ : drag coefficient of nacelle disk; $C_T$ : thrust coefficient. . . . .	45
4.1	References for some models in the GABLS cases. . . . .	77
4.2	Some parameters of the various stability conditions. Here, $U_{hub}$ and $U_{hub}^R$ are the mean streamwise velocities at the hub height before and after the rotation, respectively, $\alpha$ is the rotation angle, and $\tau_{wall} = (\tau_{13,wall}^2 + \tau_{23,wall}^2)^{1/2}$ is the total wall shear stress. $L$ is the Obukhov length. . . . .	84

## LIST OF FIGURES

2.1	Sketch of a computational cell used in the staggered grid for: (a) resolved velocity and pressure components; (b) strain-rate-tensor components; and (c) eddy viscosity and SGS stresses. The open circles represent the points at the centres of faces, the solid circle represents the cell centre, and the triangles represent the mid-points of edges. The variables are also shown where they are computed. . . . .	12
2.2	Profiles of averaged Smagorinsky coefficient $C_{S,\Delta}$ . . . . .	17
2.3	Vertical profiles of mean streamwise velocity normalized by prescribed $u_*$ . . . . .	18
2.4	Normalized mean velocity gradient $\Phi$ in the lower part of the boundary layer. The bold dashed line represents $\Phi = 1$ . . . . .	19
2.5	Normalized vertical shear stress $\langle \tau_{13} \rangle / u_*^2$ . Bold solid line: theoretical -1 slope. . . . .	20
2.6	Normalized streamwise velocity spectra versus $k_1 z$ at different heights for (a) the LASD model, (b) the LASI model, and (c) the PASI model. Grey dashed lines: divergence form; Black solid lines: skew-symmetric form. The slopes of -1 and -5/3 are also shown as black dashed lines. . . . .	21
2.7	Normalized streamwise velocity spectra versus $k_1 z$ at heights (a) $z/H = 0.07$ , and (b) $z/H = 0.41$ . The skew-symmetric form is used in all cases. . . . .	22
2.8	Mean velocity gradient $\Phi$ for different resolutions: (a) $32 \times 32 \times 32$ , (b) $64 \times 64 \times 64$ , and (c) $96 \times 96 \times 96$ . Solid line: skew-symmetric form; Dashed line: divergence form. . . . .	23
2.9	Vertical profiles of (a) $C_{S,\Delta}$ , (b) $\beta$ vs $z/H$ , and (c) $C_{S,\Delta}$ , (d) $\beta$ vs $z/\Delta$ , for different resolutions. . . . .	25

2.10	Normalized streamwise velocity spectra versus $k_1 z$ at different heights for the LASD model with various resolutions: (a) $32 \times 32 \times 32$ , (b) $64 \times 64 \times 64$ , and (c) $96 \times 96 \times 96$ . Grey dashed lines: divergence form; Black solid lines: skew-symmetric form. The slopes of -1 and -5/3 are also shown as black dashed lines. . . . .	25
2.11	Vertical profiles of normalized mean streamwise velocity for different resolutions by using (a) LASD-box-div with $\Delta t = 0.1 s$ , (b) LASD-box-ske with $\Delta t = 0.1 s$ , (c) LASD-box-div with $\Delta t = 0.05 s$ , and (d) LASD-box-ske with $\Delta t = 0.05 s$ . . . . .	27
2.12	Vertical profiles of (a) averaged Smagorinsky coefficients $C_{S,\Delta}$ and (b) averaged scale-dependent coefficient $\beta$ . . . . .	28
2.13	Profiles of (a) mean streamwise velocity and (b) mean velocity gradient $\Phi$ using the LASD model with box filtering and Gaussian filtering. . . . .	29
2.14	Contours of instantaneous resolved streamwise velocity $\tilde{u}$ at $z = 50m$ and $t = 20000.0s$ from (a) LASD-box-ske and (b) LASD-gau-ske. . . . .	30
2.15	Vertical profiles of normalized integral length scales from LASD-box-ske and LASD-gau-ske. . . . .	31
2.16	Averaged resolved kinetic energy spectrum from LASD-box-ske filtered by using different filters at height $z = 50 m$ . . . . .	32
3.1	Cross-section airfoil element . . . . .	42
3.2	Schematic of the computational domain (not to scale) . . . . .	43
3.3	Comparison of profiles of time-averaged mean streamwise component of velocity at several downstream sections on the vertical central plane. . . . .	46
3.4	Comparison of profiles of turbulence intensity $I_x$ at several downstream sections on the vertical central plane. . . . .	47
3.5	Comparison of profiles of the kinematic shear stress $-\overline{u'w'}$ at several downstream sections on the vertical central plane. . . . .	49

3.6	Self-similarity profiles of time-averaged resolved streamwise velocity deficit in the horizontal plane at the hub height for: (a) Case 1; (b) Case 4; (c) Case 5; (d) Case 6. The velocity deficits are normalized by its value at the centerline. The y-axis is the radial coordinate $r = d/2$ normalized by the half-width $r_{\frac{1}{2}}$ at that section. . . . .	50
3.7	Contours of non-dimensional time-averaged resolved streamwise velocity deficit in the horizontal plane at hub height for (a) Case 1 and (b) Case 7. The deficit is normalized by $U_{hub}$ . . . . .	52
3.8	Self-similarity profiles of time-averaged streamwise velocity deficit in the vertical central plane for: (a) Case 1; (b) Case 4; (c) Case 5; (d) Case 6. The velocity deficits are normalized by its value at the centerline. The y-axis is the radial coordinate $r = d/2$ normalized by the half-width $r_{\frac{1}{2}}$ at that section. . . . .	53
3.9	Non-dimensional time-averaged streamwise velocity deficit at hub height with LES and with several wake models. The velocity deficits are normalized by upstream mean wind speed at hub height $U_{hub}$ . The symbols are LES results and lines are wake model results. The Barthelmie's model (Eq. 3.11) is used in (a) and $c_1 = 1.03, c_2 = -0.97$ are used for the black solid line and $c_1 = 1.07, c_2 = -1.11$ are used for the red solid line; the Jensen's model (Eq. 3.12) is used in (b); the Frandsen's model (Eq. 3.14) is used in (c); and the Bastankhah's (Eq. 3.17) model is used in (d). . . . .	56
3.10	The wake width represented by $4\sigma/D$ along the streamwise direction, where $D$ is the rotor diameter and $\sigma$ is the standard deviation of mean velocity deficit: (a) in the horizontal plane at the hub-height level, representative of horizontal wake expansion, and (b) in the vertical central plane, representative of vertical wake expansion. . . . .	57
3.11	Contours of non-dimensional mean velocity deficit of Case 1 on the cross sections at (a) $x/D=2$ , (b) $x/D=8.0$ , (c) $x/D=14.0$ and (d) $x/d=18.0$ . The velocity deficit is normalized by the maximum of deficit $\delta U_{max}$ at each section. The black solid line represents the contour line of $\delta u/\delta u_{max} = 0.136$ . The white and red dashed lines are the predicted wake boundary from the Jensen's model and the Frandsen's model, respectively. . . . .	59

3.12	Comparisons of the modified Bastankhah’s model and Bastankhah’s original model for non-dimensional time-averaged streamwise velocity deficit at hub height. The symbols are LES results and the dashed lines in (a) are from the original Bastankhah’ model and in (b) are from the modified model. . . . .	61
3.13	Turbulence intensity of Case 1: (a) streamwise component $I_x$ , (b) spanwise component $I_y$ and (c) vertical component $I_z$ . . . . .	62
3.14	The maximum added turbulence intensity $\Delta I_m$ of the LES cases v.s. the theoretical model from Crespo and Hernández (1996). . . . .	64
3.15	The added turbulence intensity at the top-tip level of rotor with comparisons of several wake models. The symbols are LES results and dashed lines are wake model results. The Quarton’s model (Eq. 3.27) is used in (a), the Crespo’s model (Eq. 3.26) is used in (b), the Hassan’s model (Eq. 3.29) is used in (c), and our new model (Eq. 3.30) is used in (d). . . . .	66
3.16	The budget of turbulent kinetic energy averaged over all WiTTS cases. TA: TKE advection by mean flow; TT: TKE transport by eddies; TP: TKE production; TD: TKE dissipation. All terms are normalized by the corresponding $u_*^3/D$ . . . . .	67
4.1	Vertical profiles of time- and horizontal-averaged (a) wind speeds, (b) potential temperature $\Theta$ , (c) normalized total momentum flux (resolved + SGS terms) and (d) total heat flux (resolved + SGS terms) of the Convective PBL using two $Pr_{SGS}$ values compared with the data from literature [1]. Note that the literature data were not available in (b) and (d). . . . .	78
4.2	Vertical profiles of time- and horizontal-averaged (a) wind speeds, (b) potential temperature $\Theta$ , (c) total momentum flux (resolved + SGS terms) and (d) total heat flux (resolved + SGS terms) of the stable ABL simulations using three $Pr_{SGS}$ values compared with the data from the GABLS cases. . . . .	79
4.3	History of $u_*$ averaged over the horizontal plane for (a) stable, (b) neutral and (c) unstable ABLs. The black dashed lines represent the starting time of performing statistics and formal simulations. . . . .	81

4.4	Vertical profiles of time- and horizontal-averaged (a) velocity components $U$ (solid lines) and $V$ (dashed lines), (b) rotated velocity components $U_R$ (solid lines) and $V_R$ (dashed lines), and (c) potential temperature $\Theta$ for stable (blue), neutral (black), and unstable (red) ABLs. The thin dashed black lines represent the top-tip, hub, and bottom-tip levels of the wind turbine, respectively. . . . .	83
4.5	Vertical profiles of time- and horizontal-averaged kinematic shear stresses (a) $-\langle u'w' \rangle$ , (b) $-\langle v'w' \rangle$ , and (c) heat flux $\langle \theta'w' \rangle$ for ABLs under various stability conditions. The thin dashed black lines represent the top-tip, hub, and bottom-tip levels of the wind turbine, respectively. . . . .	83
4.6	Contours of non-dimensional time-averaged streamwise velocity component $\bar{u}/U_{hub}$ in the vertical central plane of single turbine wakes under various stability conditions. The colored lines represent the streamwise velocity relative to $U_{in}$ , the time-averaged values at the same $(y, z)$ coordinates but at $x/D \approx -2.0$ . . . . .	86
4.7	Structures of single turbine wakes in the $y - z$ planes at several downstream locations for various stability conditions. The contours are the time-averaged streamwise velocity deficit $\Delta\bar{u}/U_{hub}$ and the velocity vectors (only lateral and vertical velocity components, i. e., $\bar{v}$ and $\bar{w}$ ) are plotted at every $3 \times 3$ points. The rotor region of the turbine is represented by the red circle. . . . .	88
4.8	Self-similarity profiles of time-averaged resolved streamwise velocity deficit of single turbine wakes under various stability conditions in the vertical central plane (left column) and in the horizontal plane at hub-height level (right column). The velocity deficits are normalized by the maximum value of each profile, and the $y$ -axis is the distance to the location where the maximum value occurs and normalized by the half-width $r_{1/2}$ . The analytical Gaussian profile is presented by the black solid line. . . . .	89
4.9	Statistics of single turbine wakes under stable (blue), neutral (black), and unstable (red) conditions, for: (a) mean streamwise velocity deficit $\Delta\bar{u}_M$ normalized by $U_{hub}$ ; (b) mean coordinates of the wake normalized by $D$ ; (c) variances normalized by $D^2$ ; and (d) skewness normalized by $D^3$ . From (b) to (d), the solid lines are variables in the lateral direction and dashed lines are in the vertical direction. . . .	92

4.10	Time-averaged resolved added TKE [ $m^2/s^2$ ] in several downstream $y - z$ planes of single turbine wakes under various stability conditions. The planes reside at $x/D = 1, 3, 5, 7, 9, 11$ and $13$ , respectively. The dashed circles show the rotor area in each plane. The maximum value of resolved added TKE over the whole domain is also shown in each case. . . . .	94
4.11	Time-averaged total kinematic shear stress $-\overline{u'w'}$ [ $m^2/s^2$ ] in several downstream $y - z$ planes of single turbine wakes under various stability conditions. The planes reside at $x/D = 1, 3, 5, 7, 9, 11$ and $13$ , respectively. The dashed circles show the rotor area in each plane.	95
4.12	Instantaneous vortical structures for single turbine wakes under various stability conditions. The iso surfaces are $Q = 0.01 \text{ s}^{-2}$ . The rotor of turbine is represented by the black solid circle, and only a portion of the computational domain is shown. . . . .	96
4.13	Contour plots of instantenous vertical velocity component $w$ [m/s] in the horizontal plane at the hub height for single turbine wakes under various stability conditions. The time instants are the same as plotted in Fig. 4.12. . . . .	98
4.14	Time-averaged potential temperature deficit $\Delta\bar{\theta}$ [K] in several downstream $y - z$ planes of single turbine wakes under various stability conditions. The planes reside at $x/D = 1, 3, 5, 7, 9, 11$ and $13$ , respectively. The dashed circles show the rotor area in each plane.	99
4.15	Contours of non-dimensional time-averaged streamwise velocity component $U/U_{hub}$ in the vertical central plane for a wind farm under various stability conditions. The colored lines represent the streamwise velocity relative to $U_{in}$ , the time-averaged upstream values at the corresponding heights. . . . .	101
4.16	Statistics of wind farm wakes under stable (blue), neutral (black), and unstable (red) conditions, for: (a) mean streamwise velocity deficit $\Delta\bar{u}_M$ normalized by $U_{hub}$ ; (b) mean coordinates of the wake normalized by $D$ ; (c) variances normalized by $D^2$ ; and (d) skewness normalized by $D^3$ . From (b) to (d), the solid lines are variables in the lateral direction and dashed lines are in the vertical direction. The thin black dashes lines represent the locations of the turbines (i.e., T2 to T5, and T1 is at $x/D = 0.0$ ). . . . .	102

4.17	Time-averaged added TKE [ $m^2/s^2$ ] in several downstream $y - z$ planes of wind farm wakes under various stability conditions. The planes reside at $x/D = 1, 4, 7, 10, 13$ and $16$ , respectively. The dashed circles show the rotor area in each plane. The maximum value of resolved added TKE over the whole domain is also shown in each case.	104
4.18	Instantaneous vortical structures for a wind farm wake under various stability conditions. The time instants are the same as shown in Fig. 4.12 and the iso surfaces $Q = 0.015 \text{ s}^{-2}$ are plotted. . . . .	105
4.19	Time-averaged potential temperature change $\Delta\theta$ [ $K$ ] in several downstream $y - z$ planes of wind farm wakes under various stability conditions. The planes reside at $x/D = 1, 4, 7, 10, 13$ and $16$ , respectively. The dashed circles show the rotor area in each plane. .	106
4.20	Time-averaged relative power extractions of the wind farm under various stability conditions: (a) absolute power and (b) relative power with respect to the first turbine. . . . .	108

## ABSTRACT

The goal of this research is to investigate the properties of wind turbine wakes and their interactions with the atmospheric boundary layer (ABL) via large-eddy simulations (LES) with special emphasis on the effects of atmospheric stability. The ABL is considered stable when the ground surface is cooler than the air, unstable when the opposite happens, and neutral when the temperature effect is negligible. In the literature, neutral conditions have been studied extensively, whereas the effects of stability have not.

A new LES code, named Wind Turbine and Turbulence Simulator (WiTTS), was developed based on finite-difference (FD) schemes. First, the code's sensitivity to numerous aspects of the FD LES, such as the subgrid-scale (SGS) model, resolution, numerical treatment of the convective term, and filter types, was analyzed by simulating a neutral ABL. It was found that the Lagrangian-averaged scale-dependent (LASD) SGS model performs better than other scale-invariant Smagorinsky-type models. Second, the WiTTS was used to study the wakes from a miniature wind turbine inside a wind tunnel, following the setup of past experimental and numerical studies. It was found that those wakes are spatially anisotropic, with lateral growth faster than the vertical. Based on this, a new wake model is proposed and the Gaussian-type self-similarity is obtained for this simplified scenario. Third, to study a more realistic ABL, the stability conditions have been considered by the Boussinesq approximation and by varying thermal conditions on the ground surface, together with a constant Coriolis force. The LES results indicate that the properties of utility-scale wind turbine wakes are strongly correlated to the stability conditions. The wake recovery is enhanced by the increased turbulence due to buoyant convection in the unstable ABL, while in the stable ABL the spreading of the wake is significantly larger in the lateral direction

than in the vertical direction. The stability-related wind veering from the Coriolis force causes noticeable distortion and skewness of the wakes, especially in the stable ABL, which leads to enhanced lateral mixing but deviations from the Gaussian-type self-similarity. The influence of wind veering is reduced in wind farm wakes compared to single-turbine case. Spatial variations of temperature are introduced mainly by the advection of wake rotation, which is more discernible in the stable ABL. Atmospheric stability also influences the power extraction of the wind farm via two factors: upstream wind speed and wake recovery rate. For the same upper-level (geostrophic) wind and surface roughness, the power is highest in the stable ABL due to strongest upstream wind, but the wake loss is minimized in the unstable ABL due to fastest wake recovery.

In conclusion, our LES results suggest that the properties of wind turbine wakes are strongly correlated to the atmospheric stability and the Coriolis force, which therefore should be taken into consideration when assessing wind power generation in a wind farm and environmental impacts of wind turbine wakes.

# Chapter 1

## INTRODUCTION

Wind energy has become one of the fastest growing and most reliable renewable energy types worldwide in the past several decades. According to the Global Wind Energy Council (GWEC), by the end of 2014, the global total installed capacity was 369.6 GW, representing a cumulative market growth of more than 16 % [2]. With the increasing demand for wind energy, both number and size of wind turbines and wind farms continuously grow, which has brought a great concern about the reduced energy efficiency due to wake losses and their impacts to local, regional and global meteorology.

Wind turbine wakes are flow regions formed after wind turbines characterised by low wind speed and high turbulence, due to conversion of kinetic energy from winds into electricity and heat. In a wind farm, for certain wind directions, the wind turbine wakes from upstream turbines interact with downstream turbines, which causes significant reduction in the total energy production [3, 4, 5, 6, 7, 8]. Moreover, some local meteorological changes, such as altered surface temperature, evaporation rate, and CO<sub>2</sub> flux, etc, have been attributed to wind turbine wakes [9, 10, 11, 12, 13, 14, 15]. Therefore, it is important to understand the properties of wind turbine wakes as well as their interactions with the downstream turbines, in order to mitigate their negative impacts on energy efficiency and the environment.

Wind turbine wakes are complex and our understanding of their properties is still poor. The wakes contain turbulent eddies with various scales, from the integral scales of roughly the rotor sizes ( $\sim O(10^2)$  m) to the Kolmogorov microscales ( $\sim O(10^{-3})$  m). The spinning of the rotor further complicates the flow structures in the wakes, because it induces helical vortices from the tips of the rotor blades as well as wake rotation

[16]. More importantly, since the turbines are located inside the lower part of the atmosphere, known as the atmospheric boundary layer (ABL), wind turbine wakes have strong interactions with the ABL properties.

The ABL itself is a complex system, affected by the interaction among various forces, e.g., pressure gradient force, Coriolis force, buoyancy force due to the vertical temperature gradient, and viscous shear force imposed by the ground topology underneath. The turbulence in the ABL is closely related to shear and buoyancy forces. Different combinations of those two mechanisms result in distinctive turbulence and mean flow characteristics in the ABL. Accordingly, the ABL can be roughly categorized into three types: stable, neutral, and unstable. In a stable ABL, which normally happens at night, the ground surface is cooler than the air. Therefore, the ABL is stratified, which suppresses the turbulence production and results in strong wind shear throughout the boundary layer. In the neutral ABL, the thermal effects are negligible, and the turbulence is solely generated by the wind shear. In the unstable ABL, which normally happens in daytime, the ground surface is warmer than the air and, as a result, strong convective turbulence is induced by the buoyancy effect and mean wind shear is reduced because of the strong mixing. Also, the balance between pressure gradient force, Coriolis force and shear forces can produce complex dynamics in the ABL, such as the Ekman spiral [17], which potentially influences wind turbine wakes. However, its impacts on wind energy have not been fully revealed yet.

The interactions between the ABL and wind turbine wakes will be studied in this dissertation by performing high-fidelity large-eddy simulations (LES). The LES is a widely used technique, where the unsteady 3d flow motions are resolved directly down to the scale of the grid spacing and the subgrid-scale (SGS) motions are modelled. Correspondingly, high-resolution results can be obtained, while acceptable computational costs are maintained. But it is also known that the LES results are sensitive to the numerical scheme and the SGS model used. In this study, an LES code, WiTTS, is developed based on high-order finite difference schemes, coupled with state-of-the-art SGS and wind turbine models. From the LES results, the following research questions

are addressed:

1) What are the mean and turbulent properties of wind turbine wakes during their propagations in the ABL? Particularly, does a self-similarity property exist in the wind turbine wakes, as widely used in current wake models?

2) How does the atmospheric stability influence wind turbine wakes and energy efficiency?

3) What are the impacts of wind turbine wakes on local meteorology, especially temperature?

These questions are discussed in three chapters, each based on research papers either published or under review. The dissertation is organized as follows. The numerical details of the flow solver in WiTTS are presented in Chapter 2, where important sensitivity tests of the finite-difference LES for the neutral ABL are performed, in order not only to give a validation of WiTTS but also to provide some guidelines for the community. This chapter was published in *Boundary-Layer Meteorology* [18]. In Chapter 3, the first research question is studied with WiTTS for an isolated wind turbine in the neutral ABL without the Coriolis force. This chapter was published in *Wind Energy* [19]. In Chapter 4, the second and third questions are addressed by simulating both a single turbine and a small wind farm under various stability conditions with the Coriolis force. This chapter will be submitted to a peer reviewed journal soon. At last, the conclusions are discussed in Chapter 5.

## Chapter 2

### SENSITIVITY ISSUES IN FINITE-DIFFERENCE LARGE-EDDY SIMULATIONS OF THE ATMOSPHERIC BOUNDARY LAYER

#### 2.1 Abstract

The neutral atmospheric boundary layer (ABL) is simulated by finite-difference large-eddy simulations (LES) with various dynamic subgrid-scale (SGS) models. The goal is to understand the sensitivity of the results to several aspects of the simulation set-up: SGS model, numerical scheme for the convective term, resolution, and filter type. Three dynamic SGS models are tested: two scale-invariant models and the Lagrangian-averaged scale-dependent (LASD) model. The results show that the LASD model has the best performance in capturing the law-of-the-wall, because the scale invariance hypothesis is violated in finite-difference LES. Two forms of the convective term are tested, the skew-symmetric and the divergence forms. The choice of the convective term is more important when the LASD model is used and the skew-symmetric scheme leads to better simulations in general. However, at fine resolutions both in space and time, the sensitivity to the convective scheme is reduced. Increasing the resolution improves the performance in general, but does not better capture the law of the wall. The box and Gaussian filters are tested and it is found that, combined with the LASD model, the Gaussian filter is not sufficient to dissipate the small numerical noises, which in turn affects the large-scale motions. In conclusion, to get the most benefits of the LASD model within the finite-difference framework, the simulations need to be set up properly by choosing the right combination of numerical scheme, resolution, and filter type.

## 2.2 Introduction

The large-eddy simulation (LES) technique is widely used in research applications where explicit resolution of three-dimensional turbulence in high-Reynolds-number flows is important. In most LES studies, the numerical grid naturally plays the role of a low-pass filter by which the flow motions are separated into two parts: large-scale motions, which can be directly resolved, and subgrid-scale (SGS) motions, which need to be parameterized in terms of SGS stresses [20, 21]. One of the most commonly used SGS models is the Smagorinsky model [22], which assumes that the grid resolution falls within the inertial subrange of turbulence; that the SGS motions are locally isotropic; and that their effects can be modelled as an eddy viscosity with a universal model coefficient (Smagorinsky coefficient). However, this assumption is problematic in specific complex flows, e.g. wall-bounded turbulence, where the grid resolution approaches some externally imposed scales at which the locally isotropic assumption does not hold. Germano et al. [23] and Lilly [24] developed a dynamic approach to obtain the Smagorinsky coefficient in different flow regions by performing additional test filtering and assuming that the coefficient is scale-invariant. Some sort of averaging is necessary to stabilize the oscillations in the resulting coefficient field. For some simple turbulent problems, spatial averaging can be performed along the directions of statistical homogeneity [23, 25, 26]. For more general turbulent flow problems where spatial homogeneity is absent, the averaging can be performed either in time or in local space [27]. Meneveau et al. [28] developed a Lagrangian averaging in time along trajectories of fluid particles such that this approach can be used for any configuration [29]. In order to mitigate the assumption of scale invariance, especially when the resolution approaches the limits of the inertial subrange [30], Porté-Agel et al. [31] and Bou-Zeid et al. [32] developed a scale-dependent approach, in which a power-law scale dependence was proposed and tested a priori using field measurements [33]. Although slight differences exist in their methods, both studies used an additional level of filtering (second test filtering) with a filter width four times that of the grid spacing.

Although Smagorinsky-type SGS models cannot capture backscatter and posit an incorrect alignment between stress and strain, they have still been widely used due to their simplicity in both concept and implementation. In most previous studies, dynamic Smagorinsky SGS models have been used in the framework of spectral or pseudo-spectral methods, where the sharp spectral filter was used as test or second test filter [31, 33, 34, 35, 36, 37, 38, 39]. Fourier-transform-based spectral methods are applicable only in homogeneous directions. Most problems of engineering interest, however, involve non-periodic boundary conditions in all three directions, and, as a result, spectral methods are less applicable. Techniques, such as introducing additional “buffer regions”, have been developed in order to impose non-periodic boundary conditions while still retaining Fourier-spectral discretization [37]. But finite-difference (FD) or finite volume (FV) schemes are widely used in many atmospheric and wind-energy models, such as the Weather Research and Forecasting (WRF) model [40], Advanced Regional Prediction System (ARPS) [41, 42], and Simulator for Wind Farm Applications (SOWFA) [7].

Compared to pseudo-spectral methods, finite difference methods in general exhibit lower accuracy due to truncation errors from discretization in the horizontal directions (in the vertical, pseudo-spectral models too use finite difference). Since truncation errors occur at high wavenumbers, they are expected to interact with the SGS modelling. Although LES with FD methods have been used to study different complex physical problems ranging from fully inhomogeneous lid-driven cavity flow [43] to reacting turbulent jets [44], as pointed out by Meneveau and Katz [30], little is still known about the interplay between numerical and modelling issues. From a priori investigations, Chow and Moin [45] pointed out that, when low-order FD schemes are used, truncation errors can be so large that they dominate over the contributions from the SGS modelling. In general, high-fidelity FD LES can be achieved in two ways: increasing the order of accuracy of the numerical methods [46] or performing extra explicit filtering [47]. The latter approach has gained much attention in the recent decade due

to its simple application to lower-order FD codes for complex flows. For example, Gullbrand and Chow [48] proposed a mixed model, where a non-linear term reconstructed from the explicit-filtered velocity field is included in addition to a Smagorinsky-type eddy viscosity model. Combined with the explicit filtering, this approach has led to satisfactory simulations of channel flows and the atmospheric boundary layer [48, 49], especially with complex surface topography [50]. On the other hand, when high-order FD schemes are used, the explicit filtering is still beneficial but only marginally, because the extra costs associated with the filtering and reconstruction process (e.g. it can be viewed as an inverse process of filtering) are not negligible. Meanwhile, the explicit filtering moves a great portion of energy from the resolved part to the subfilter-scale part, which in turn reduces the effective resolution.

Besides what is mentioned here, a large number of alternative SGS models or numerical approaches exist. Rather than a comprehensive comparison of all possible approaches, the focus of this paper is on fourth-order FD LES with dynamic Smagorinsky SGS models due to their wide use, though with a scarcity of sensitivity analyses. The interplay between numerical method, resolution, and filter type has been investigated to some extent in the context of the standard dynamic Smagorinsky SGS model. For example, Lund and Kaltenbach [47] identified problems due to numerical errors with the dynamic Smagorinsky model coupled with a standard second-order accurate scheme on a staggered grid of a turbulent channel flow at Reynolds number  $Re_\tau = 2000$ . A study at higher  $Re_\tau = 5000$  by Balaras et al. [51] using a similar numerical method and SGS model, but with a wall model to include the effect of the viscous terms that are not resolved, concluded that the dynamic Smagorinsky model gives good results even at marginal resolution. The effect of two numerical schemes and two different numerical filters, in conjunction with the standard dynamic Smagorinsky model, was studied by Najjar and Tafti [52]. They showed that the type of filter has a significant impact on the model coefficient, which, in turn, affects the LES results. They also concluded that the behaviour of the SGS model depends heavily on the numerical scheme and that the dynamical procedure is not guaranteed to provide an improvement over

the constant-coefficient Smagorinsky model with all numerical schemes. Further, a systematic investigation of the LASD model in the context of FD LES has not been carried out to date. The only attempt was reported by Kirkil et al. [50], in which several SGS models, including the LASD model, have been evaluated within the finite-difference WRF-LES model. It was shown that the LASD model performed satisfactory for the neutral ABL over flat terrain, while it had similar performance to the constant Smagorinsky model for the transverse ridge case. The dearth of systematic investigations points to the need of further studies of the interactions between numerical schemes, filters, resolution, and SGS modelling issues.

Furthermore, with the fast development of wind-energy research and application, LES has been widely used to study the interactions between the ABL and wind turbine/farm [34, 37, 7, 6]. It is crucial that the characteristics of the ABL are simulated correctly, especially when the FD or FV schemes are used (e.g., in SOWFA), before the wind turbines are considered. This paper presents a posteriori tests to analyze how SGS modelling and other numerical aspects affect the simulations of the neutral ABL in the FD framework. Although neutral conditions are rarely observed in the real world ABL, the neutral ABL is a canonical case due to its simplicity (i.e., no consideration of buoyancy), the documented log-law scaling, and the abundance of prior studies. The techniques discussed herein, coupled with a wind-turbine simulator (not shown here), serve as the core of the Wind Turbine and Turbulence Simulator (WiTTs) developed at the University of Delaware [19].

The chapter is organized as follows: Section 2 gives the numerical methods where the SGS models, finite-difference schemes, and boundary treatments are introduced, as well as the simulation set-up. Section 3 presents the results of sensitivity tests of SGS models, resolutions, numerical schemes, and filter types, while conclusions are presented in Section 4.

## 2.3 Numerical Methods

### 2.3.1 Large-eddy simulation and subgrid-scale (SGS) models

For an incompressible flow, the LES model comprises filtered Navier-Stokes equations,

$$\frac{\partial \tilde{u}_i}{\partial t} = -\tilde{u}_j \frac{\partial \tilde{u}_i}{\partial x_j} - \frac{1}{\rho} \frac{\partial \tilde{p}}{\partial x_i} - \frac{\partial \tau_{ij}}{\partial x_j} + f_i \quad (2.1)$$

with the continuity equation

$$\frac{\partial \tilde{u}_i}{\partial x_i} = 0, \quad (2.2)$$

where  $\tilde{(\cdot)}$  denotes a filtered quantity at the filter width  $\Delta$  (typically equal to the grid spacing),  $\tilde{u}_i (i = 1, 2, 3)$  is the filtered fluid velocity,  $\rho$  is the (constant) fluid density,  $\tilde{p}$  is the filtered dynamic pressure,  $\tau_{ij} = \widetilde{u_i u_j} - \tilde{u}_i \tilde{u}_j$  is the SGS stress tensor, and  $f_i$  is the body force. The molecular viscous term is ignored here considering that it is several orders of magnitude smaller than the SGS term when the Reynolds number is sufficiently high. In the equations, every term is resolved except  $\tau_{ij}$ , which is modelled by using an SGS parametrization. One of the most widely used assumptions in SGS modelling is the eddy-viscosity hypothesis, which links the deviatoric part of the SGS stress tensor  $\tau_{ij}^d$  to the filtered velocity field in a linear way,

$$\tau_{ij}^d = \tau_{ij} - \frac{1}{3} \delta_{ij} \tau_{kk} = -2\nu_r \tilde{S}_{ij}, \quad (2.3)$$

where  $\delta_{ij}$  is the Kronecker delta,  $\nu_r$  is the eddy viscosity, and  $\tilde{S}_{ij}$  is the resolved strain rate tensor

$$\tilde{S}_{ij} = \frac{1}{2} \left( \frac{\partial \tilde{u}_i}{\partial x_j} + \frac{\partial \tilde{u}_j}{\partial x_i} \right). \quad (2.4)$$

A simple relationship for the eddy viscosity was proposed by analogy to the mixing-length hypothesis [22],

$$\nu_r = \ell_S^2 |\tilde{S}| = (C_S \Delta)^2 |\tilde{S}|, \quad (2.5)$$

where  $\ell_S$  is the Smagorinsky length scale,  $C_S$  is the Smagorinsky coefficient,  $\Delta$  is the grid spacing, and  $|\tilde{S}|$  is the characteristic filtered rate of strain defined by

$$|\tilde{S}| = \left(2\tilde{S}_{ij}\tilde{S}_{ij}\right)^{1/2}. \quad (2.6)$$

For homogeneous and isotropic turbulence, Lilly [53] determined  $C_S \approx 0.17$  by using the sharp spectral filter. But for a flow with mean shear, this estimate gives excessive dissipation to the large-scale fluctuations.  $C_S$  decreases as anisotropy increases and is also a function of the mesh aspect ratio [54].

A dynamic approach based on the Germano identity (Eq. A.1 in Appendix A.1) was developed to determine  $C_S$  in different flow regions by performing a test filtering (with wider filter width) explicitly onto the resolved velocity field, assuming that  $C_S$  is scale-invariant [23]. It was found that the resulting values of  $C_S$  exhibit large fluctuations, such that averaging is necessary to overcome the problem. If the averaging is performed over a homogenous plane, the approach is called the planar-averaged scale invariant (PASI) model following Bou-Zeid et al. [32] (see Appendix A.1). Based on the PASI model, for more general inhomogeneous turbulence where a spatial average is problematic, Meneveau et al. [28] developed a weighted Lagrangian time average along the fluid trajectory. This approach is the so-called Lagrangian-averaged scale-invariant (LASI) model [32] (see Appendix A.2). However, the assumption of scale-invariance of  $C_S$ , i. e.  $\beta = 1$  where  $\beta$  is a scale-dependent coefficient (see later Eq. A.5), is questionable. It was found that  $C_S$  obtained from the later Eq. A.6 corresponds to the test filter scale  $\alpha\Delta$  rather than grid filter scale  $\Delta$  [32]. Porté-Agel et al. [31] and Bou-Zeid et al. [32] introduced scale-dependent approaches by using a second test filter at scale  $\hat{\Delta} = \alpha^2\Delta$  to calculate  $\beta$  dynamically. In the Bou-Zeid et al.'s approach, it is assumed that the dependence follows a power law, which has been verified by a priori field measurements [33]. This type of SGS model is so-called Lagrangian-averaged scale-dependent (LASD) model, and the Bou-Zeid et al.'s approach is followed herein (see Appendix A.3).

In LES with a dynamic model, as discussed earlier, the explicit filtering is performed at test or second test levels. Here, in conjunction with finite-difference methods, two filters, i. e. box (or top-hat) and Gaussian filters, are tested for their simplicity and wide use in applications (see Appendix A.4). Here, the filtering is performed in a two-dimensional manner along the horizontal directions in physical space. Following previous finite-difference LES, the trapezoidal rule is used to calculate the discrete integral [27, 51, 52]. For both box and Gaussian filters, the test filtering is performed with a width twice that of the horizontal grid spacing  $\Delta$ , and the filter width of the second test filtering is four times  $\Delta$ .

### 2.3.2 Numerical 3-D Navier-Stokes solver using finite-difference scheme

Equations 3.1 and 4.2 are solved by finite-difference schemes on a staggered grid [55]. For the resolved variables, as shown in Figs. 2.1 a and b, the velocity components are computed at the face centres of a computational cell, the off-diagonal parts of the strain-rate tensor  $\tilde{S}_{ij}$  are computed at the mid-points of the edges, and the diagonal parts of  $\tilde{S}_{ij}$  and the modified pressure  $\tilde{p}^*$  are computed at the centre of the cell, where  $\tilde{p}^*$  is defined as

$$\tilde{p}^* = \tilde{p} + \frac{1}{3}\rho\sigma_{kk}, \quad (2.7)$$

and  $\sigma_{kk}$  is the summation of the normal SGS stresses. For the SGS variables, as shown in Fig. 2.1c, the eddy viscosity  $\nu_r$  is computed at the centre of the cell together with the deviatoric normal stress components, and the deviatoric shear stress components are stored at the mid-points of the edges. The staggered storage of the SGS stress makes the calculation of the gradient term  $\partial\tau_{ij}^d/\partial x_j$  at the corresponding velocity points straightforward. Linear interpolations are used when the off-diagonal parts of  $\tilde{S}_{ij}$  are needed at the cell centres or when  $\nu_r$  are needed at the edges.

The non-linear convective term in Eqs. 3.1 are calculated at the corresponding velocity points, and can be written at least in four forms [46],

$$(Div.)_i = \frac{\partial\tilde{u}_i\tilde{u}_j}{\partial x_j}, \quad (2.8)$$

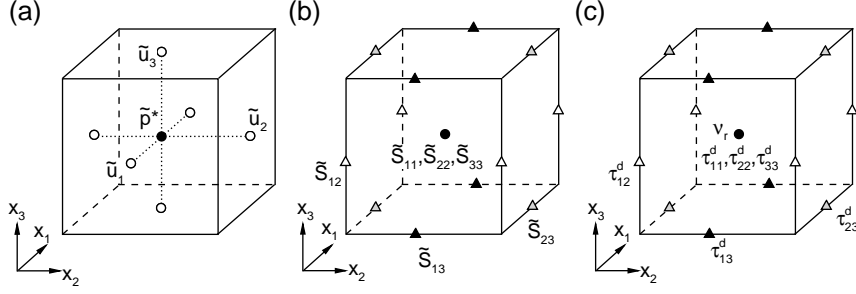


**Figure 2.1:** Sketch of a computational cell used in the staggered grid for: (a) resolved velocity and pressure components; (b) strain-rate-tensor components; and (c) eddy viscosity and SGS stresses. The open circles represent the points at the centres of faces, the solid circle represents the cell centre, and the triangles represent the mid-points of edges. The variables are also shown where they are computed.

$$(Adv.)_i = \tilde{u}_j \frac{\partial \tilde{u}_i}{\partial x_j}, \quad (2.9)$$

$$(Skew.)_i = \frac{1}{2} \left( \frac{\partial \tilde{u}_i \tilde{u}_j}{\partial x_j} + \tilde{u}_j \frac{\partial \tilde{u}_i}{\partial x_j} \right), \quad (2.10)$$

$$(Rot.)_i = \tilde{u}_j \left( \frac{\partial \tilde{u}_i}{\partial x_j} - \frac{\partial \tilde{u}_j}{\partial x_i} \right) + \frac{1}{2} \frac{\partial \tilde{u}_j u_j}{\partial x_i}, \quad (2.11)$$

where  $(Div.)_i$ ,  $(Adv.)_i$ ,  $(Skew.)_i$ , and  $(Rot.)_i$  are referred to as divergence, advective, skew-symmetric, and rotational forms, respectively. Note that  $(Skew.)_i = ((Div.)_i + (Adv.)_i)/2$  and  $(Rot.)_i = (Adv.)_i$ , so there are only two independent forms, i. e.  $(Adv.)_i$  and  $(Div.)_i$ , and they are analytically equivalent if the continuity constraint (Eq. 4.2) is satisfied strictly. However, discrepancies arise when their discrete forms are implemented numerically. Previous studies have shown that, for high-order FD schemes, the aliasing errors associated with the discrete convective term are important and that different FD treatments lead to different effects. For example, the skew-symmetric form was found to minimize the aliasing error in both spectral and FD LES [56, 57, 58] and in a priori examinations [45]. In this study, following Morinishi et al. [46], the fourth-order fully conservative discrete forms can be written as follows,

$$(Div. - S4)_i \equiv \frac{9}{8} \frac{\delta_1}{\delta_1 x_j} \left[ \left( \frac{9}{8} \overline{u_j^{1x_i}} - \frac{1}{8} \overline{u_j^{3x_i}} \right) \overline{u_i^{1x_i}} \right] - \frac{1}{8} \frac{\delta_3}{\delta_3 x_j} \left[ \left( \frac{9}{8} \overline{u_j^{1x_i}} - \frac{1}{8} \overline{u_j^{3x_i}} \right) \overline{u_i^{3x_i}} \right], \quad (2.12)$$

$$(Adv. - S4)_i \equiv \frac{9}{8} \overline{\left( \frac{9}{8} \overline{u_j^{1x_i}} - \frac{1}{8} \overline{u_j^{3x_i}} \right) \frac{\delta_1 \overline{u_i^{1x_j}}}{\delta_1 x_j}} - \frac{1}{8} \overline{\left( \frac{9}{8} \overline{u_j^{1x_i}} - \frac{1}{8} \overline{u_j^{3x_i}} \right) \frac{\delta_3 \overline{u_i^{3x_j}}}{\delta_3 x_j}}, \quad (2.13)$$

where

$$\frac{\delta_n \phi(x_1, x_2, x_3)}{\delta_n x_1} \equiv \frac{\phi(x_1 + nh_1/2, x_2, x_3) - \phi(x_1 - nh_1/2, x_2, x_3)}{nh_1} \quad (2.14)$$

is the finite-difference operator with stencil  $n$  acting on  $\phi$  with respect to  $x_1$ ,  $h_i$  is the grid spacing in the  $i$  direction, where  $S4$  denotes fourth-order accuracy at the staggered grid. Note that  $\overline{(\cdot)}$  here, and only here, represents an interpolation operator as

$$\overline{\phi}^{nx_1} \Big|_{x_1, x_2, x_3} \equiv \frac{\phi(x_1 + nh_1/2, x_2, x_3) + \phi(x_1 - nh_1/2, x_2, x_3)}{2} \quad (2.15)$$

with stencil  $n$  acting on  $\phi$  with respect to  $x_1$ . The finite-difference operator and interpolation operators in other directions can be defined straightforwardly in the same way.

As shown in Fig. 2.1, as a result of the staggering, multiple interpolations of the variables are necessary. Here, the linear interpolation is used due to its simplicity. Standard second-order central difference scheme is used in calculations of  $\tilde{S}_{ij}$  and  $\partial \tau_{ij}^d / \partial x_j$ . A fractional-step method [59] is used to update the velocity and pressure fields with the continuity constraint (Eq. 4.2) satisfied, and the second-order Adam-Bashforth scheme is used to advance in time. The Poisson equation for pressure is discretized with fourth-order accuracy, consistent with the convective term treatment, and solved using a parallelized multigrid approach with the damped Jacobian smoother [60].

### 2.3.3 Treatment of the boundary conditions

Periodic boundary conditions are used in the horizontal directions; at the top boundary, the slip condition, i. e.  $\partial \tilde{u}_i / \partial x_3 = 0, i = 1, 2$  and  $\tilde{u}_3 = 0$ , is used. At the

wall ( $z = 0$ ), a local similarity model [32] is used for the shear stress  $\tau_{i,3}^{wall}$  ( $i = 1, 2$ ) as follows,

$$\tau_{i,3}^{wall}(x, y) = \tau_w(x, y) \frac{\tilde{u}_i(x, y, \Delta_z/2)}{\sqrt{\tilde{u}_1^2 + \tilde{u}_2^2}}, i = 1, 2, \quad (2.16)$$

and

$$\tau_w(x, y) = - \left[ \frac{\kappa}{\ln\left(\frac{\Delta_z/2}{z_0}\right)} \right]^2 \left[ \tilde{u}_1(x, y, \Delta_z/2)^2 + \tilde{u}_2(x, y, \Delta_z/2)^2 \right], \quad (2.17)$$

where  $\kappa = 0.41$  is the von Kármán constant,  $z_0$  is the uniform aerodynamic roughness length, and  $\Delta_z$  is the grid spacing in the vertical direction. Although boundary conditions for  $\tilde{u}_1$  and  $\tilde{u}_3$  are not required at the wall due to the staggering, special treatment of the horizontal velocity components is still necessary in the calculation of the convective term. Here, the technique of ghost points is used to extend the velocity components outside the vertical boundaries so that the same stencil can be used in both the internal region and near the boundaries. Since fourth-order schemes with seven-point stencils are used here, three levels of ghost points are needed for each velocity component. Particularly, the no-penetration condition is used for the vertical component, i. e.  $\tilde{u}_3(-z) = -\tilde{u}_3(z)$  and  $\tilde{u}_3(z = 0) = 0$ . For the horizontal components, we use second-order linear extrapolation to obtain the ghost-point values. In practise, together with the wall model (later Eq. 2.16), we found that this boundary condition is better than the no-slip Stokes boundary condition [46], i. e.  $\tilde{u}_i(-z) = -\tilde{u}_i(z)$ ,  $i = 1, 2, 3$  (not shown).

### 2.3.4 Details of simulations and problem set-up

A neutral atmospheric boundary layer is simulated using the numerical methods discussed above. The dimensions of the simulation domain are  $L = 2000$  m,  $W = 2000$  m and  $H = 1000$  m in the  $x$ ,  $y$  and  $z$  directions ( $x_1$ ,  $x_2$  and  $x_3$  directions), respectively, where  $L$ ,  $W$  and  $H$  represent length, width, and height. We take  $z_0 = 0.1$  m and the friction velocity is prescribed as  $u_* = 0.45$  ms<sup>-1</sup>. The body force in Eq. 3.1 is set to

be a constant pressure gradient force, i. e.  $f_i = -(u_*^2/H)\delta_{i1}$  where  $\delta_{i1}$  is the Kronecker delta function, to drive the flow. Note that an alternative friction velocity can be predicted from the wall stress (Eq. 2.16), which is denoted as  $u_{*,c}$  here (subscript ‘c’ stands for ‘calculated’). It is not necessary that  $u_* = u_{*,c}$  throughout the whole simulation, but the two are supposed to be equal when the flow is fully developed and momentum conservation is well preserved. Coriolis forcing, buoyancy forcing, and molecular viscosity are neglected. The initial velocity field is given by

$$\tilde{u} = \frac{u_*}{\kappa} \ln \frac{z}{z_0} + \frac{1}{2} \varepsilon L \cos\left(\frac{2\pi x}{L}\right) \sin\left(\frac{2\pi y}{W}\right) \cos\left(\frac{2\pi z}{H}\right), \quad (2.18a)$$

$$\tilde{v} = \frac{1}{2} \varepsilon W \sin\left(\frac{2\pi x}{L}\right) \cos\left(\frac{2\pi y}{W}\right) \cos\left(\frac{2\pi z}{H}\right), \quad (2.18b)$$

$$\tilde{w} = \varepsilon H \sin\left(\frac{2\pi x}{L}\right) \sin\left(\frac{2\pi y}{W}\right) \sin\left(\frac{2\pi z}{H}\right), \quad (2.18c)$$

where  $\tilde{u}, \tilde{v}$  and  $\tilde{w}$  are resolved velocity components in the  $x, y$  and  $z$  directions, respectively, the sinusoidal functions are used for perturbation, and  $\varepsilon$  is chosen to be 0.0005. Note that the initial velocity field given by Eq. 2.18 is divergence-free. Uniform grid spacing is used in each direction and three resolutions are tested:  $32 \times 32 \times 32$ ,  $64 \times 64 \times 64$ , and  $96 \times 96 \times 96$ . The time step is fixed to be 0.1 s (the maximum Courant–Friedrichs–Lewy number is about 0.032, 0.064 and 0.096 at the three resolutions, respectively). The simulations are parallelized in the three directions by using message-passing interface technique, and 64 processors are used for each case.

Both the divergence form (Eq. 2.8) and the skew-symmetric form (Eq. 2.10) are tested for the convective term. The advective form (Eq. 2.9) is found numerically unstable in our simulations (which was also found in [58]), and the rotational form (Eq. 2.11) was reported to give large aliasing errors [45], so they are not included here. For the SGS model, three dynamic models, i. e., PASI, LASI, and LASD, are tested with both box and Gaussian filterings. Henceforth, the notation “SGS model-filter-convective form” (div: divergence form; ske: skew-symmetric form) is used to distinguish the combinations of the three aspects tested here.

## 2.4 Results

### 2.4.1 Sensitivity to SGS model and convective scheme

Different dynamic SGS models, i. e. PASI, LASI, and LASD, are tested with the box filter. Both the divergence and skew-symmetric forms are used in conjunction with each SGS model. The resolution used here is  $64 \times 64 \times 64$ . All simulations are carried out up to 45,000 s (physical time) and the last 25,000 s are used for statistics.

First, the averaged Smagorinsky coefficients  $C_{S,\Delta}$  from the different SGS models are compared in Fig. 2.2. As expected,  $C_{S,\Delta}$  varies significantly depending on the SGS model. In general, the LASD model has the maximum value by taking into account the scale dependence, while PASI and LASI models have similar predictions of smaller  $C_{S,\Delta}$ , which is consistent with previous pseudo-spectral studies [32]. The larger  $C_{S,\Delta}$  in the LASD model implies that the SGS dissipation is stronger. Note that the dependence on the choice of the convective scheme is almost negligible in the LASI and PASI models, but is apparent in the LASD model. As discussed by Chow and Moin [45], when the SGS dissipation is relatively small as in the LASI and PASI models, the numerical errors due to FD truncations can be so large that the effects of the convective form are masked. On the other hand, since more truncation errors are removed by the LASD model, the aliasing errors due to the numerical treatments of the convective form are further revealed. Therefore, the appropriate choice of the convective form is more important to the performance when the LASD model is used.

In Fig. 2.3, profiles of time- and horizontal-averaged streamwise velocity component  $U$  normalized by  $u_*$  are plotted in semi-logarithmic scales for the various SGS models together with the log law  $U = (u_*/\kappa)\ln(z/z_0)$ . The LASD model improves the prediction of the log law significantly in the near-wall region, while the LASI and PASI models poorly yield the law-of-the-wall. The superior performance of the LASD model is consistent with previous spectral studies [31, 32], suggesting that the scale dependence is important in the near-wall region where the scales of turbulence decrease quickly towards the wall and the grid resolution is coarser than that required to fully resolve the production subrange. In addition, the skew-symmetric form has a superior

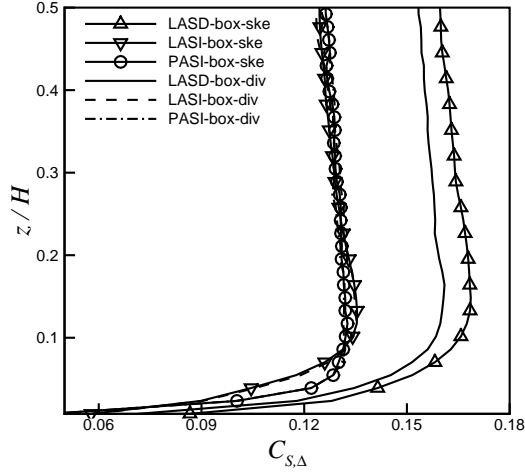


**Figure 2.2:** Profiles of averaged Smagorinsky coefficient  $C_{S,\Delta}$ .

performance to that of the divergence form when the LASD model is used, since the skew-symmetric form results in smaller aliasing errors [58, 45]. Consistent with earlier discussion, the difference due to the convective forms is less obvious in the LASI and PASI models.

In Fig. 2.4, the normalized mean velocity gradient  $\Phi(z) = (\kappa z/u_*)(\partial U/\partial z)$  is computed for all cases and plotted as a function of  $z/H$ , in which  $\Phi = 1$  represents the theoretic prediction of the law-of-the-wall. In the lower part  $z/H < 0.2$ , where the log-law is expected, the nearly constant behaviour of  $\Phi(z)$  is successfully achieved in the LASD model, although the value (approximately 1.2) is slightly overestimated (Fig. 2.4). In contrast, results with the LASI and PASI models differ more from the law-of-the-wall and the profiles of the gradient are less constant than with the LASD model. Particularly in the region very close to the wall, underestimations of the wind shear are observed in the LASI and PASI models, suggesting insufficient turbulence dissipation due to lack of consideration of the scale dependence. Furthermore, the velocity gradient is less affected by the convective scheme in the region close to the wall, but the dependence is more distinct with height in all cases.

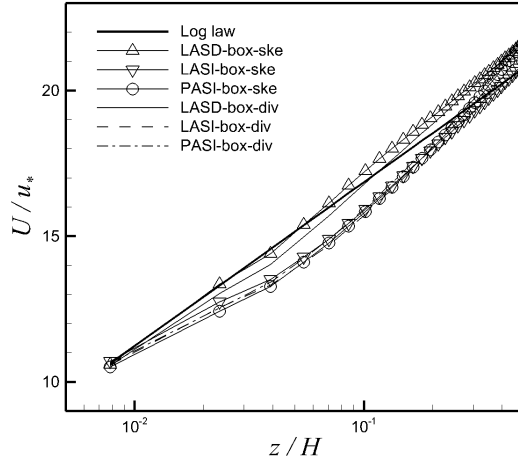


**Figure 2.3:** Vertical profiles of mean streamwise velocity normalized by prescribed  $u_*$ .

A small peak (so-called “overshoot”), which is well known for the standard Smagorinsky SGS model associated with spurious length scales introduced by numerical viscous effects [61], is observed for  $\Phi$  around  $z/H \sim 0.1$  for the LASD model, indicating that the LASD model in the FD LES slightly overestimates the dissipation near the wall; whereas it is absent in the LASI and PASI models where the dissipation is relatively small, as discussed above. The overshoot was also observed for some other SGS models used in FD LES [50], in which an additional near-wall stress term was used to improve agreement with the law-of-the-wall. In the previous studies of the LASD model using low-dissipative pseudo-spectral code, the overshoot problem was mitigated [31, 32]. In the region very close to wall, i. e. the first three points, oscillations of the gradient are observed in all cases, which are believed to be caused by the wall stress treatment [61]. Note that similar oscillations have also been observed in pseudo-spectral simulations [32].

Next, the shear stress  $\langle \tau_{13} \rangle$  is investigated, where  $\langle \cdot \rangle$  denotes averaging both in time and in each horizontal direction. Since molecular viscosity is negligible, the total shear stress  $\langle \tau_{13} \rangle$  has three parts: the resolved part  $-\langle \tilde{u}'_1 \tilde{u}'_3 \rangle$ , where  $\tilde{u}'_i = \tilde{u}_i - \langle \tilde{u}_i \rangle$  ( $i =$

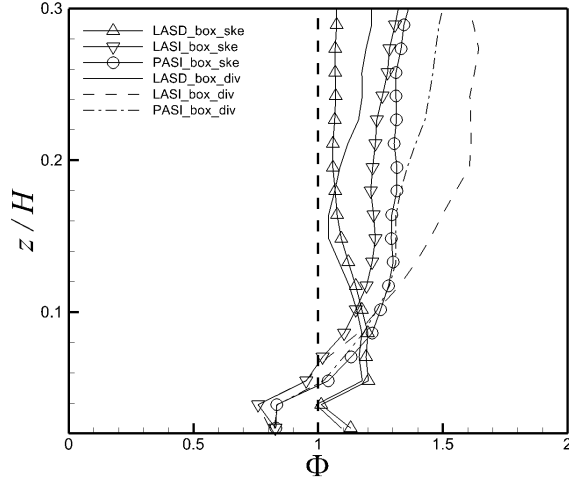


**Figure 2.4:** Normalized mean velocity gradient  $\Phi$  in the lower part of the boundary layer. The bold dashed line represents  $\Phi = 1$ .

1, 2, 3), the SGS part  $\langle \tau_{13} \rangle$ , and the wall shear stress (Eq. 2.17). Further, for a constant-pressure-driven flow without viscous effect, theoretically the vertical integration of the total averaged shear stress normalized by  $u_*^2$  yields a straight line with slope of -1, which starts from a value of 1 on the wall and ends at a value of 0 up at the top of the boundary layer. Fig. 2.5 shows the normalized total and decomposed shear stress profiles of the ABL from current simulations. The wall shear stress is included in the SGS component for the sake of plotting. In the near wall region, the contribution from each component of the shear stress varies with the SGS model, i. e. the SGS stress has the largest contribution in the LASD model, and smaller in the LASI and PASI models. Note that the LASI model has slightly smaller SGS flux than the PASI model, indicating that the Lagrangian averaging is slightly less dissipative than the planar averaging. Hence, the resolved component near the wall is smaller in the LASD model, and larger in the LASI and PASI models, since the total momentum is approximately conserved.

In Fig. 2.6, the time- and horizontal-averaged energy spectra of streamwise velocity normalized by  $u_*^2 z$  at different heights, obtained from various SGS models,

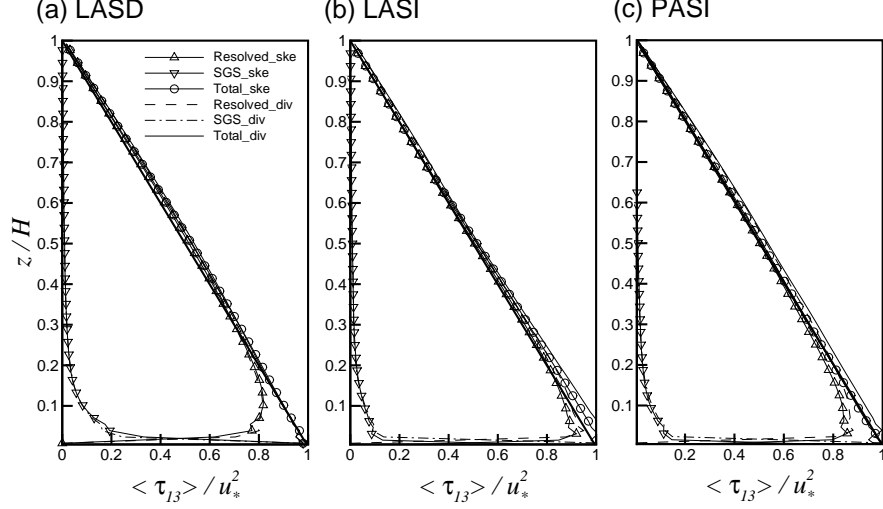


**Figure 2.5:** Normalized vertical shear stress  $\langle \tau_{13} \rangle / u_*^2$ . Bold solid line: theoretical -1 slope.

are plotted versus  $k_1 z$ , where  $k_1$  is the wavenumber in the streamwise direction. The spectra are used to evaluate the performance of the SGS models in generating turbulent structures with different length scales [50]. Previous studies [62, 31, 32, 50] pointed out that the normalized spectra at different heights collapse to a slope proportional to  $k_1^{-1}$  in the production range ( $k_1 z < 1$ ) and to  $k_1^{-5/3}$  in the inertial subrange ( $k_1 z > 1$ ). In Fig. 2.6a, the collapses in the two ranges are well captured by the LASD model regardless of the convective schemes. In Figs. 2.6 (b) and (c), the slopes are flatter than expected in the two ranges by using the LASI and PASI models, consistent with the fact that energy dissipation is underestimated if scale dependence is not considered. For the LASI and PASI models, the difference caused by the convective scheme is more noticeable. At the highest resolved wavenumbers, fast decaying of the energy occurs at all heights in all cases due to numerical dissipation associated with the finite-difference discretization, which is consistent with the observation in [50].

The averaged streamwise energy spectra at two specific heights, i.e.  $z/H = 0.07$  (close to the wall) and  $z/H = 0.41$  (away from the wall), are plotted in Fig. 2.7. The spectra are obtained by performing one-dimensional fast fourier transform (FFT)

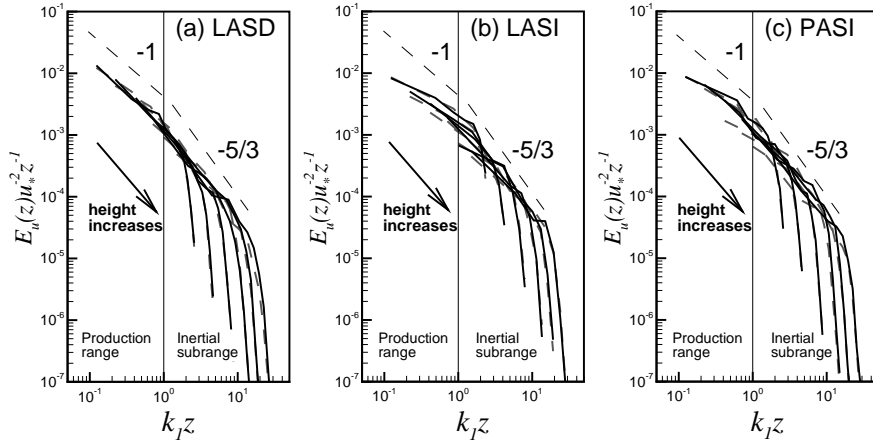


**Figure 2.6:** Normalized streamwise velocity spectra versus  $k_1 z$  at different heights for (a) the LASD model, (b) the LASI model, and (c) the PASI model. Grey dashed lines: divergence form; Black solid lines: skew-symmetric form. The slopes of  $-1$  and  $-5/3$  are also shown as black dashed lines.

to the streamwise velocity component along the x-direction and are averaged in time and in the horizontal directions. In order to show the effects of the finite-difference discretization and the smooth filtering more clearly, the results from a pseudo-spectral LES with the sharp-spectral LASD model are plotted as comparison. The pseudo-spectral LES uses the same problem set-up as the finite-difference LES, and most of the numerical details follow [32], except that the  $2/3$  rule, which simply cuts off the highest  $1/3$  of the velocity spectra, is used here for elimination of the aliasing errors [63], whereas the  $3/2$  rule was used in [32]. The skew-symmetric form is used for the convective term for the cases shown in the figure. For the pseudo-spectral cases, the production range and inertial subrange are well resolved and a sharp cut-off of the spectra is evident at  $k_1 z = 4.7$  and  $27.7$  respectively in Figs. 2.7 (a) and (b) due to the dealiasing, which separates the resolved scales (lower  $2/3$  of the spectra) and unresolved small scales (cut-off) clearly. In contrast, the separation of large-scale and small-scale motions is less abrupt in the finite-difference LES, where the spectra are smoothed near the cut-off wavenumbers. The smooth transition indicates that the

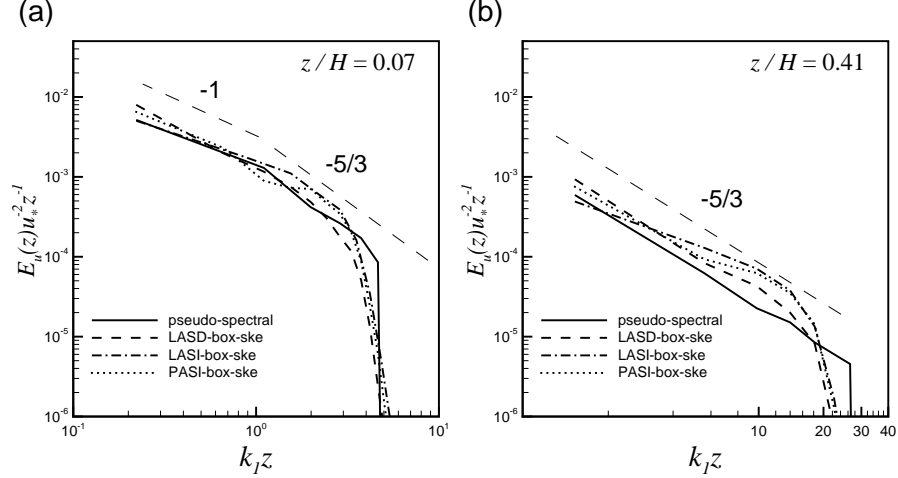


**Figure 2.7:** Normalized streamwise velocity spectra versus  $k_1 z$  at heights (a)  $z/H = 0.07$ , and (b)  $z/H = 0.41$ . The skew-symmetric form is used in all cases.

effect of the finite-difference discretization is not limited to the small-scale motions but also impacts the large-scale motions. When the LASI or PASI model is used, the  $-5/3$  slope is poorly captured at both heights near and away from the wall.

In summary, among several dynamic SGS models tested in current FD LES, the LASD model is the only one that provides sufficient dissipation to reduce numerical noise, i.e. truncation and aliasing errors, and it best captures the law-of-the-wall. However, the LASD model is more sensitive to the choice of the convective form, with the skew-symmetric form performing better than the divergence form in general. The energy spectra show that, compared to the pseudo-spectral LES, the large-scale motions are affected by the truncations of the finite-difference discretization, which further violates the assumption of scale invariance.

#### 2.4.2 Sensitivity to resolution

Next, the LASD model is tested with three different resolutions, i. e.,  $32 \times 32 \times 32$ ,  $64 \times 64 \times 64$ , and  $96 \times 96 \times 96$ , using both the divergence and skew-symmetric forms for the convective term. The box filter is used here for the test and second test filtering processes. As plotted in Fig. 2.8,  $\Phi$  predicted from  $32 \times 32 \times 32$  is relatively poor

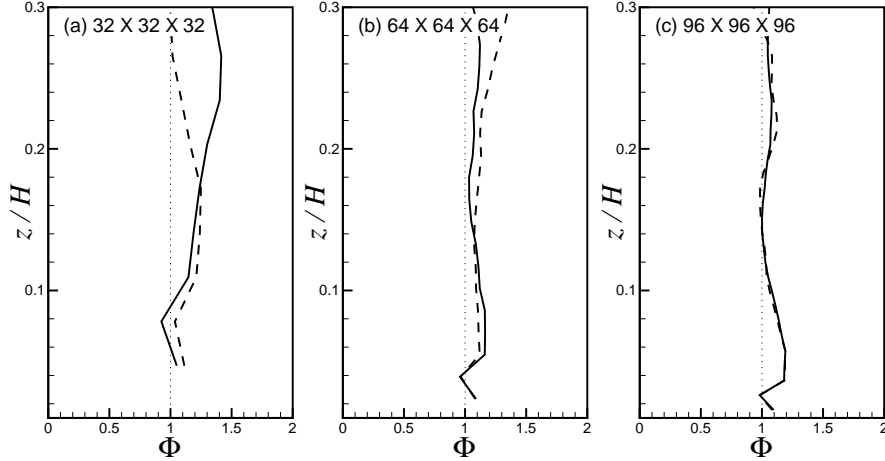


**Figure 2.8:** Mean velocity gradient  $\Phi$  for different resolutions: (a)  $32 \times 32 \times 32$ , (b)  $64 \times 64 \times 64$ , and (c)  $96 \times 96 \times 96$ . Solid line: skew-symmetric form; Dashed line: divergence form.

and depends obviously on the convective scheme. With the increase of resolution, the collapse to the log law is more apparent and the sensitivity to the convective scheme is reduced. Note that, regardless of the convective scheme, the profiles of  $\Phi$  from  $96 \times 96 \times 96$  are less constant compared to  $64 \times 64 \times 64$ , implying that the prediction of the law-of-the-wall is not necessarily improved by using higher resolution. Actually, the “overshoot” problem is more severe at higher resolution because the first few grid points extend closer to the wall, where the ratio between the dissipation from the SGS model and the inertial effect from resolved motions is further increased, which obscures the correct scaling of the law-of-the-wall [61]. As suggested by [61], adjusting the aspect ratio is more effective than only increasing the resolution in all directions to eliminate the “overshoot”, as was shown in [50] for the LASD model in the WRF model.

In Figs. 2.9 (a) and (b), the time- and horizontal-averaged Smagorinsky coefficient  $C_{S,\Delta}$  and the scale-dependent coefficient  $\beta$  are plotted vs  $z/H$  for different resolutions. Compared to the mean velocity, the SGS coefficients are more dependent on resolution, as expected, especially in the lower part of the ABL, but are insensitive to the treatment of the convective scheme. In all cases, in the region near the wall,

$C_{S,\Delta}$  decreases as height decreases towards the wall and its magnitude increases with resolution, whereas in the upper part the classic value between 0.1 and 0.22 [32] is approached asymptotically for all resolutions. The scale-dependent coefficient  $\beta$  shows a trend similar to  $C_{S,\Delta}$ . Contrary to previous spectral studies [31], which found that  $\beta$  asymptotically approaches 1 in the aloft region, the current results give a much smaller prediction of  $\beta \approx 0.6$  away from the wall, suggesting that scale dependence is important not only in the region close to the wall but also in the core region of the flow in finite-difference LES. The amplification of the scale dependence is believed to be caused by the fact that considerable large-scale motions are affected by the implicit filtering at the grid-scale level due to finite-difference discretization [64, 52] as well as the explicit filterings at the test or second test levels where a discrete smooth filter is used. From the spectral perspective, the influence of the smooth filter is not only limited in the inertial subrange but extends to the whole spectrum due to its non-local effect (see Fig. 2.16), thus the self-similarity across different scales is less valid. In Figs. 2.9 (c) and (d), the profiles of SGS coefficients are collapsed for different resolutions when they are plotted against height  $z$  normalized by the filter width  $\Delta$ , implying that both  $C_{S,\Delta}$  and  $\beta$  are dependent on scale  $\Delta$  at a certain height  $z$ . However, the scale dependence of  $\beta$  is considered to be a higher-order effect compared to that of  $C_{S,\Delta}$ , so it is still acceptable to use the scale-invariant assumption of  $\beta$  in the LASD model [31, 32].

In Fig. 2.10, the streamwise velocity spectra versus  $k_1 z$  at different heights for the LASD model at various resolutions are plotted. The spectral energies are normalized by the maximum value of the spectral energy  $E_{u,max}$  at the lowest height obtained by using the divergence form, and the spectra are cutoff at  $2/3$  of the maximum wavenumber, consistent to the dealiasing used in the pseudo-spectral code. With the resolution  $32 \times 32 \times 32$ , the -1 slope is poorly yielded due to overestimated dissipation, although it is slightly improved by using the skew-symmetric form for the convective term. For higher resolutions, both the -1 slope in the production range and the -5/3 slope in the inertial subrange are yielded reasonably well.

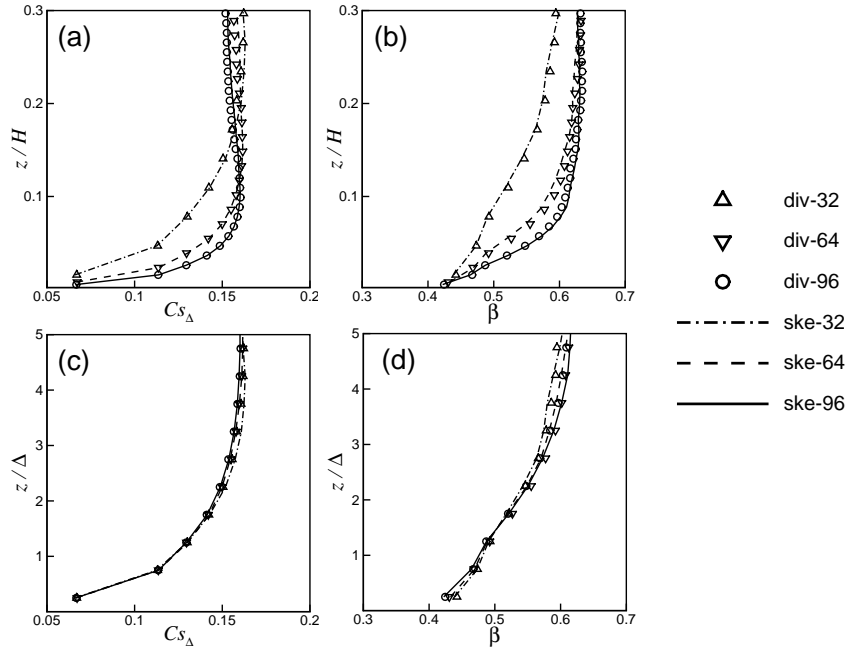


**Figure 2.9:** Vertical profiles of (a)  $C_{S,\Delta}$ , (b)  $\beta$  vs  $z/H$ , and (c)  $C_{S,\Delta}$ , (d)  $\beta$  vs  $z/\Delta$ , for different resolutions.

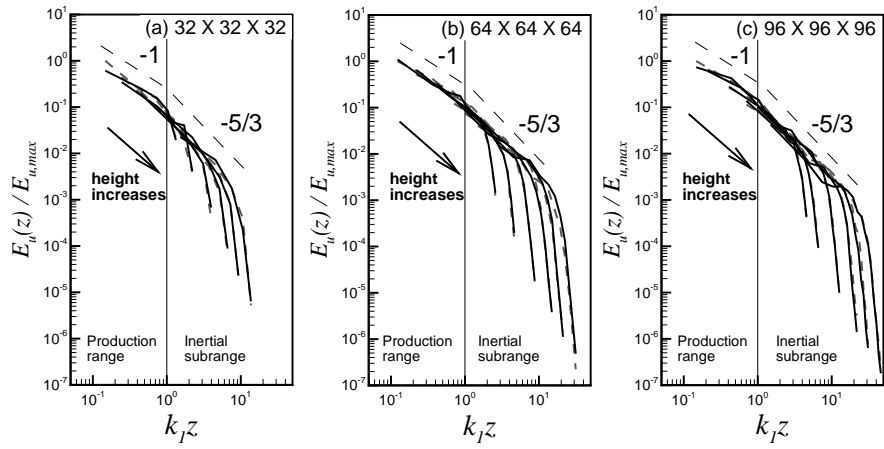


**Figure 2.10:** Normalized streamwise velocity spectra versus  $k_1 z$  at different heights for the LASD model with various resolutions: (a)  $32 \times 32 \times 32$ , (b)  $64 \times 64 \times 64$ , and (c)  $96 \times 96 \times 96$ . Grey dashed lines: divergence form; Black solid lines: skew-symmetric form. The slopes of  $-1$  and  $-5/3$  are also shown as black dashed lines.

Lastly, Fig. 2.11 shows the vertical profiles of the normalized mean streamwise velocity from each case with both time steps of  $\Delta t = 0.1$  s and  $\Delta t = 0.05$  s. Comparing Figs. 2.11 (a) and (b), the difference caused by the various convective schemes is evident when  $\Delta t = 0.1$  s; the skew-symmetric form produces a better collapse to the log law in the lower part near the wall ( $z/H < 0.1$ ). The dependence on the convective scheme can be reduced greatly by using higher temporal resolution, as plotted in Figs. 2.11 (c) and (d) where  $\Delta t = 0.05$  s is used, especially for the divergence form. Furthermore, compared to the divergence form, the skew-symmetric form appears to be less sensitive to temporal resolution (as well as spatial resolution), which makes it more robust in practical applications.

In summary, in this section, the sensitivity to resolution of finite-difference LES with the LASD model was examined. The simulations are less sensitive to resolution when the skew-symmetric form is used for the convective term. When the resolution in both space and time increases, the dependence on the convective scheme is reduced. The scale dependence of both  $C_{S,\Delta}$  and  $\beta$  is found to be significant throughout the whole flow region in the current finite-difference LES, which in turn produces the superior performance of the LASD model compared to other scale-invariant SGS models discussed in Section 2.4.1. Lower resolution has poorer performance in the production range, and higher resolution improves the prediction of the energy spectra, but higher resolution does not guarantee a better capture of the law-of-the-wall.

### 2.4.3 Sensitivity to filter type

In previous studies [31, 32], sharp spectral filtering was performed in the spectral space for the test and second test filtering processes of the LASD model. Since this paper focuses on LES using finite-difference methods, it is more straightforward to perform the filtering process in physical space. Two basic spatial filters, i. e. box filter and Gaussian filter, are examined here. Both of the skew-symmetric and divergence forms have been tested, but only the results from the skew-symmetric form are shown here.

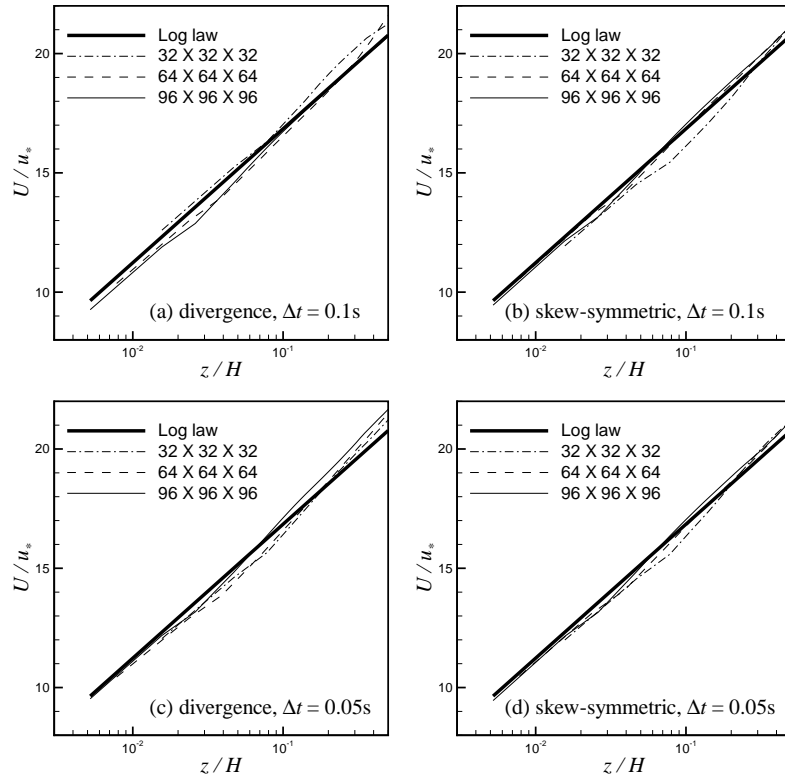


**Figure 2.11:** Vertical profiles of normalized mean streamwise velocity for different resolutions by using (a) LASD-box-div with  $\Delta t = 0.1$  s, (b) LASD-box-ske with  $\Delta t = 0.1$  s, (c) LASD-box-div with  $\Delta t = 0.05$  s, and (d) LASD-box-ske with  $\Delta t = 0.05$  s.

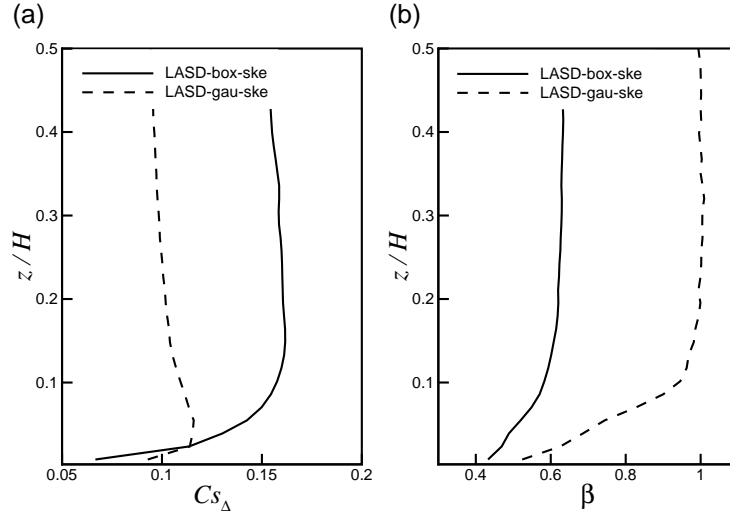


**Figure 2.12:** Vertical profiles of (a) averaged Smagorinsky coefficients  $C_{S,\Delta}$  and (b) averaged scale-dependent coefficient  $\beta$ .

The time- and horizontal-averaged  $C_{S,\Delta}$  and  $\beta$  are plotted in Fig. 2.12. It is clear that the coefficients are highly dependent on the filter type. In general,  $C_{S,\Delta}$  predicted from the Gaussian filtering is much smaller than that from the box filtering. It is interesting to notice that, for the Gaussian filtering, the expected decrease of  $C_{S,\Delta}$  is only confined in a very limited height off the wall, indicating that it fails to predict the expected behavior of the mixing length  $\lambda = C_S \Delta \sim z$  in the log-law region [65]. Meanwhile, as plotted in Fig. 2.12 (b),  $\beta$  increases almost linearly with the Gaussian filtering in the near wall region and it approximately approaches 1 in the core region of the ABL, whereas  $\beta$  is much smaller and approaches a value of about 0.6 in the core region with the box filtering, indicating a stronger scale dependence. The larger scale dependence of the box filter introduces larger  $C_{S,\Delta}$  and eventually causes larger energy dissipation by the SGS model.

With varying SGS effects due to the filter type, the resolved velocity fields also exhibit different features. For instance, the Gaussian filter produces relatively poor capture of the law-of-the-wall in term of the mean stream velocity profile (Fig. 2.13 (a)), and its normalized gradient  $\Phi$  appears to be less constant and deviates further from 1

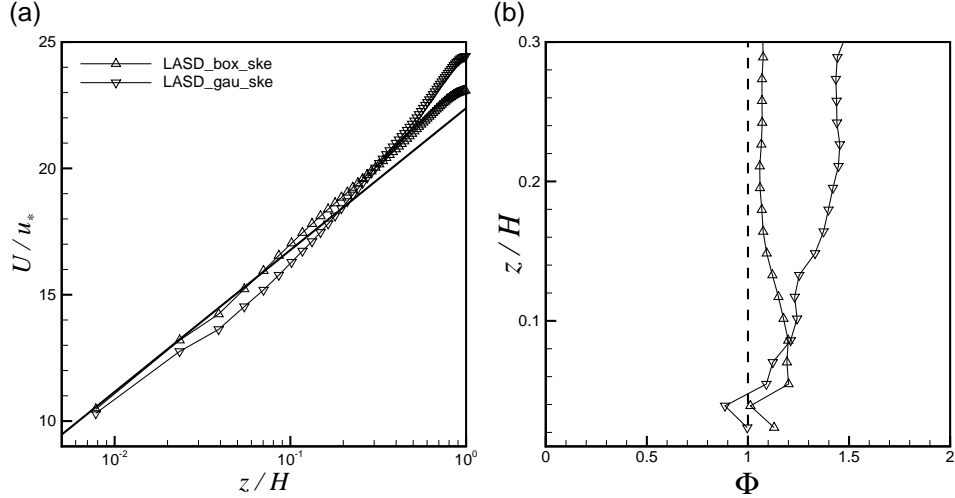


**Figure 2.13:** Profiles of (a) mean streamwise velocity and (b) mean velocity gradient  $\Phi$  using the LASD model with box filtering and Gaussian filtering.

(Fig. 2.13 (b)). As discussed in Sec. 2.4.1, the poor performance of the Gaussian filter here is attributed to insufficient SGS dissipation such that high-frequency numerical errors contaminate the flow features.

In order to visualize the effects more clearly, Fig. 2.14 shows contours of instantaneous resolved streamwise velocity component  $\tilde{u}$  at  $z = 50$  m (within the surface layer, i. e.  $z/H < 0.1$ ) and  $t = 20,000$  s from both box and Gaussian filtering. The instantaneous field from the Gaussian filtering in Fig. 2.14 (b) contains a large amount of small-scale fluctuations whose energy could not be sufficiently dissipated by the SGS model. On the other hand, when the box filtering is used (Fig. 2.14 (a)), large-scale motions, such as elongated streaky structures aligned with the streamwise direction, are clearly formed with length scale comparable to the height of the ABL [66, 67, 50], and the small-scale fluctuations are reduced. Therefore, the effects of the SGS models due to the choice of the filter type are not limited to the small scales, but also impact the simulations of some large-scale flow features.

To characterize the large eddies in the ABL, the integral length scale can be

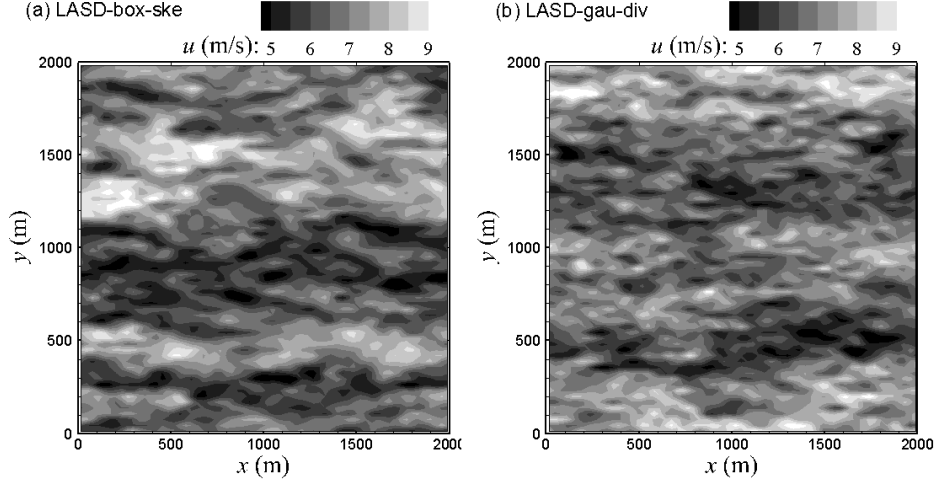


**Figure 2.14:** Contours of instantaneous resolved streamwise velocity  $\tilde{u}$  at  $z = 50m$  and  $t = 20000.0s$  from (a) LASD-box-ske and (b) LASD-gau-ske.

calculated as follows

$$L_{ij}(z) \equiv \frac{1}{R_{ij}(z, 0)} \int_0^\infty R_{ij}(z, r) dr, \quad (2.19)$$

where  $R_{ij}(z, r) \equiv \langle \tilde{u}'_i(x, y, z, t) \tilde{u}'_j(x + r, y, z, t) \rangle$  ( $i = 1, 2, 3$ ) is the two-point correlation function in the longitudinal direction, and  $\langle \cdot \rangle$  denotes horizontal and time averaging. In Fig. 2.15, the vertical profiles of  $L_{11}$  and  $L_{13}$  from both LASD-box-ske and LASD-gau-ske are plotted, where  $L_{11}$  represents the large-eddy length scales associated with streamwise momentum transport, and  $L_{13}$  represents the large-eddy length scales associated with vertical momentum transport. As expected, both length scales decrease near the wall, meaning that the eddy sizes shrink when approaching the wall. Moreover, the box filtering introduces larger  $L_{11}$  and  $L_{13}$  than the Gaussian filtering, consistent with earlier observations (Fig. 2.14) that the large scale motions are better reproduced with the box filtering case but are contaminated by small scale numerical noises in the Gaussian filtering case.

In order to show the effects of the various filters more straightforwardly, the averaged resolved kinetic energy spectrum at  $z = 50 m$  from LASD-box-ske is calculated as a function of  $kz$ , where  $k = \sqrt{k_1^2 + k_2^2}$  (Fig. 2.16). The resolved kinetic energy

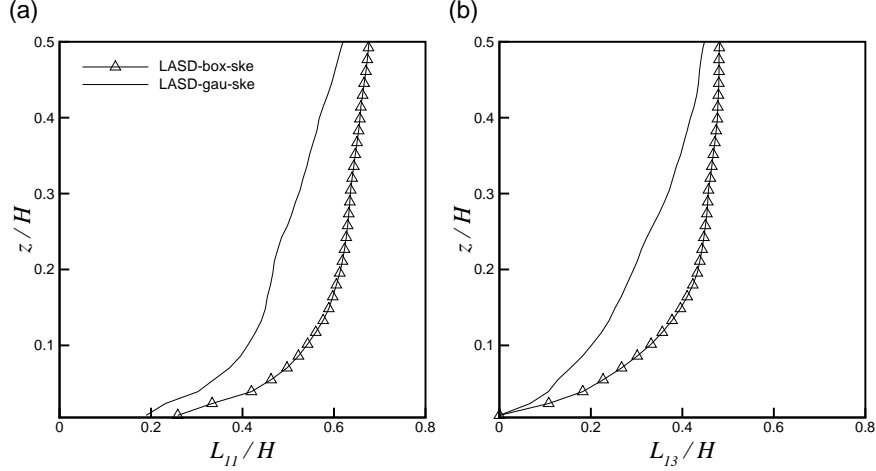


**Figure 2.15:** Vertical profiles of normalized integral length scales from LASD-box-ske and LASD-gau-ske.

spectrum  $E(k)$  at each time step is calculated by performing two-dimensional FFT to the velocity field to get the spectral energy field in the  $k_1 - k_2$  plane, then integrating the spectral energy along the circle with radius equal to  $k$ . The test and second test filtering approaches are performed on the velocity field by using various filters and the corresponding energy spectra are obtained and shown in Fig. 2.16 as well. The sharp spectral filter (cut-off filter) is also used here for comparison. As expected, the energy spectrum is sharply cut off at high wavenumbers by the sharp spectral filter and the energy spectrum at larger scales (lower wavenumbers) is not affected. In contrast, the smooth filters (box and Gaussian filters) cause significant distortions of the spectrum not only at high wavenumbers but also at low wavenumbers, i.e. the large-scale motions are affected and the small-scale motions still contain significant amounts of energy, which smears the distinction between resolved and SGS scales. The box filter removes more energy than the Gaussian filter throughout the whole spectrum. The lower energy at low wavenumbers indicates that the large-scale motions beyond the inertial subrange are more affected by the box filter, which explains the stronger scale-dependent behavior. Meanwhile, in the relatively high-wavenumber range, the box filter is preferable in the FD framework, since the box filter is less “smooth” than

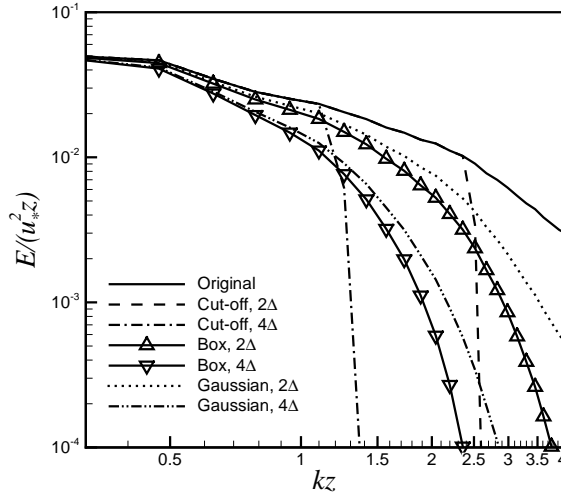


**Figure 2.16:** Averaged resolved kinetic energy spectrum from LASD-box-ske filtered by using different filters at height  $z = 50 m$ .

the Gaussian filter in physical space and therefore the separation of scales is less ambiguous (but the opposite is true in spectral space, indicating that the Gaussian filter might be more realistic in spectral LES), and the small-scale fluctuations are further suppressed.

## 2.5 Conclusions

Numerous sensitivity issues regarding finite-difference LES with dynamic Smagorinsky SGS models were investigated for the high-Reynolds-number neutral atmospheric boundary layer. Several conclusions can be made. First, in FD LES, the discrete truncation on a particular grid acts as an implicit smooth filter, which, in combination with the explicit filtering used in the Germano identity for dynamic Smagorinsky models, affects not only the small-scale motions but also the large-scale motions beyond the inertial subrange. In other words, the assumption of scale invariance is violated and truncation errors become important compared to the contributions of the SGS models. Dynamic Smagorinsky SGS models that do not consider scale dependence (the PASI and LASI models) fail in providing sufficient dissipation over the truncation errors,

which leads to the poor capture of both the logarithmic velocity near the surface and the  $-5/3$  region in the velocity spectra. On the other hand, if the scale dependence is considered, as in the LASD model, the SGS dissipation is sufficient to remove a large portion of the numerical noise and improved performances are obtained. Furthermore, it is found that, compared to the LASI or PASI model, the simulations with the LASD model are more sensitive to the convective term formulations, since their effects are more evident when truncation errors are sufficiently dissipated by the SGS model. In general, the skew-symmetric form has a better performance than the divergence form, due to its superior conservation property and reduced aliasing errors.

Second, the sensitivity tests of grid resolution show that all the SGS models investigated are grid-dependent, as a result of FD discretization. Although higher resolution improves the performance overall, it is not sufficient to give an improved prediction of the law-of-the-wall when the aspect ratio is unchanged. The dependence on the convective term, especially for the LASD model, can be reduced by higher resolution both in space and time.

Third, two commonly used smooth filters, box and Gaussian filters, are tested with the LASD model. Although both of them smear the separation between large-scale and small-scale motions, the box filter is less “smooth” in physical space and the distinction between resolved and unresolved scales is less ambiguous. Therefore, its performance is superior to the Gaussian filter in FD LES. The smoothing of the Gaussian filtering makes it unable to generate sufficient dissipation to remove small-scale numerical errors (similar to that observed with the PASI and LASI models), which eventually affects the large-scale flow features via elongated streamwise streaks in the neutral ABL.

Overall, among the dynamic Smagorinsky SGS models tested, the LASD model has the best performance in capturing the law-of-the-wall, due to its capability of suppressing the truncation errors resulting from the discretization and aliasing errors resulting from the non-linear convective term. Moreover, as pointed out by Chow and Moin [45], the dominance of the numerical errors over the contributions of the SGS

models (such as the PASI and LASI models, or the LASD model with the Gaussian filtering used here) can be significantly reduced by performing explicit filtering with larger width over the resolved velocity fields. With a mixed SGS model, the explicit filtering technique has been successfully implemented in wall-bounded FD LES applications [48, 49]. In their WRF model and LES investigations, Kirkil et al. [50] have shown that the performances of this explicit-filtered mixed model and the LASD model were comparable in simulations over flat terrain, but the mixed model was superior for the transverse ridge case. Therefore, in future work, the mixed model with explicit filtering will be investigated and compared with the LASD model in the framework of FD LES for complex turbulent flows.

## Chapter 3

### SELF-SIMILARITY AND TURBULENCE CHARACTERISTICS OF WIND TURBINE WAKES IN THE NEUTRAL ABL.

#### 3.1 Abstract

Mean and turbulent properties of the wake generated by a single wind turbine are studied here with a new large-eddy simulation (LES) code, the Wind Turbine and Turbulence Simulator (WiTTS). WiTTS uses a scale-dependent Lagrangian dynamical model of the sub-grid shear stress and actuator lines to simulate the effects of the rotating blades. WiTTS is first tested by simulating neutral boundary layers without and with a wind turbine and then used to study the common assumptions of self-similarity and axisymmetry of the wake under neutral conditions for a variety of wind speeds and turbine properties. We find that the wind velocity deficit generally remains self-similar to a Gaussian distribution in the horizontal. In the vertical, the Gaussian self-similarity is still valid in the upper part of the wake, but it breaks down in the region of the wake close to the ground. The horizontal expansion of the wake is always faster and greater than the vertical expansion under neutral stability, due to wind shear and impact with the ground. Two modifications to existing equations for the mean velocity deficit and the maximum added turbulence intensity are proposed and successfully tested. The anisotropic wake expansion is taken into account in the modified model of the mean velocity deficit. Turbulent kinetic energy (TKE) budgets show that production and advection exceed dissipation and turbulent transport. The nacelle causes significant increase of every term in the TKE budget in the near wake. In conclusion, WiTTS performs satisfactorily in the rotor region of wind turbine wakes under neutral stability.

## 3.2 Introduction

With the increasing demand for clean, safe, and cheap energy, wind power has been expanding globally in recent years and it has become a dominant renewable energy source, with over 280 GW installed worldwide by the end of 2012 [68]. In general, wind turbines are installed in wind farms along several rows and columns. Because wind turbines generate wakes that propagate downwind, the wakes from turbines in upwind rows can impact negatively the performance of downwind rows. Understanding wake losses is therefore an increasingly important topic as wind farms grow in size and in number of turbine rows. Although a modern wind turbine can be very large in size, e.g.  $> 100$  m in both diameter and hub height, it still operates in the lower part of the atmospheric boundary layer (ABL), where the wind is highly turbulent. Therefore, it is important to study the interaction between the turbulent atmosphere and the wind turbine wake in order to optimize the design of the wind turbine as well as the layout of the wind farm for maximum energy extraction.

As comprehensively reviewed in [69, 16], wind turbine wakes have been extensively studied in the past two decades. However, this topic is still far from being fully understood due to the highly turbulent nature of wakes. The wake can be roughly divided into two regions: the near wake and the far wake (although sometimes a transition region is also considered [69]). The near wake region is where the effect of the rotor is dominant and the wake is significantly affected by blade aerodynamics, stalled flow, and tip vortices [16]. Tip vortices are shed from the blade tip and root and propagate a short distance downstream following helical trajectories. When the inclination angle is small, the tip vortices can be interpreted as cylindrical shear layers that expand in the wake due to turbulent diffusion and form a ring-shaped domain of high turbulence intensity and great velocity gradients [69]. At a certain distance downstream, the tip vortices break down due to instability. This distance marks the end of the near wake region [69]. The range of the near wake region depends on wind loads and inflow conditions. Typically, it is confined to the region from the rotor to less than 3 diameters ( $D$ ) downstream [70]. Beyond the near wake, past a transitional region

[69], the far-wake region begins in which the wake is fully developed. Hypothetically, in the absence of ambient wind shear, velocity and turbulence intensity should remain self-similar and axisymmetric. In this region, rotor effects are less important whereas turbulent diffusion of momentum becomes dominant. Most effort in the literature has been put towards understanding the far-wake behavior [16].

The modeling frameworks to study wind turbine wakes can also be roughly divided into two groups: kinetic models and field models [69, 16]. In kinetic models, also known as explicit models, an analytical expression of a specific wake property, such as wind speed deficit, is explicitly given. Most kinetic models are based of self-similarity [71, 72, 73, 74]. In some widely used wake models, e.g. the Wind Atlas Analysis and Application Program (WAsP) [73, 75], the wake is assumed to be axisymmetric and grow linearly with a constant velocity deficit through the wake radius while the deficit decays with distance following a power law. However, the self-similarity and axisymmetry assumptions are questionable in the presence of strong wind shear and ground effects [16, 74, 76] and will be therefore evaluated in this study. Kinetic models have achieved great success in the wind industry sector due to their simplicity and computer efficiency.

The second approach to studying wind turbine wakes is to use so-called field models, also known as implicit models, which solve the flow equations numerically at every point of the flow field. In early works, a linearized form of the momentum equation in the main flow direction was used together with a parabolic approximation, a constant advection velocity, and a constant eddy viscosity [77]. Ainslie [78] developed a parabolic eddy viscosity model in which the wake was assumed to be axisymmetric. Due to the improvements in computer power, efficiency, and cost, numerical modeling of wind turbine wakes using computation fluid dynamics (CFD) has become more popular in recent years [79, 80, 81, 76, 82, 37, 36].

So far, directly solving the flow interactions with the blades at high Reynolds numbers has been too computationally intensive for most practical applications, especially if multiple wind turbines are considered. Therefore, parameterizations of the

aerodynamic forces on the rotor have been developed in the wind industry community. An example of such a parameterization is the actuator disk model, which uses a permeable circular disk to represent the rotor and the integrated thrust force induced by the wind turbine is uniformly distributed on the disk [81, 16]. This approach is easy to implement into a classic unsteady Navier-Stokes solver and has shown satisfactory results with relatively coarse grids [34, 35]. However, the original disk models were not able to take into account the rotational effects of the wind turbine blades since only drag force along the axial direction was considered. Alternatively, the actuator line model [79, 76, 36] calculates the instantaneous drag and lift forces of each blade element from tabulated airfoil data and distributes the forces along actuator lines representing the blades. Since the actuator line model uses the aerodynamic information of each blade element, it is capable of capturing detailed 3-D rotational phenomena, such as tip vortices, and it is therefore used in this study. The disadvantage is that both finer grid resolution and smaller time steps are required by the actuator line model than by the actuator disk model to smoothly resolve the flow structures that form on the fast moving blade tips.

Another important issue in using CFD for studying wind turbine wakes is how to properly represent the ABL turbulence. As pointed out by Chamorro and Porté-Agel [83] from their wind tunnel measurements, the turbulence properties of the incoming ABL have significant effects on the wakes. Since the Reynolds number of such a flow is usually very high ( $> 10^7$  based on rotor diameter and free wind speed at hub height), direct numerical simulation is still practically impossible with today's computer technology. Consequently, assumptions and simplified cases have been often used. In early CFD studies of wind turbine wakes, laminar free-stream flow with uniform wind speed has been widely used [80, 79, 82]. Troldborg *et al.* [84] generated a turbulent inflow with the same spectral characteristics as the real atmosphere by exerting time varying body forces in a plane upstream the rotor, but without mean wind shear. The techniques of solving Reynolds Averaged Navier-Stokes (RANS) equations are powerful in the studying of high-Reynolds number problems and their relatively high

efficiency is attractive from the industry point of view. Crespo *et al.* [85, 70, 69] developed the UPMWAKE model to calculate the wind turbine wake in the ABL using a parabolic approximation and the  $\kappa - \epsilon$  model for turbulence closure. However, RANS models directly resolve only the mean flow properties and parameterize the effects of the Reynolds stresses, whereas large-eddy simulation models directly resolve the unsteady flow properties, not the mean flow properties, all the way down to the filter scale and parameterize the effects of eddies smaller than that scale with so-called sub-grid scale (SGS) models. Consequently, LES has become increasingly popular for ABL simulations in recent years [21, 31]. Jimenez *et al.* [81] used a classic dynamic SGS model [23] to show that LES can be used successfully to investigate the details of the flow within wind turbine wakes. Calaf *et al.* [34, 35] studied the fully developed, neutral boundary layer in an array of several wind turbines using LES with a scale-dependent Lagrangian SGS model [28, 31, 32]. This SGS model is particularly suitable to study the anisotropic turbulence with complex geometry, such as wind turbine wakes, since it does not need any spatial averaging. The same SGS model was also used in Lu and Porté-Agel's [36] study of a large wind farm in a stable ABL and will be used in this study as well.

In this chapter, a new LES code is developed to study wind turbine wakes, the Wind Turbine and Turbulence Simulator, which uses the scale-dependent Lagrangian model for the SGS stresses and an actuator line model for the wind turbine rotor. By using WiTTS, the assumption of self-similarity and several wake models are examined for a single wind turbine in a neutral ABL. Turbulence intensity and TKE budgets are also studied. The paper is organized as follows: WiTTS is introduced in section 2; details of the simulation setup are given in section 3; the WiTTS validation is presented in section 4; and results of both mean flow properties and turbulence properties are discussed in section 5.

### 3.3 WiTTS: Numerical Methods and Modeling Approaches

#### 3.3.1 Governing equations and discretization

In this study, the filtered incompressible Navier-Stokes equations

$$\frac{\partial \tilde{u}_i}{\partial t} + \tilde{u}_j \frac{\partial \tilde{u}_i}{\partial x_j} = -\frac{1}{\rho} \frac{\partial \tilde{p}}{\partial x_i} - \frac{\partial \tau_{ij}^r}{\partial x_j} + f_{ei} - \Pi \delta_{i1} \quad (3.1)$$

with the continuity constraint

$$\frac{\partial \tilde{u}_i}{\partial x_i} = 0. \quad (3.2)$$

The meaning of each term, associated discretization and numerical methods have already been discussed in the last chapter, except the term  $f_{ei}$ , which represents the body forces from the actuator line model for the wind turbine aerodynamics.

#### 3.3.2 Actuator line model for wind turbine aerodynamics

In this study, the wind turbine blades are modeled by an actuator line model [79]. This model treats each blade as an actuator line which is comprised of a series of airfoil elements along the spanwise direction. At each element with a radius  $r$  in the  $(\theta, x)$  plane where  $\theta$  is the azimuthal coordinate, as shown in Fig. 3.1, the incident tangential velocity  $V_\theta$  and the normal velocity  $V_x$  are calculated by using an iterative blade-element momentum (BEM) method [86]. Note that in a standard actuator line model,  $V_\theta$  and  $V_x$  at the blade can be directly calculated from the velocity field by interpolation, so the BEM method is not necessary. But in our simulations, we found that interpolating directly at the blade is a bit problematic since it uses velocities affected by the distribution of the body forces. Instead, we interpolate the streamwise velocity a certain distance upstream of the blade (about  $3\Delta_x$ ), which is less affected by the rotor, and then use this velocity to predict the velocities at the blade by the BEM method. The local relative velocity  $\mathbf{V}_{rel}$  can be expressed as

$$\mathbf{V}_{rel} = (V_\theta - \Omega r, V_x), \quad (3.3)$$

where  $\Omega$  is the rotational speed of the turbine. Hence the angle between  $\mathbf{V}_{rel}$  and the rotor plane is  $\phi = \tan^{-1}(V_x/(\Omega r - V_\theta))$ . The angle of attack is defined as  $\alpha = \phi - \gamma$ ,

where  $\gamma$  is the local pitch angle. The lift coefficient  $C_L$  and the drag coefficient  $C_D$  are functions of  $\alpha$  and can be found from tabulated data for a specific airfoil. Consequently, the aerodynamic force per spanwise unit length is calculated as

$$\mathbf{f} = \frac{\mathbf{F}}{dr} = \frac{1}{2}\rho V_{rel}^2 c(C_L \mathbf{e}_L + C_D \mathbf{e}_D), \quad (3.4)$$

where  $\rho$  is the air density;  $c$  is the chord length; and  $\mathbf{e}_L$ ,  $\mathbf{e}_D$  are the unit vectors in the directions of lift and drag, respectively. A three-dimensional Gaussian distribution function [79] is applied to spread  $\mathbf{f}$  smoothly from each airfoil element to grid points in the following convolution form

$$\mathbf{f}_\epsilon = \mathbf{f} \otimes \eta_\epsilon, \quad \eta_\epsilon = \frac{1}{\epsilon^3 \pi^{3/2}} \exp\left(-\frac{d^2}{\epsilon^2}\right), \quad (3.5)$$

where  $d$  is the distance between a grid point and the element at the actuator line;  $\eta_\epsilon$  is the regularization kernel; and  $\epsilon$  is a constant to adjust the width of the distribution, which is set equal to the grid size in this study following Mikkelsen [87] and Wu and Porté-Agel [37]. Previous studies have shown that the predicted power is sensitive to this value [88, 76]. Churchfield et al. [7] suggested that  $\epsilon = C/4.3$  such that the Gaussian width is similar to the chord length  $C$ . Since the grid width  $\Delta = (\Delta_x \Delta_y \Delta_z)^{1/3}$  in this study is about half of the chord length, it means  $\epsilon \approx \Delta/2$ . However, as shown by Troldborg [76], a small value of  $\epsilon$  causes spurious oscillations in the resulting velocity field. In this study, we found that  $\epsilon = \Delta$  works well by comparing our LES data to the wind tunnel measurements as shown in later section 4.2.

The nacelle can be taken into account as a drag force  $F_x$ :

$$F_x = \frac{1}{2}\rho C_{D,nac} A_{nac} U_{hub}^2, \quad (3.6)$$

where  $A_{nac}$  is the incident area of the nacelle, and  $C_{D,nac}$  is the drag coefficient of the nacelle. The tower of the wind turbine can also be modeled as a drag force. However, it is neglected due to its small size compared with the resolution used in the current numerical simulations.

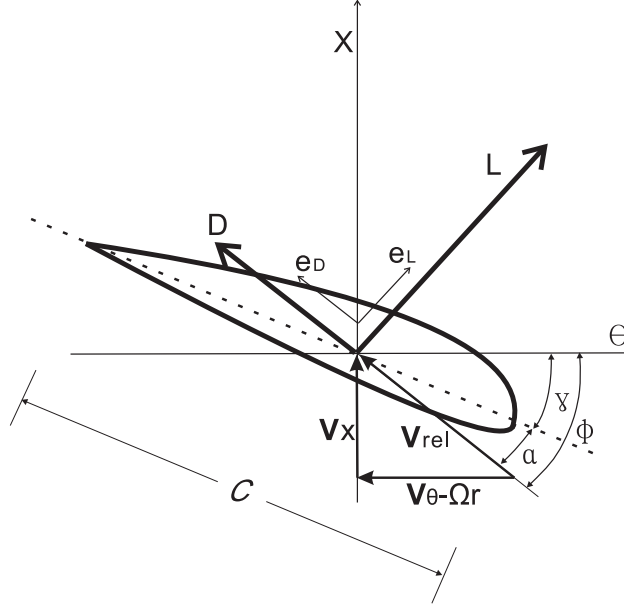


**Figure 3.1:** Cross-section airfoil element

### 3.4 Simulation Setup

The WiTTS model is used to study the neutrally-stratified turbulent boundary layer with a single wind turbine above a flat ground surface. In this study, the simulation setup generally follows the boundary layer wind tunnel tests of Saint Anthony Falls Laboratory at University of Minnesota [83]. The streamwise length of the computational domain is  $L_x = 4.32$  m, the vertical height is  $L_z = 0.46$  m and the spanwise length is  $L_y = 0.72$  m (Fig. 3.2). The wind turbine is located 0.6 m downstream from the inlet section and at the center in the spanwise direction. The diameter of the turbine rotor is  $D = 0.15$  m and the hub height is  $h = 0.125$  m. The ratio of  $D/h = 1.2$  is similar to that found in large turbines ( $\geq 2$ MW) [37]. The computational domain is uniformly divided in each direction by  $N_x \times N_y \times N_z = 288 \times 48 \times 64$  grid points, which corresponds to grid sizes of  $\Delta_x \times \Delta_y \times \Delta_z \approx 0.015$  m  $\times$  0.015 m  $\times$  0.007 m. In the scale-dependent Lagrangian dynamic SGS model, the test filtering at  $2\Delta$  and the second test filtering at  $4\Delta$ , where  $\Delta = \sqrt{\Delta_x^2 + \Delta_y^2}$ , are performed in a 2-D way in each horizontal plane by using a Gaussian filter.

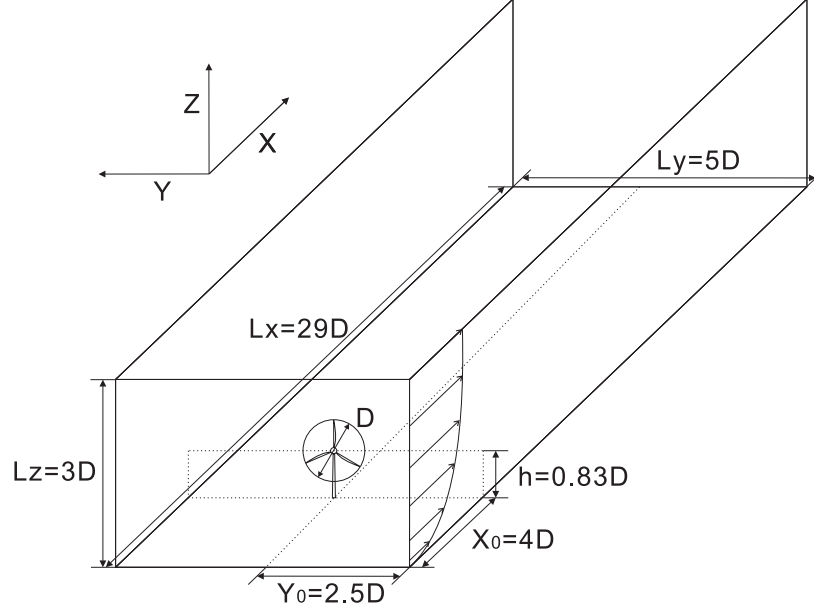


**Figure 3.2:** Schematic of the computational domain (not to scale)

As a consequence of the staggered grid used in this study, no boundary condition is necessary for the horizontal velocity components at the ground surface, but the wall model from Eq. 2.16 is used for shear stresses. The periodic conditions are used at the spanwise boundaries and the free slip condition is used at the top, i.e.  $\frac{\partial \tilde{u}}{\partial z} = 0$ ,  $\frac{\partial \tilde{v}}{\partial z} = 0$ ,  $\tilde{w} = 0$ . At the outlet section in the streamwise direction, the weakly-reflecting boundary condition is used:

$$\frac{\partial \tilde{u}_i}{\partial t} + C \frac{\partial \tilde{u}_i}{\partial x} = 0, \quad (3.7)$$

where  $C$  is a characteristic speed and it is taken as the mean streamwise velocity at the inflow section. The inflow boundary condition is imposed at the inlet section in the streamwise direction of the domain. The inflow information comes from a separate simulation of the turbulent boundary layer using the same code with the same domain size and resolution but without the wind turbine. In this separate simulation, the periodic boundary conditions are used at all horizontal boundaries. The simulation are carried out for a period long enough for the turbulence to become fully developed.

In order to study the influence of different flow characteristics on the performance of the wind turbine, three different boundary layers are generated with different mean wind speeds at the hub height:  $U_{hub} \simeq 1.6$  m/s, 2.2 m/s, 3.4 m/s. The surface roughness length is set to be  $z_0 = 0.03$  mm.

The wind turbine in the wind tunnel study uses a three-blade GWS/EP-6030×3 rotor [83, 37]. The wind turbine rotates at either constant rotational speed  $\Omega$  or constant tip speed ratio  $\lambda = \Omega \frac{D}{2} / U_{hub}$ . A list of selected cases discussed in this study is shown in Table 3.1. Note that Cases 1-6 are numerical wind tunnel experiments using the WiTTS code whereas Case 7 is a full-scale simulation using Simulator for Off-shore Wind Farm Applications (SOWFA) [89], a computational fluid dynamics solver developed at the National Renewable Energy Laboratory, USA, for the sake of cross-comparison and generality. In SOWFA, the governing equations are solved using the finite-volume method on unstructured meshes and the constant Smagorinsky model ( $C_S = 0.168$ ) for the SGS shear stress[7]. An actuator-line model for the wind turbine was also used in SOWFA. In SOWFA the rotor speed is neither determined by a fixed rotational speed nor by a fixed tip-speed ratio, but by a torque controller in which the torque comes out of integrating the aerodynamic forces from the blade elements. The resolution in Case 7 is about 3.5 m. The Siemens SWT-2.3-93 wind turbine with rotor diameter of 93 m and hub height of 63.4 m is used in Case 7. The mean streamwise velocity at the hub height is about  $U_{hub} = 8.65$  m/s. Note that the drag coefficient of the nacelle in Case 7 is effectively 0 because SOWFA does not include any treatment of the nacelle. In the table,  $C_T$  is the thrust coefficient defined as follows

$$C_T = \frac{T}{\frac{1}{2}\rho U_{hub}^2 A}, \quad (3.8)$$

where  $A$  is the swept area of the rotor, and  $T$  is the thrust force which is equal to the total form drag force integrated from the actuator line model by assuming that the skin friction is negligible.

Case	$U_{hub}$ (m/s)	$u_*$ (m/s)	$z_0$ (mm)	$\lambda$	$\Omega$ (rpm)	$C_{D,nac}$	$C_T$
1	2.2	0.102	0.03	4.25	N/A	0.85	0.461
2	2.2	0.102	0.03	N/A	1120	0.85	0.461
3	2.2	0.102	0.03	N/A	1500	0.85	0.375
4	1.6	0.075	0.03	4.25	N/A	0.85	0.450
5	3.4	0.150	0.03	4.25	N/A	0.85	0.550
6	2.2	0.102	0.03	4.25	N/A	0.3	0.476
7	8.65	0.386	9.0	N/A	N/A	0.0	0.560

**Table 3.1:** Setup details of the seven cases simulated in this study. Cases 1-6 are numerical wind tunnel experiments using the WiTTS code and Case 7 is a full-scale simulation using SOWFA.  $U_{hub}$ : the mean streamwise component of velocity in the free upstream at hub-height level;  $u_*$  is the friction velocity;  $z_0$ : surface roughness length;  $\lambda$ : tip-speed ratio of rotor;  $\Omega$ : rotational speed of rotor;  $C_{D,nac}$ : drag coefficient of nacelle disk;  $C_T$ : thrust coefficient.

### 3.5 WiTTS Validation

The WiTTS results of Case 1 are compared with the wind tunnel measurements reported in [83]. The vertical profiles of the time-averaged, resolved, streamwise component of velocity  $\bar{u}$  are plotted at several downstream sections in Fig. 3.3. Note that, from this point on,  $\overline{(\cdot)}$  denotes a time average instead of the test filtering used in earlier sections and  $\widetilde{(\cdot)}$  is neglected for simplicity. In general, the WiTTS results match well with the wind tunnel data, especially in the region above the hub, although an overestimation of wind speed below the hub is also observed. This overestimation has two possible contributors: one is from the ‘‘overshoot problem’’, shown in Fig. ?? (b) and Fig. 3.3 at  $x/D = -1$  by the overestimation of mean wind shear  $\phi_m$ , and the other is the absence of the tower in our simulation. However, the overestimation is mainly in the region below the rotor near the wall and its magnitude is small compared with the deficit in the rotor region. The velocity deficit is confined generally within the region of the turbine rotor and its maximum occurs behind the nacelle since the nacelle has a relatively large drag coefficient compared with the blades. The velocity deficit region, i.e. wake region, expands slowly downstream while its magnitude decreases. The velocity almost recovers back to its upstream profile after 20D downstream.

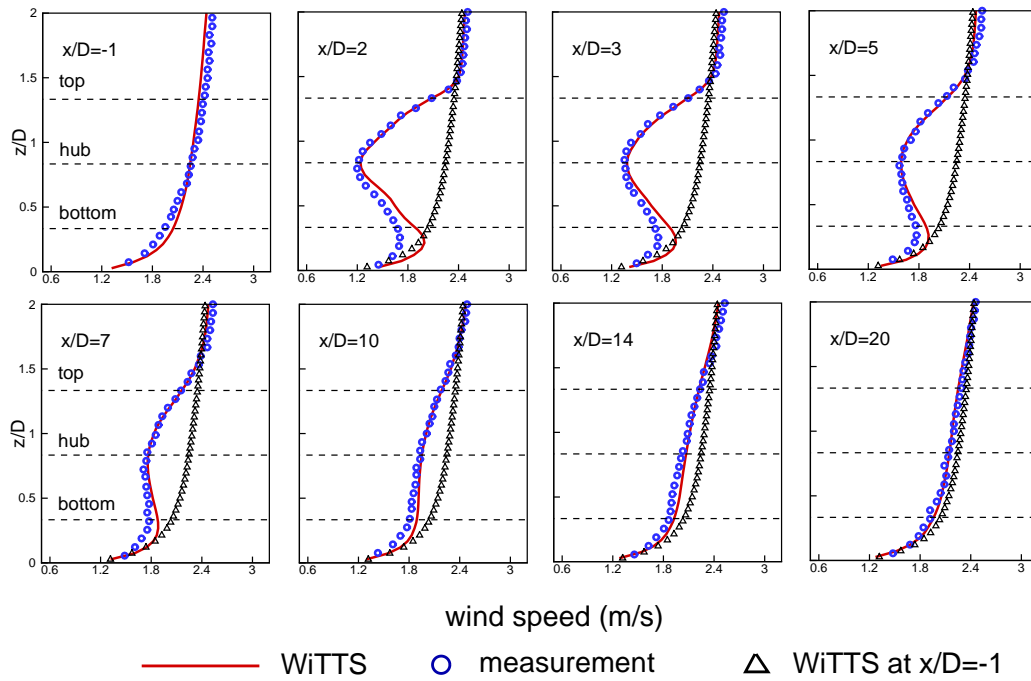


**Figure 3.3:** Comparison of profiles of time-averaged mean streamwise component of velocity at several downstream sections on the vertical central plane.

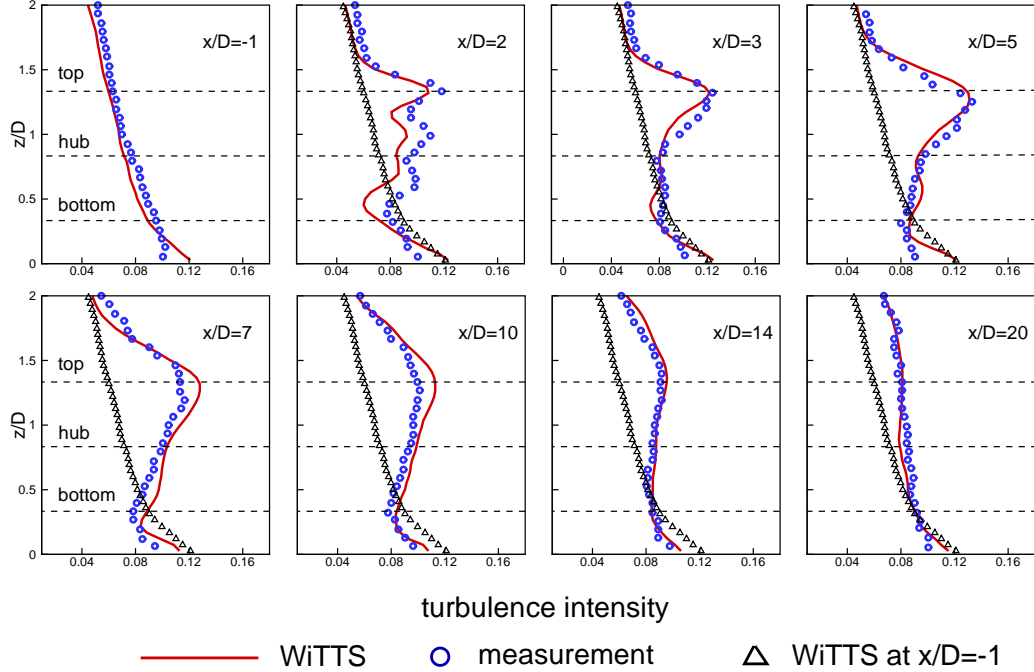


**Figure 3.4:** Comparison of profiles of turbulence intensity  $I_x$  at several downstream sections on the vertical central plane.

Fig. 3.4 compares the resolved streamwise turbulence intensity  $I_x$ , which is defined as the root-mean-square (rms) of the resolved streamwise velocity fluctuation component  $u' = u - \bar{u}$  divided by  $U_{hub}$ , resulted from the WiTTS and the experiment. The simulated vertical profiles of  $I_x$  agree well qualitatively with the wind tunnel data, especially for the location of the maximum and minimum values. Both WiTTS and the wind tunnel data show that in general turbulence intensity is increased in the wake by the wind turbine and at each downstream section the maximum occurs near the top-tip height, due to the high wind shear. The global maximum appears near  $\sim 5-7D$  downstream. Unlike velocity, turbulence intensity recovers much slower and it is still noticeable after  $20D$  especially in the region above hub height. Note that near the ground an overestimate appears due to the less accurate scaling of the law-of-the-wall discussed earlier. But still, this numerical problem appears only in the region near the wall and does not seem to affect the rotor region, which is the focus of this paper.

The vertical profiles of the kinematic shear stress  $-\overline{u'w'}$  including its SGS part are compared in Fig. 3.5. In the rotor region, the wake exhibits two opposite behaviors above and below the hub height. Above the hub height, the shear stress (equal and opposite in sign to the turbulent momentum flux) is positive and enhanced by the wind turbine, which implies a stronger downward turbulent momentum flux with the wind turbine than without it. Two maxima are found: the first one at the top-tip height, lasting almost throughout the entire wake, and a second maximum near the hub height in the near wake region  $< 2D$ . Below the hub height, shear stress is enhanced too but with a negative sign in the wake  $< 10D$ , which implies a stronger upward turbulent momentum flux with the turbine than without it. This suggests that entrainment occurs in such a way that enhanced downward momentum flux is found above the hub height and enhanced upward momentum flux below the hub height.

In summary, although some discrepancies exist between the results of WiTTS and the experiments in the region near the wall, in most part of the boundary layer and in the wake region they match well. Since we are interested in the rotor region, which is away from the wall, WiTTS appears to be a valid choice for this study.

## 3.6 Results

### 3.6.1 Mean velocity properties

The self-similarity of a wake after a bluff body has been studied for decades [90, 91]. In a fully developed wake, the time-averaged, resolved, streamwise velocity deficit  $\delta U(x, y, z) = \bar{u}_{inflow}(z) - \bar{u}(x, y, z)$ , normalized by its maximum  $\delta U_{max}(x)$ , can be expressed as one function as:

$$\frac{\delta U(x, y, z)}{\delta U_{max}(x)} = f(\xi), \quad (3.9)$$

where  $f(\xi)$  is a self-similar shape function of  $\xi(x, y, z) = r(y, z)/r_{\frac{1}{2}}(x)$ ,  $r$  is the distance from the centerline of the wake, and  $r_{\frac{1}{2}}(x)$  is the half-width, which is defined as the spanwise distance between two points on a profile at which the mean deficit is half of its maximum. The assumption of self-similarity is critical in several wind turbine

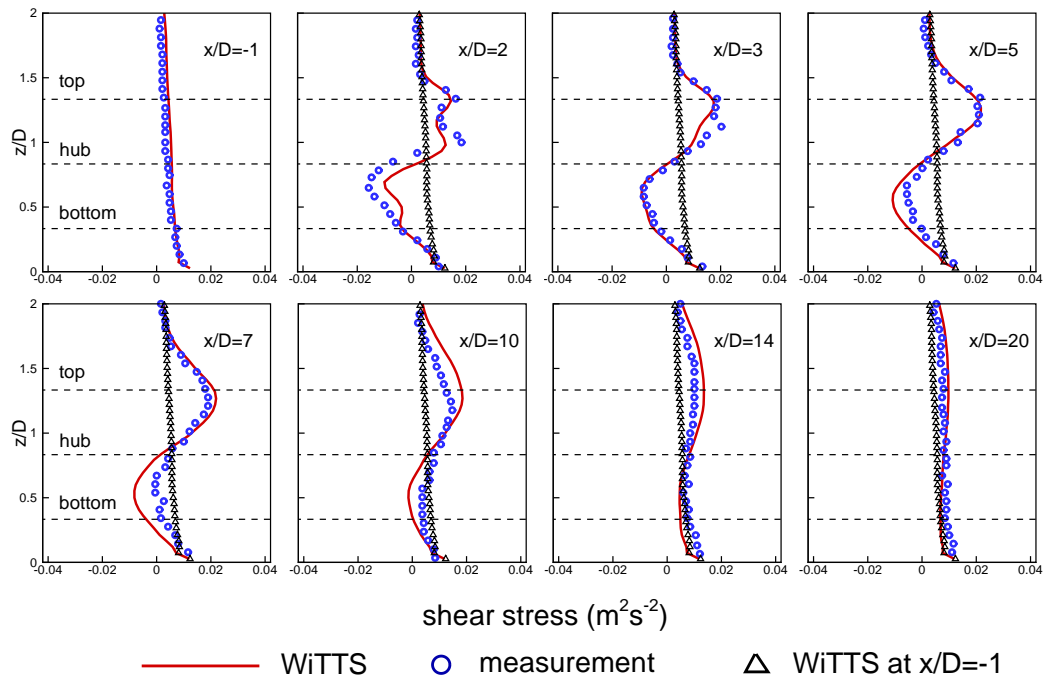


**Figure 3.5:** Comparison of profiles of the kinematic shear stress  $-\overline{u'w'}$  at several downstream sections on the vertical central plane.

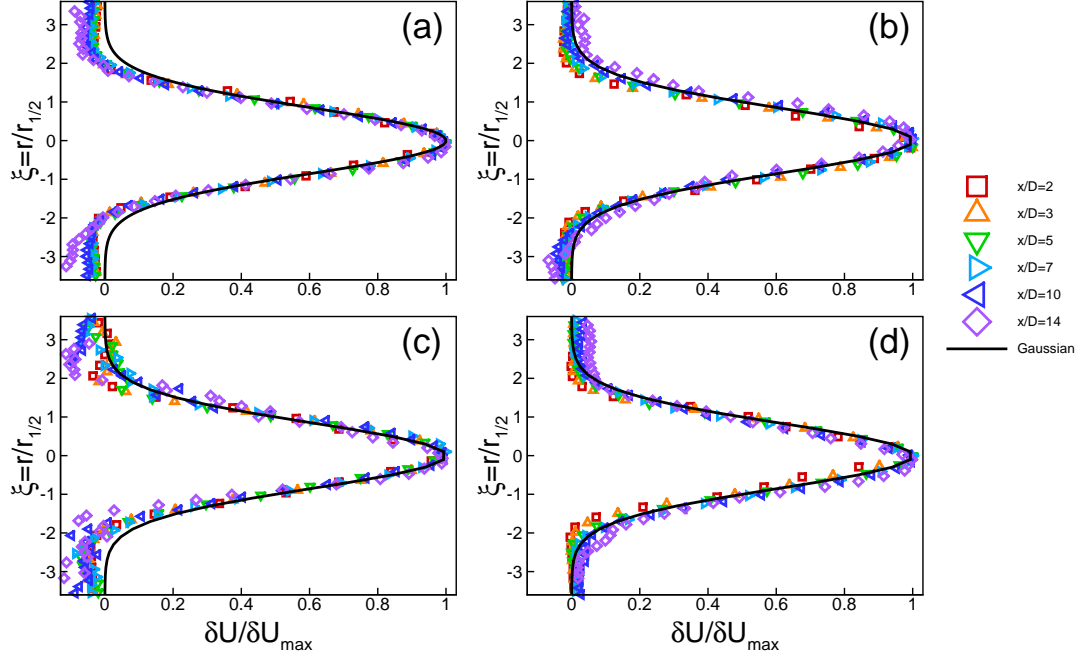


**Figure 3.6:** Self-similarity profiles of time-averaged resolved streamwise velocity deficit in the horizontal plane at the hub height for: (a) Case 1; (b) Case 4; (c) Case 5; (d) Case 6. The velocity deficits are normalized by its value at the centerline. The y-axis is the radial coordinate  $r = d/2$  normalized by the half-width  $r_{1/2}$  at that section.

wake models [73, 74, 92]. However, this assumption is still arguable considering that a rotating wind turbine is much more complicated than a still bluff body. In order to clarify it, the normalization is carried out upon the profiles of  $\delta U$  for Case 1, 4, 5, and 6 in the horizontal plane at hub height and in the vertical central plane, respectively. A theoretical Gaussian function obtained with the hypothesis of uniform eddy viscosity ([91], p. 154) in the following form is used for comparison:

$$f(\xi) = \exp(-\xi^2 \ln 2). \quad (3.10)$$

As shown in Fig. 3.6, in the bulk region of the wake, the self-similarity assumption with the Gaussian shape works reasonably well in the horizontal plane, especially for  $|\xi| \leq 1$ . The deviation from the Gaussian shape increases with the radius towards the edge of the wake where the shear is strong. Also, in the near wake, e.g.  $x/D \leq 3$ ,

Case 6 shows a small but noticeable deviation from the Gaussian curve. This implies that the self-similarity in the near wake depends on the specific design of the rotor and nacelle. An extreme example showing the effect of the nacelle design is plotted in Fig. 3.7, where the non-dimensional mean streamwise velocity deficit  $\delta u/U_{hub}$  of Case 1 and Case 7 are compared. Recall that Case 1 is a wind-tunnel-scale simulation by WiTTS with nacelle, while Case 7 is a full-scale simulation by SOWFA without nacelle. Clearly, the discrepancy is significant in the near wake region. In Case 1, a single maximum deficit is found along the centerline. In contrast, two deficit maxima are observed in Case 7, each centered approximately at half the rotor radius. After 6D downstream, the two maxima merge together gradually at the centerline with the expanding of the annular shear layer. The two cases become similar only after about 7D, and the self-similarity for Case 7 appears much later than for Case 1. Nevertheless, the specific design of a turbine only has a significant effect in the near or intermediate wake region, but in the far-wake region, e.g.,  $x/D > 7$ , the wake is less influenced by the turbine design and shows self-similar properties well.

Similarly, vertical profiles of velocity deficit are shown in Fig. 3.8. Basically, self-similarity holds well in the upper half of the profiles, although small deviations are also found near the wake edges. In the lower parts of the profiles, however, self-similarity is preserved up to  $\xi \sim -1$ . Below that, it is invalidated by the strong shear near the ground, especially for Case 5 in Fig. 3.8 (c), in which  $u_*$  is the strongest among the four cases. In summary, the assumption of self-similarity is verified in the bulk region of the wake both horizontally and vertically, but it only holds in the far wake region since in the near wake the design of the nacelle has a significant impact. Also, the self similarity is less valid where wind shear is strong, e.g. near the edges of the wake or near the ground.

To evaluate wake effects or develop wake models, it is important to study how the wake develops with distance. Since self-similarity is often assumed, the evaluation of  $\delta U_{max}(x)$  is critical, and different relationships are used in different wake models. As shown in Fig. 3.6 and 3.8, the maximum always appears near the centerline of the

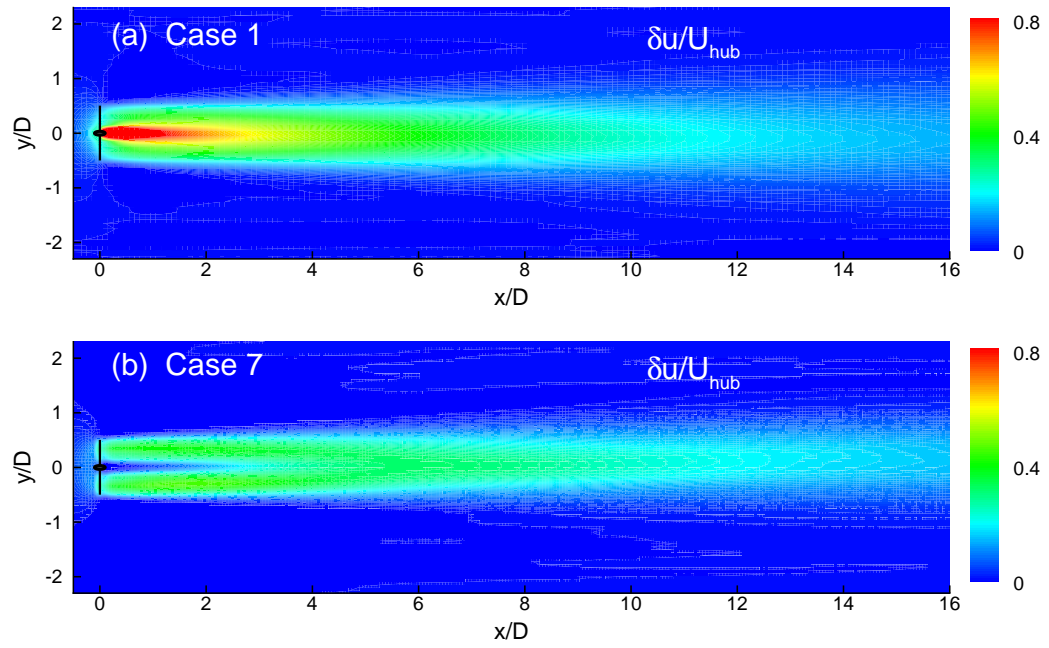


**Figure 3.7:** Contours of non-dimensional time-averaged resolved streamwise velocity deficit in the horizontal plane at hub height for (a) Case 1 and (b) Case 7. The deficit is normalized by  $U_{hub}$ .

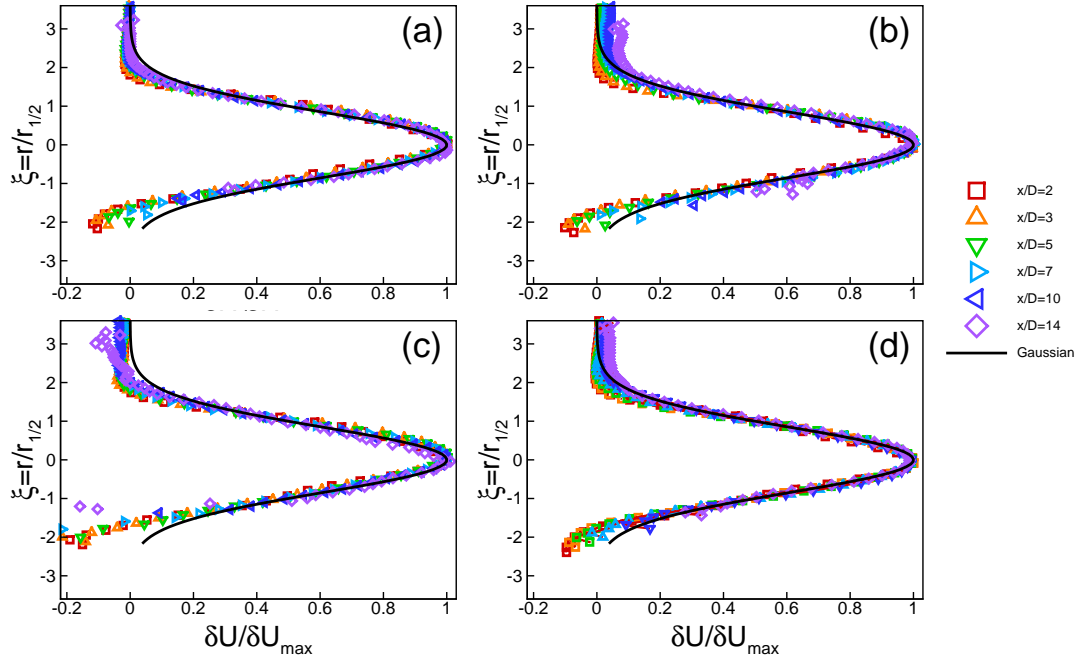


**Figure 3.8:** Self-similarity profiles of time-averaged streamwise velocity deficit in the vertical central plane for: (a) Case 1; (b) Case 4; (c) Case 5; (d) Case 6. The velocity deficits are normalized by its value at the centerline. The y-axis is the radial coordinate  $r = d/2$  normalized by the half-width  $r_{\frac{1}{2}}$  at that section.

wake in cases where the nacelle effect is not negligible. Therefore,  $\delta U_{hub}$  is often used, since it is easier to measure. By fitting data from field measurements, Barthelmie *et al.* [3] proposed:

$$\frac{\delta U_{hub}}{U_\infty} = c_1 \left(\frac{x}{D}\right)^{c_2}, \quad (3.11)$$

where  $U_\infty$  is the mean wind speed upstream and  $c_1$  and  $c_2$  are constants with values of (1.03, -0.97) or (1.07, -1.11), which are equally plausible.

The widely-used Jensen's model [73, 75] assumes a top-hat function for  $f(\xi)$  in Eq. 3.9, such that  $\delta U_{max}(x/D) = \delta U(x/D)$  is constant inside the wake at  $x/D$  which yields:

$$\frac{\delta U}{U_\infty} = a' \left( \frac{1}{1 + 2k_{wake} \frac{x}{D}} \right)^2 \quad (3.12)$$

based on a linear expansion of the wake. Here,  $a' = 2a = (1 - \sqrt{1 - C_T})$  is twice of the induction factor  $a$ ,  $C_T$  is the thrust coefficient,  $k_{wake} = A / \ln(h_{hub}/z_0)$  is a wake decay constant,  $A \approx 0.5$  [83], and  $z_0$  is the surface roughness length. The wake diameter  $D_w(x)$  at distance  $x$  is determined by:

$$D_w(x) = (1 + 2\alpha_0 \frac{x}{D})D, \quad (3.13)$$

where  $\alpha_0$  is a constant rate of expansion of the wake radius.

With similar assumptions of top-hat profiles and linear-expansion of the wake, an analytical modeling was proposed by Frandsen *et al.* [74] using momentum conservation in the wake as follows:

$$\frac{\delta U}{U_\infty} = \frac{1}{2} \pm \frac{1}{2} \sqrt{1 - 2 \frac{A_0}{A(x)} C_T}. \quad (3.14)$$

Here  $A_0$  is the incident rotor area and  $A(x)$  is the area of the cross section of the wake at distance  $x$ . The “+” applies when  $a' > 0.5$  and “-” applies when  $a' \leq 0.5$ . In the absence of wind shear, the cross section of the wake is a circle, i.e.  $A(x) = \pi(\frac{D_w}{2})^2$ , and

$$D_w(x) = (\beta^{k/2} + \alpha \frac{x}{D})^{1/k} D. \quad (3.15)$$

Here  $\beta = \frac{1}{2} \frac{1+\sqrt{1-C_T}}{\sqrt{1-C_T}}$ ,  $k = 3$  and

$$\alpha = \beta^{k/2} [(1 + 2\alpha_0 \frac{x}{D})^k - 1] / (\frac{x}{D}). \quad (3.16)$$

Recently, based on LES results, Bastankhah and Porté-Agel [92] proposed a new analytical model from conservation of mass and momentum. The self-similarity property is used with a uniform Gaussian distribution of the velocity deficit as follows:

$$\frac{\delta U_{hub}}{U_\infty} = 1 - \sqrt{1 - \frac{C_T}{8(k^*x/D + \varepsilon)^2}}, \quad (3.17)$$

where  $k^* = \partial\sigma/\partial x$  is the growth rate of the wake,  $\sigma$  is the standard deviation of the velocity deficit that will be discussed later,  $\varepsilon = 0.2\sqrt{\beta}$ , and  $\beta = 0.5(1+\sqrt{1-C_T})/\sqrt{1-C_T}$ . By using the Gaussian distribution, the velocity deficit at any position  $(x, y, z)$  can be found as

$$\frac{\delta u(x, y, z)}{U_\infty} = \frac{\delta U_{hub}(x)}{U_\infty} \exp(-\frac{1}{2(k^*x/D + \varepsilon)^2} [(\frac{z - z_h}{D})^2 + (\frac{y}{D})^2]), \quad (3.18)$$

where  $z_h$  is the hub height.

In Fig. 3.9, we present the non-dimensional velocity deficit at hub height  $\delta U_{hub}/U_{hub}$  from our LES results together with the wake model predictions described above. The LES results show that in the near wake region, the curve shapes highly depend on the incoming wind conditions and nacelle designs. Interestingly, Case 7, which has no nacelle, shows an increase of the deficit with distance from almost zero to its maximum at about 6D to 7D, which corresponds to the merge of the two maxima of deficit at the centerline shown in Fig. 3.7 (b). For those cases with higher drag of the nacelle, the maximum appears faster with larger magnitude. In the far wakes, all the cases decrease gradually, and the rate of decay decreases with distance. In Fig. 3.9 (a), the Barthelmie's empirical model with two sets of suggested parameters is also plotted. Since this model is based on field measurements, it gives fair prediction to some of our LES data in the far wakes when  $c_1 = 1.03, c_2 = -0.97$  are used. However, the magnitudes are underestimated by both choices. Moreover, the curves of the deficits do not converge for different conditions such that it is hard to fit all curves by

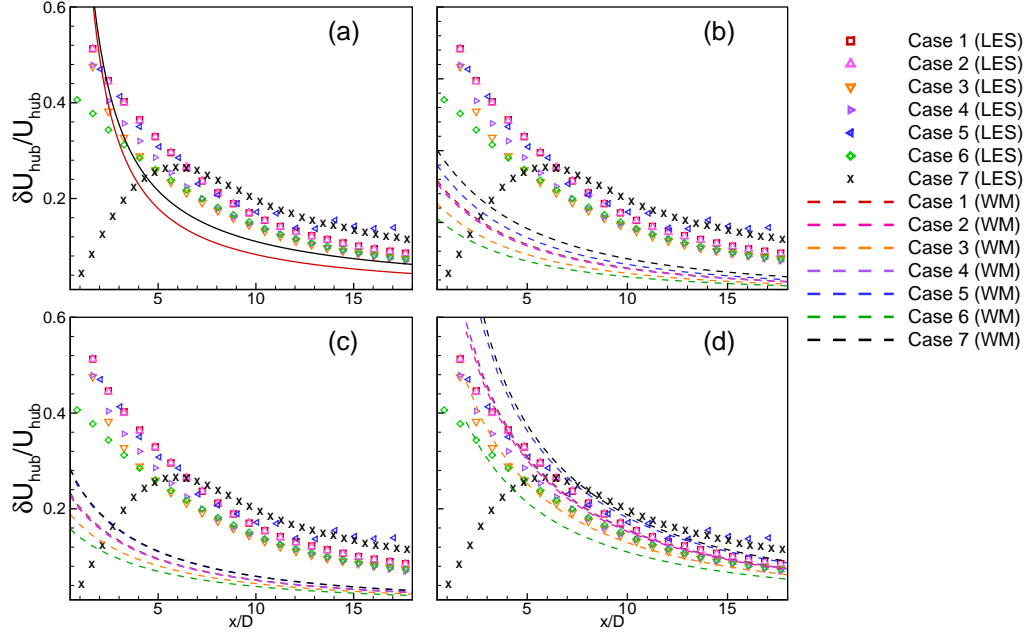


**Figure 3.9:** Non-dimensional time-averaged streamwise velocity deficit at hub height with LES and with several wake models. The velocity deficits are normalized by upstream mean wind speed at hub height  $U_{hub}$ . The symbols are LES results and lines are wake model results. The Barthelmie's model (Eq. 3.11) is used in (a) and  $c_1 = 1.03, c_2 = -0.97$  are used for the black solid line and  $c_1 = 1.07, c_2 = -1.11$  are used for the red solid line; the Jensen's model (Eq. 3.12) is used in (b); the Frandsen's model (Eq. 3.14) is used in (c); and the Bastankhah's (Eq. 3.17) model is used in (d).

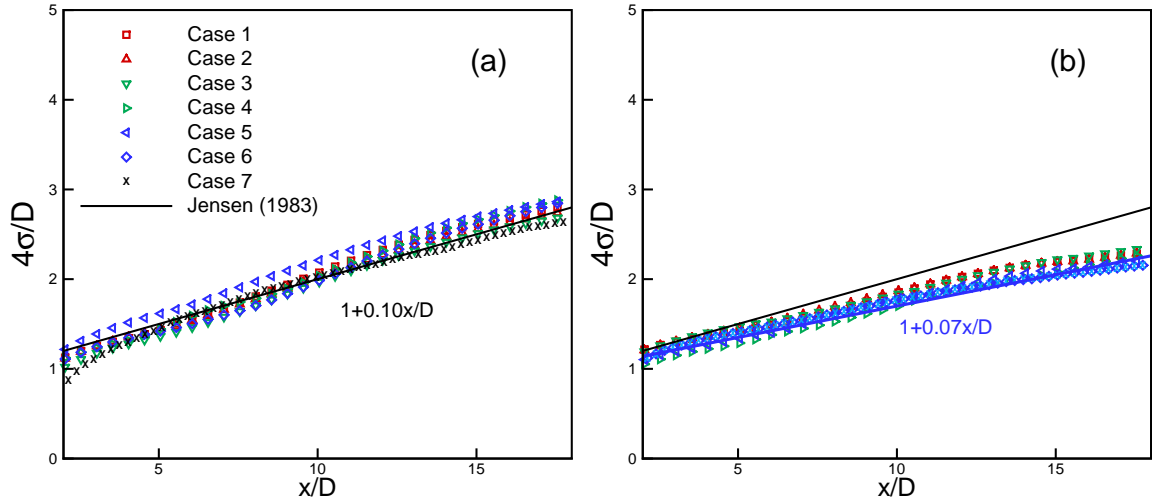


**Figure 3.10:** The wake width represented by  $4\sigma/D$  along the streamwise direction, where  $D$  is the rotor diameter and  $\sigma$  is the standard deviation of mean velocity deficit: (a) in the horizontal plane at the hub-height level, representative of horizontal wake expansion, and (b) in the vertical central plane, representative of vertical wake expansion.

using only one or two relationships. The Jensen's model and the Frandsen's model are used in Fig. 3.9 (b) and (c), respectively. Since both models start from the top-hat assumption of the deficit distribution, they underestimate the velocity deficit at the centerline significantly. The Bastankhah's model plotted in Fig. 3.9 (d) appears to be the best of the three candidates. It successfully captures the non-converging curves due to different  $C_T$  and matches reasonably well with each individual case. However, it still underestimates the magnitude and overestimate the rate of decrease of the deficit with distance in the far wake. The discrepancies are possibly caused by the assumption that the wake grows isotropically in all directions perpendicular to the wind direction, without consideration of the azimuthal variation caused by the ambient wind shear, as discussed next.

In order to quantify the wake growth, the standard deviation  $\sigma$  (square root of the variance  $\sigma^2$ ) of the mean velocity deficit  $\delta u(\mathbf{x})$  at each cross section is often treated

as a proxy for the width (or spread) of the wake. The variance is calculated as follows:

$$\sigma^2 = \frac{1}{M_0} \int_{-\infty}^{\infty} (\mathbf{x} - \mu)^2 \delta u(\mathbf{x}) d\mathbf{x} = M_2/M_0 - \mu^2. \quad (3.19)$$

Here  $\mu = M_1/M_0$  is the mean and  $M_0, M_1$  and  $M_2$  are the zeroth, first, and second moments, respectively, defined as:

$$M_0 = \int_{-\infty}^{\infty} \delta u(\mathbf{x}) d\mathbf{x}, \quad M_1 = \int_{-\infty}^{\infty} \mathbf{x} \delta u(\mathbf{x}) d\mathbf{x}, \quad M_2 = \int_{-\infty}^{\infty} \mathbf{x}^2 \delta u(\mathbf{x}) d\mathbf{x}. \quad (3.20)$$

For a Gaussian distribution, a spread of  $4\sigma$  includes approximately 95% of the area under the distribution thus it is often used as the “boundary” of the wake. Accordingly, the non-dimensional standard deviation normalized by the rotor diameter can be calculated horizontally at the hub-height level and vertically in the vertical central plane, respectively (Fig. 3.10). The prediction from the Jensen’s model Eq. 3.13 is also shown as a comparison, in which  $\alpha_0 = 0.05$  is chosen. For the horizontal expansion of the wake at the hub-height level, the linear assumption used in the Jensen’s model actually works well. The LES results approximately follow the same rate of linear expansion, although they grow a bit faster in the region  $5 < x/D < 10$  and a slightly slower past  $10D$  (Fig. 3.10 (a)). On the other hand, for the vertical expansion of the wake (Fig. 3.10 (b)), the LES results depart significantly from the Jensen’s wake model. The expansions are slower overall and the discrepancies increase with distance, which implies an anisotropy in the wake growth. Another linear relationship  $1 + 0.07x/D$  was used in Fig. 3.10 (b) to better fit the curves, i.e.  $\alpha_0 = 0.035$ . Note that this fitting is not perfect since the LES curves appear less linear in the far wakes, but it is used here only for its simplicity.

To examine this anisotropy, contours of non-dimensional velocity deficit  $\delta u/\delta u_{max}$ , where  $\delta u_{max}$  is the maximum of the deficit at the cross section, are plotted at several vertical cross sections downstream in Fig. 3.11 for Case 1. The boundary of the wake is represented by the contour line of  $\delta u/\delta u_{max} = 0.136$ , corresponding to the value at  $4\sigma$  of a normal distribution. As shown in Fig. 3.11 (a), (b), the anisotropy is relatively small all the way to about  $x/D \approx 8$ , as the contours are qualitatively symmetric and

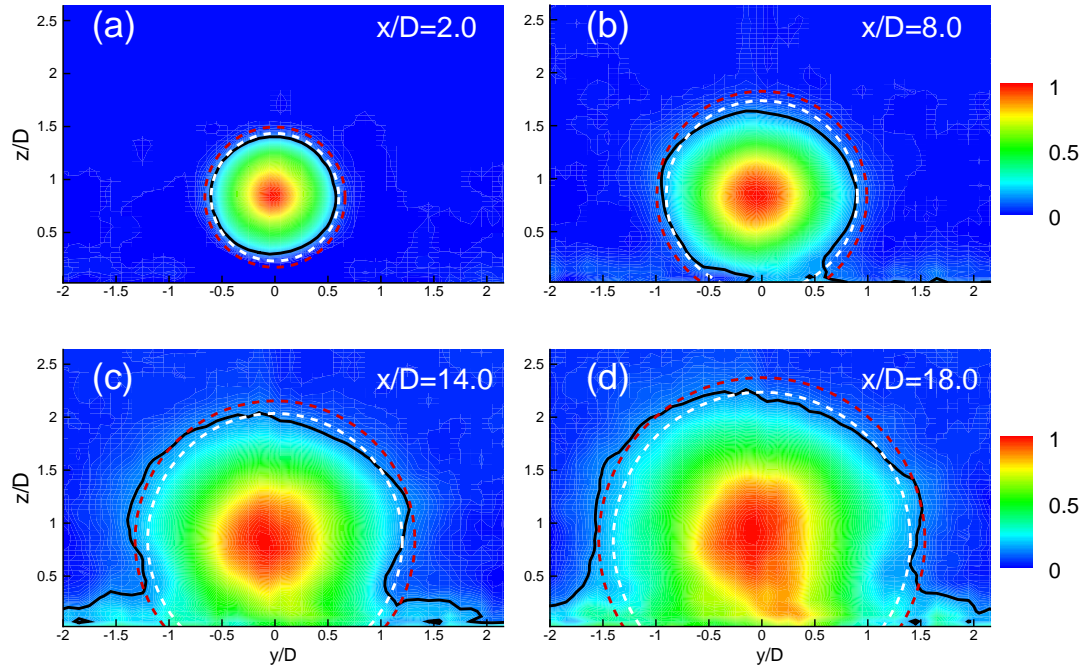


**Figure 3.11:** Contours of non-dimensional mean velocity deficit of Case 1 on the cross sections at (a)  $x/D=2$ , (b)  $x/D=8.0$ , (c)  $x/D=14.0$  and (d)  $x/d=18.0$ . The velocity deficit is normalized by the maximum of deficit  $\delta U_{max}$  at each section. The black solid line represents the contour line of  $\delta u / \delta u_{max} = 0.136$ . The white and red dashed lines are the predicted wake boundary from the Jensen's model and the Frandsen's model, respectively.

circular, which suggests that the wake models produce reasonably good predictions. However, the wake expansion is still slightly slower vertically than horizontally, due to vertical wind shear, as shown by the more elliptic than circular shape. But the difference between the axes are small so the shape doesn't not change too much. In the further downstream wake regions (Fig. 3.11 (c), (d)), besides the vertical wind shear, the anisotropy is primarily caused by the impact of the wake with the ground, which causes the wake to spread out laterally near the ground and the elliptic shape to be destroyed. However, this effect is limited in the lower part and the rest of the wake is less affected.

Looking back at the Bastankhah's model, it is clear that ignoring the anisotropic wake expansion causes an overestimate of the area of wake in the far wake region, especially when the wake hits the ground. Therefore, the mean velocity deficit is underestimated due to conservation of mass and momentum, whereas the decay rate is overestimated. Here, a simple modification is proposed to take the anisotropic wake expansion into account. Instead of using the same  $\sigma$  in all directions, an elliptical Gaussian function corresponding to  $\sigma_y \neq \sigma_z$  can be used in the following relationship

$$\frac{\delta u(x, y, z)}{U_\infty} = \frac{\delta U_{hub}(x)}{U_\infty} \exp\left(-\left(\frac{y^2}{2\sigma_y^2} + \frac{(z - z_h)^2}{2\sigma_z^2}\right)\right). \quad (3.21)$$

As shown in Fig. 3.10, we can simply use the linear estimations of  $\sigma_y$  and  $\sigma_z$  as

$$\frac{\sigma_y}{D} = k_y \frac{x}{D} + \varepsilon, \quad \frac{\sigma_z}{D} = k_z \frac{x}{D} + \varepsilon \quad (3.22)$$

where  $k_y$  and  $k_z$  are expansion rates of the wake in the horizontal and vertical directions, respectively, and  $\varepsilon$  is defined in Eq.3.17. As a consequence of Eq. 3.21, by equating the momentum loss to the total thrust force following the same procedure of Bastankhah and Porté-Agel [92], Eq. 3.17 can be rewritten as

$$\frac{\delta U_{hub}}{U_\infty} = 1 - \sqrt{1 - \frac{C_T}{8 \frac{\sigma_y \sigma_z}{D^2}}}. \quad (3.23)$$

Note that Eq.3.23 coincides to Eq.3.17 when  $\sigma_y = \sigma_z$ .

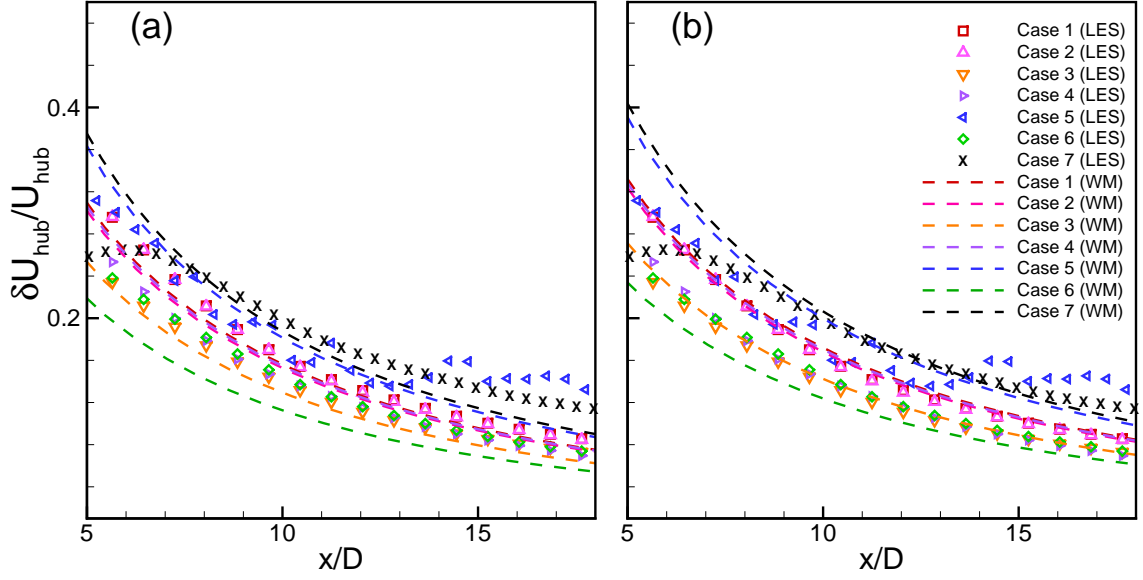


**Figure 3.12:** Comparisons of the modified Bastankhah's model and Bastankhah's original model for non-dimensional time-averaged streamwise velocity deficit at hub height. The symbols are LES results and the dashed lines in (a) are from the original Bastankhah' model and in (b) are from the modified model.

The modified model Eqn.3.23 is tested by using the present cases and  $k_y = 0.025$ ,  $k_z = 0.0175$  from the observation of Fig. 3.10. Note that the expansion rates are not constant but vary case by case, as shown in [92] and [93]. Comparisons between the modified model and the original model are shown in Fig. 3.12. As discussed earlier, the Bastankhah's original model underestimates the values of velocity deficit in the far wakes in Fig. 3.12(a), meanwhile the modified model reduces this underestimation noticeably and matches better with the LES results in Fig. 3.12(b). It shows that the anisotropy in the wake expansion is important to get the correct estimation of the velocity deficit. Note that the linear fit of the expansion rate is only a first-order approximation. Higher-order fittings are possible and can be embedded easily into the current model.

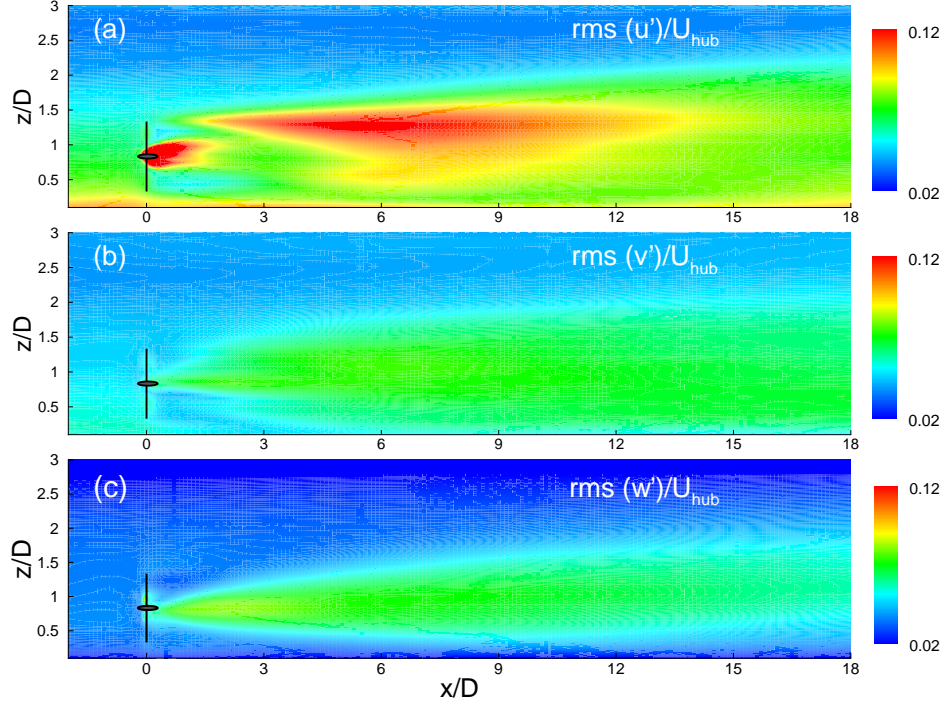


**Figure 3.13:** Turbulence intensity of Case 1: (a) streamwise component  $I_x$ , (b) spanwise component  $I_y$  and (c) vertical component  $I_z$ .

### 3.6.2 Turbulence properties

The turbulence intensity in the wake of a wind turbine is important to the performance and wind load of the wind turbines sitting behind. In Fig. 3.13, contours of the three components of the resolved turbulence intensity of Case 1 are plotted in the vertical central plane. In the near wake region, the nacelle induces a significant increase of  $I_x$  that lasts only about  $2D$  downstream. An increase in  $I_x$  also happens at the top-tip level of the rotor, which continuously increases and reaches its maximum at about  $5D$  downstream in this case and lasts until about  $15D$ . Therefore, this effect of  $I_x$  is very important to downstream wind turbines in a modern wind farm with a typical spacing of about  $8D \sim 10D$ . An interesting finding is that a low turbulence intensity region forms past the wind turbine beneath the rotor level in the wake. This decreased turbulence intensity is caused by the net effect of the reduced wind shear induced by the turbine and the background wind shear [70].

Compared with the streamwise component, the other components  $I_y$  and  $I_z$  are less significant, as expected (Fig. 3.13b and c). The spanwise intensity  $I_y$  also shows an asymmetry due to wind shear that is larger above hub height than below. At the hub-height level,  $I_y$  slightly increases not directly past the nacelle but at a distance of about  $0.5D$  downstream. The maximum of  $I_y$  occurs roughly at the same distance as  $I_x$ , at about  $6 - 7D$ , but at a vertical location that is lower than the top-tip level. The flow separation at the edge of the nacelle induces a significant increase of  $I_z$  in the near wake, while a small increase of  $I_z$  is observed at the tips of the rotor. Due to its dominance,  $I_x$  is of particular interest and will be simply referred as the turbulence intensity  $I$  in this study, as done in many other works [16].

In order to show the wind turbine effect on turbulence intensity, the added turbulence intensity can be defined as [70]:

$$\Delta I = \sqrt{I_{wake}^2 - I_\infty^2} \quad (3.24)$$

where  $I_\infty$  is the turbulence intensity in the free upstream. Although an exact description of the 3D distribution of the turbulence intensity is complex, in practice it is useful to model the maximum added turbulence intensity in a relatively simple way. As discussed earlier, the maximum always appears near the top-tip level of the annular shear layer of the wake. In the near wake region, by assuming that the production of turbulent kinetic energy (TKE) is much larger than its dissipation, Crespo and Hernández [70] proposed a theoretical expression for the maximum added turbulence intensity  $\Delta I_m$ :

$$\Delta I_m = 0.75a = 0.362[1 - (1 - C_T)^{1/2}], \quad (3.25)$$

where  $a$  is the induction factor and  $C_T$  is the thrust coefficient. In Fig. 3.14,  $\Delta I_m$  at the top-tip level within  $x < 3D$  from the LES cases are plotted with the theoretical model. In general, the WiTTS results show very good agreements with the theoretical model in the range  $0.3 < C_T < 0.6$ , where  $\Delta I_m$  increases mainly with  $C_T$  in the near wake region.

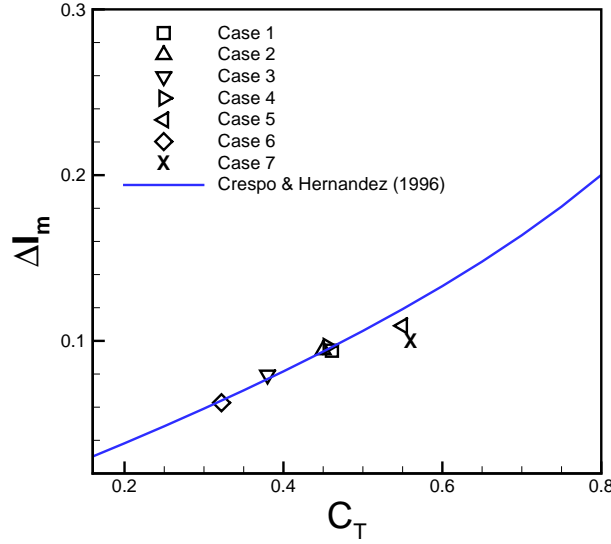


**Figure 3.14:** The maximum added turbulence intensity  $\Delta I_m$  of the LES cases v.s. the theoretical model from Crespo and Hernández (1996).

For the far wakes, by fitting the UPMWAKE results in the region  $5 < x/D < 15$  with  $0.07 < I_\infty < 0.14$ , Crespo and Hernández [70] proposed that the maximum added turbulence intensity is related to the induction factor  $a$  and free-upstream turbulence intensity  $I_\infty$  as follows

$$\Delta I_m = 0.73a^{0.8325} I_\infty^{-0.0325} \left(\frac{x}{D}\right)^{-0.32}. \quad (3.26)$$

Alternatively, Quarton [94] proposed an empirical relationship

$$\Delta I_m = 4.8C_T^{0.7} I_\infty^{0.68} \left(\frac{x}{x_N}\right)^{-0.57} \quad (3.27)$$

where  $x_N$  is the estimated length of the near wake using the definition by Vermeulen [72] as

$$x_N = \frac{\sqrt{0.214 + 0.144m}(1 - \sqrt{0.134 + 0.124m})}{(1 - \sqrt{0.214 + 0.144m})\sqrt{0.134 + 0.124m}} \frac{r_0}{dr/dx}, \quad (3.28)$$

where  $m = \frac{1}{\sqrt{1-C_T}}$ ,  $r_0 = R\sqrt{\frac{M+1}{2}}$  and  $R$  is the radius of the rotor. In Eq. 3.28,  $dr/dx$  is the expansion rate of the wake which has three contributors: ambient turbulence,  $(dr/dx)_a^2 = 2.5I_0 + 0.005$ , rotor generated turbulence,  $(dr/dx)_r^2 = 0.012B\lambda$ , and shear

generated turbulence,  $(dr/dx)_m^2 = \frac{(1-m)\sqrt{1.49+m}}{9.76(1+m)}$ , where  $B$  is the number of blades and  $\lambda$  is the rotor-tip speed ratio. A modification form of the Quarton's model based on the wind tunnel measurements was proposed by Hassan [95] as

$$\Delta I_m = 5.7C_T^{0.7}I_\infty^{0.68}\left(\frac{x}{x_N}\right)^{-0.96}. \quad (3.29)$$

Those three models are actually quite similar to each other in form considering that  $a$  and  $C_T$  are strongly linked. The biggest discrepancy is that  $\Delta I_m$  slightly decreases with  $I_\infty$  in Eq. 3.26, while it increases with  $I_\infty$  in Eq. 3.27 and 3.29. The three models are tested for all cases shown here and the results are compared with the LES data. The results are shown in Fig. 3.15, where only Case 2 is omitted since it is very close to Case 1. The LES results show that, although the incoming turbulence intensity is the same for Cases 1 to 6, the added turbulence intensities are still scattered caused by the differences in wind speed, rotation speed of rotor, or nacelle design. But all cases share a very similar pattern, i.e., the  $\Delta I_m$  increases quickly in the near wake region until it reaches a maximum, then it gradually decreases. The point where  $\Delta I_m$  is maximum varies depending on the specific case, but in general it is in the range between about 4D to 8D. It is clear that neither of the three wake models match well with the LES results in the near or intermediate wake regions. The Quarton's model overestimates the added intensity significantly, while the Crespo's model underestimates both the magnitude of the added intensity and its rate of decaying with distance. The Hassan's model appears to have better match to the LES results, but still it underestimates the magnitude in the far wake regions.

Based on the observations, a modification to the Hassan's model is proposed here as follows

$$\Delta I_m = 5.7C_T^{0.5}I_\infty^{0.68}\left(\frac{x}{x_N}\right)^{-0.96}. \quad (3.30)$$

Note that the only explicit change made here is the power of  $C_T$ . Since  $x_N$  is also a function of  $C_T$ , the change also affects the estimation of  $x_N$  for each case. As shown in Fig. 3.15 (d), although the magnitude of  $\Delta I_m$  is still underestimated in the far wake at distances greater than 16D and the rate of change is slightly overestimated, the current

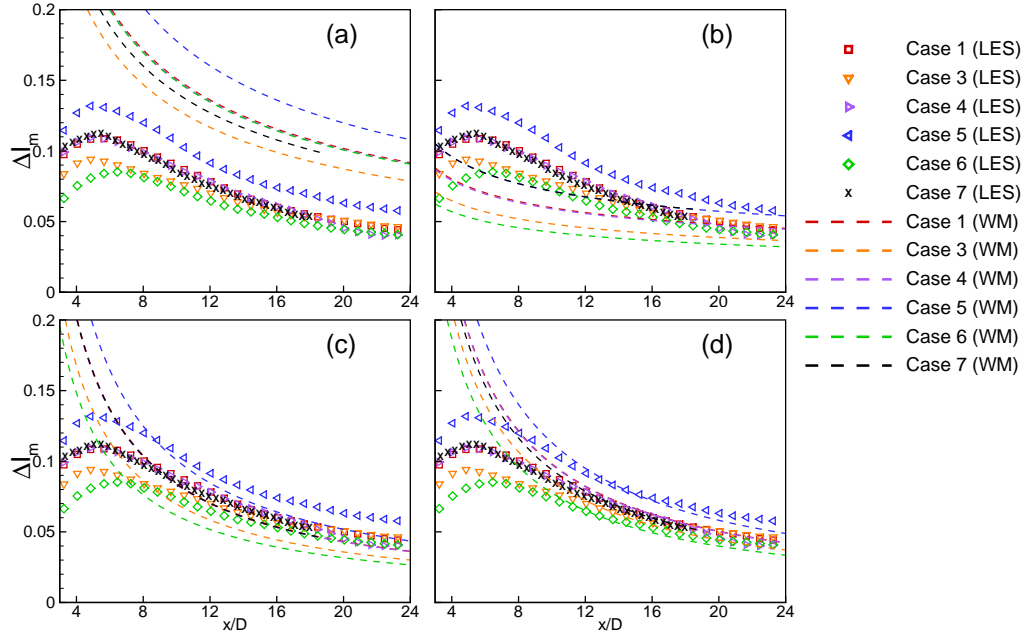


**Figure 3.15:** The added turbulence intensity at the top-tip level of rotor with comparisons of several wake models. The symbols are LES results and dashed lines are wake model results. The Quarton’s model (Eq. 3.27) is used in (a), the Crespo’s model (Eq. 3.26) is used in (b), the Hassan’s model (Eq. 3.29) is used in (c), and our new model (Eq. 3.30) is used in (d).

model improves the prediction and fits the curves of LES results better compared to the other three models. The modification is purely empirical and simple, thus a more comprehensive investigation is expected in future studies.

It is also interesting to study the budget of turbulent kinetic energy (TKE) in the wind turbine wakes. In Fig. 3.16, the following four terms of the TKE budget, averaged over Case 1 through 5, are plotted in the vertical central plane: advection of TKE by mean flow

$$-\bar{u}_j \frac{\partial k}{\partial x_j}, \quad (3.31)$$

transport of TKE by the eddies

$$-\overline{\frac{\partial k u'_i}{\partial x_i}}, \quad (3.32)$$

TKE production by shear

$$\overline{u'_i u'_j} \frac{\partial \bar{u}_i}{\partial x_j} \quad (3.33)$$

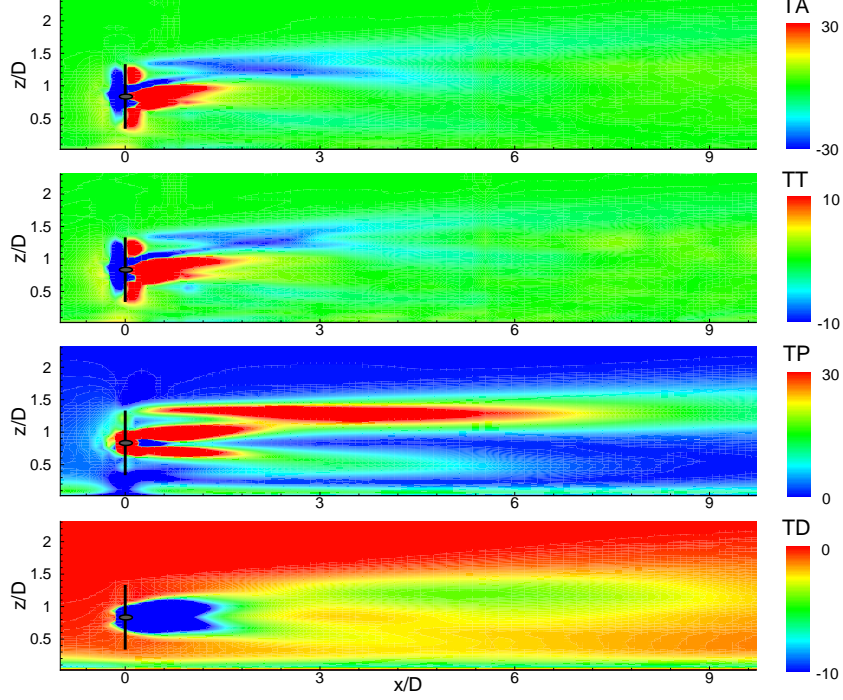


**Figure 3.16:** The budget of turbulent kinetic energy averaged over all WiTTS cases. TA: TKE advection by mean flow; TT: TKE transport by eddies; TP: TKE production; TD: TKE dissipation. All terms are normalized by the corresponding  $u_*^3/D$ .

and dissipation

$$-2\overline{\nu_r S'_{ij} S'_{ij}}, \quad (3.34)$$

where  $\overline{(\cdot)}$  denotes time average,  $k = \frac{1}{2}(\overline{(u'_1)^2} + \overline{(u'_2)^2} + \overline{(u'_3)^2})$  is TKE,  $u'_i$  is the velocity fluctuations,  $S'_{ij}$  is the rate of strain tensor of the velocity fluctuations as follows

$$S'_{ij} = \frac{1}{2} \left( \frac{\partial u'_i}{\partial x_j} + \frac{\partial u'_j}{\partial x_i} \right), \quad (3.35)$$

and  $\nu_r$  is eddy viscosity from Eq. ???. All terms are normalized by its corresponding  $u_*^3/D$  of each case.

In general, the TKE advection by the mean flow and the TKE transport by the eddies behave in a very similar manner: a large positive value after the nacelle occurs but is limited within 3D; opposite signs on either sides of the rotor are observed within 1D upwind and downwind; and a relatively strong negative value is generated at near

the top-tip level which lasts about  $5D$  downstream due to the presence of the TKE maximum at about  $5D$ . Moreover, the magnitude of the advection by mean flow is larger than the transport by eddies in the near wake region. Due to the asymmetry of the vertical wind shear, the advection and transport are both weak at the lower levels beneath the rotor.

The TKE production caused by wind shear at the top-tip level of the rotor is significant. The nacelle forms two regions of enhanced TKE production, above and below its edges. The high production region above the nacelle merges with the high production region at the top-tip level at about  $3D$ . The TKE dissipation mainly happens in the near wake region past the nacelle and is weak in the rotor region, consistent with the assumption used to derive Eq. 3.25. In the far wake, a local maximum of dissipation happens in the upper part above the hub level but below the top-tip level, whereas the dissipation near the ground appears to be unaffected by the turbine.

### 3.7 Conclusions

In this study, a new large-eddy simulation code, the Wind Turbine and Turbulence Simulator (WiTTS), is developed to study the wake generated from a single wind turbine in the neutral ABL. A scale-dependent Lagrangian dynamic model is used for the SGS stress and the actuator-line model is used to take into account the rotational effect of the rotor. The WiTTS results match well with wind tunnel measurements, although the scaling of the law-of-the-wall shows a classic "overshoot" problem near the ground. The mean velocity deficit shows good self-similarity properties following a normal distribution in the horizontal plane at the hub-height level. Self-similarity is a less valid approximation in the vertical near the ground, due to strong wind shear. The wake expansion is found to be anisotropic due to wind shear and impact with the ground, such that the wake grows faster horizontally than vertically. Several wake models of the velocity deficits are examined and compared against our LES results. A modification to the Bastankhah's model is proposed to take into account the anisotropic

expansion of the wake in a simple way by assuming two different variances in the vertical and in the horizontal directions, rather than the same one in both directions. The results show that the modification improves the prediction in the far wake regions.

Aligned with the mean wind direction, the streamwise component of turbulence intensity is the dominant one among the three components and thus it is further studied here. The highest turbulence intensity occurs near the top-tip level. The WiTTS results prove that the theoretical model proposed by Crespo and Hernández works well to predict the maximum added turbulence intensity  $\Delta I_m$  in the near wake region. In the far-wake, the LES results are used to test several wake models for the added turbulence intensity. An empirical modification is also proposed to the Hassan's model for better fitting in the far wakes. The budget of turbulence kinetic energy from the WiTTS are is also evaluated. It is found that the advection of TKE by the mean flow is important in the near wake and the transport of TKE by eddies has a similar pattern but lower magnitude. The TKE production is affected significantly by the nacelle in the near wake and at the top-tip level of the rotor, lasting several rotor diameters downstream. The TKE dissipation is relatively small in the whole wake, although it is significantly increased by the nacelle wake within 2D.

## Chapter 4

# WIND TURBINE WAKES UNDER VARIOUS ATMOSPHERIC STABILITY CONDITIONS

### 4.1 Abstract

The effects of various stability conditions in the atmospheric boundary layer (ABL) on the wakes of a single wind turbine and a small wind farm are studied with large-eddy simulations (LES). The interactions between geostrophic forcing, stability condition, and Coriolis forcing produce complex 3D structures in both mean and turbulent properties in the wind turbine/farm wakes, which also influence the ABL's temperature distribution. The wakes are significantly deformed and stretched by the wind veering corresponding to the Coriolis forces. As a result, the common assumption of Gaussian-type self-similarity of the mean velocity deficit is found to be invalid in the single turbine wake. The wind farm wakes are less developed and less deformed but have higher velocity deficits and turbulence levels than single turbine wakes. By fixing the geostrophic wind, the power extraction of the wind farm depends on trade-offs between upstream wind speed and ambient turbulence level.

### 4.2 Introduction

Wind turbine wakes, the low-wind-speed and high-turbulence flow regions behind wind turbines due to extraction of momentum from the upstream winds, are known to be the largest contributors to energy losses in wind farms [16, 4, 6]. It is therefore important to investigate wake properties in order to mitigate their negative impact. Residing in the lower part of the atmospheric boundary layer (ABL), the wind turbine wakes interact with the atmospheric dynamics in a complex way.

Wind turbine wakes have been studied primarily under the assumption of a neutral ABL, where the mean potential temperature profile is uniform and constant [34, 34, 96, 37, 97, 19]. However, neutral stability is actually rare, because in reality the ABL is always affected by buoyancy effects due to different thermal conditions [17]. Typically, when the ground is warmer than the ambient air (e.g., in daytime), the ABL is unstable since the air parcels near the ground are warmer and lighter than those above, which triggers buoyant convection with enhanced turbulence (also known as “convective boundary layer”). In contrast, when the ground is cooler than the ambient air (e.g., at night), the ABL is stable, i.e., buoyant convection and turbulence are suppressed and a low-level jet (LLJ) may occur near the top of the ABL [17].

The interactions between atmospheric stability and wind farms have been observed in various studies. Satellite data provided empirical evidence that surface temperature varies diurnally due to wind farm wakes, i.e., the surface is warmed by up to 0.72 K at night, but the warming is very weak in the daytime [14]. On the other hand, a field campaign at the San Geronio wind farm, California, indicated surface warming at night but surface cooling in daytime [12]. Similar trends have been reported from mesoscale model simulations and were attributed to enhanced turbulence mixing in the wakes [12, 13]. A mesoscale modeling study of the effects of wind farms on the ABL throughout a diurnal cycle [15] found that the impact of the wind farm can last up to 60 km downwind at night and that the LLJ is completely eliminated within the wind farm, but little impact in the daytime was observed due to the pre-existing rapid mixing. They also reported surface warming at night inside the wind farm by about 0.5 K, but cooling up to -0.3 K downwind. From power generation data, Wharton and Lundquist [98] found a correlation between power generation and stability condition, i.e., the power generated at a given wind speed at hub height is about 15% higher under the stable condition than the strong unstable condition. Similar trends have also been suggested in vertical wind profiles from meteorological tower and SODAR measurements [99]. However, the opposite finding, i.e., higher power during stable conditions, has been reported by Vanderwende and Lundquist [100] from their nacelle

wind measurements at an onshore wind farm.

The somewhat ambiguous observations indicate the need for a more careful study of the details of the interactions between the wind turbine wakes and the stability conditions, which, however, has not been performed until very recently. From wind tunnel measurements of a single miniature wind turbine under both neutral and stable conditions [83], the dependence on the stability conditions on both mean velocity deficit and turbulence intensity in the wake was shown. From high-resolution large-eddy simulations [101, 102], the details of flow structures in the near wake regions after a single turbine under two stable conditions were revealed. A more systematic LES study considering both stable, neutral, and unstable conditions on a single turbine wake was performed [103] for the first time. The wake exhibited a very asymmetric expansion in the vertical and lateral directions depending on the stability conditions, based on which an analytical wake model was proposed as a revision for the stability conditions. In their study, the wind speed is fixed at the hub height for all stability conditions and the Coriolis forcing was omitted.

Besides the single turbine, the stability effects on wind farm wakes have also been studied primarily using LES. Churchfield et al. [7] simulated wind farm wakes under both neutral and unstable conditions. They concluded that the coherent turbulent structures formed under different levels of atmospheric stability have important effects on wind turbine structural response, power production, and wake evolution. LES of infinite large wind farms (by assuming periodicity in the horizontal directions) suggested increased boundary-layer heights and decreased surface momentum and heat fluxes for both stable and unstable conditions [36, 104]. Under stable conditions [36], it was found that the Coriolis force causes skewed spatial wake structures and an increase of temperature near the ground. On the other hand, under unstable conditions, where the vertical mixing due to wind turbines is not important, the enhanced entrainment flux at the top of the boundary layer causes a decreased vertically-integrated temperature but an increased land surface temperature [104]. The effects of configuration and stability on a large but finite offshore wind farm have also been studied [105]. It was

found that, when the wind speed at hub height is fixed, in general the total power increases as the ABL becomes more unstable due to faster wake recovery, but not always, since local effects, such as wind acceleration between two adjacent turbines, become important under some particular layout designs and stability conditions.

Despite the great progress gained, previous studies have been limited in several aspects. On one hand, besides the variations in turbulence levels and vertical wind shear, the stability effects are strongly coupled with other important factors in a real ABL that may influence the wake properties, such as the Coriolis forcing, geostrophic forcing, and surface heat and momentum fluxes. On the other hand, it is unclear how the overlaps between multiple wakes differ from the single turbine wake scenario under various stability conditions. Therefore, we aim to go a little further in both directions in this LES study. Similar to the work of Abkar and Porté-Agel [103], stable, neutral, and unstable conditions are considered here. The geostrophic wind speed at the top of the ABL [106, 36] and the Coriolis frequency are fixed for all stability conditions. The wind speed as well as the wind direction inside the ABL are allowed to evolve with height according to the balance between geostrophic, Coriolis, and stability-related shear forcings. Moreover, both a single wind turbine and a finite wind farm with five turbines aligned in the streamwise direction are simulated in this study.

The paper is organized as follows: Section 4.3 briefly describes the numerical methods; some validation cases are shown in Section 4.4; the ABL properties are discussed in Section 4.5; the detailed results, including mean flow properties, turbulence statistics and vortical structures, for both the single turbine case and wind farm case are presented and discussed in Section 4.6; at last, conclusions are given in Section 4.7.

### 4.3 Numerical Methods

In this study, the Wind Turbine and Turbulence Simulator (WiTTs) developed at the University of Delaware is used. The base version of WiTTs is an LES solver of the 3D, unsteady, incompressible, neutral ABL with wind turbines inside. The

Navier-Stokes equations are solved by the fractional-step method [59] in the finite-difference framework, where a fourth-order, fully conservative, central scheme [46] is used for the convective term in the skew-symmetric form. The Poisson equation for pressure is solved by a fourth-order multigrid method [60]. The subgrid-scale (SGS) motions are modeled by the Lagrangian-average scale-dependent (LASD) model [32] with test and second test filterings in the physical space using a box filter. The wind turbine is modeled by the actuator line model, as introduced in Section 3.3.2 [79]. The simulations are parallelized by domain decomposition using Message Passing Interface (MPI). More details and some validations of WiTTS can be found in [19] and [18].

In order to take the stability and the Coriolis effects into account, following [36], the governing equations of WiTTS are slightly modified as follows

$$\frac{\partial \tilde{u}_i}{\partial t} + \tilde{u}_j \frac{\partial \tilde{u}_i}{\partial x_j} = -\frac{1}{\rho} \frac{\partial p^*}{\partial x_i} - \frac{\partial \tau_{ij}}{\partial x_j} + \delta_{i3} g \frac{\tilde{\theta} - \langle \tilde{\theta} \rangle}{\theta_0} + f_c \varepsilon_{ij3} (\tilde{u}_i - U_{gi}) + f_i, \quad (4.1)$$

plus the continuity constraint

$$\frac{\partial \tilde{u}_i}{\partial x_i} = 0. \quad (4.2)$$

Here  $\tilde{u}_i (i = 1, 2, 3)$  is the filtered fluid velocity,  $\rho$  is the (constant) air density,  $p^*$  is the modified pressure including the trace part of the stress tensor,  $\tau_{ij}$  is the deviatoric part of the SGS stress tensor,  $\tilde{\theta}$  is the resolved potential temperature,  $\theta_0$  is the reference temperature,  $\langle \cdot \rangle$  represent a horizontal average,  $g = 9.8$  m/s is the gravitational acceleration,  $f_c$  is the Coriolis parameter,  $U_{gi}$  is the geostrophic wind,  $\varepsilon_{ijk}$  is the alternating unit tensor, and  $f_i$  is the body force for the actuator line model [79, 19]. Note that the Boussinesq approximation is used here for the buoyancy term (the third term on the RHS of Eq. 4.1) due to stability, and a filtered transport equation for potential temperature is coupled as follows:

$$\frac{\partial \tilde{\theta}}{\partial t} + \tilde{u}_j \frac{\partial \tilde{\theta}}{\partial x_j} = -\frac{\partial q_j}{\partial x_j}, \quad (4.3)$$

where  $q_j = \tilde{u}_j \tilde{\theta} - \tilde{u}_j \tilde{\theta}$  is the SGS heat flux that needs to be modeled.

Eq. 4.3 is integrated in time by a fourth-order four-stage Runge-Kutta method, and the nonlinear term is discretized by the fourth-order fully conservative central scheme [46]. The SGS heat flux can be modeled by the eddy-viscosity approach as

$$q_j = -D_T \frac{\partial \tilde{\theta}}{\partial x_i} = -\frac{\nu_T}{Pr_{SGS}} \frac{\partial \tilde{\theta}}{\partial x_i}, \quad (4.4)$$

where  $D_T$  is the SGS eddy diffusivity for heat,  $\nu_T$  is the SGS eddy viscosity for momentum fluxes, and  $Pr_{SGS}$  is the SGS Prandtl number. Although  $D_T$  can be obtained in the same LASD manner as  $\nu_T$  [107, 36], we prefer to use the LASD model for  $\nu_T$  only but prescribe a constant  $Pr_{SGS}$  here to obtain  $D_T$ , in order to save computational cost [7, 105].

On the ground surface, a wall model following the Monin-Obukhov similarity theory is embedded for the momentum shear stress as follows [108, 36],

$$\tau_{i3,wall} = -\left(\frac{u_r \kappa}{\ln(z/z_0) - \Psi_M}\right)^2 \frac{\tilde{u}_i}{u_r} \quad (i = 1, 2). \quad (4.5)$$

Here,  $\tilde{u}_i$  is the instantaneous local velocity component at the first point of the wall ( $z = \Delta_z/2$ ),  $u_r = \sqrt{\tilde{u}_1^2 + \tilde{u}_2^2}$ ,  $\kappa = 0.41$  is the von Kármán constant,  $z_0$  is the surface roughness height and set to be 0.016 m in all cases, and  $\Psi_M$  is the correction for the stability condition with the local Obukhov length  $L = -\frac{u_*^3 \tilde{\theta}}{\kappa g q_{3,wall}}$  (where  $u_*$  is the friction velocity and  $q_{3,wall}$  is the surface heat flux). For the stable conditions,  $\Psi_M = -4.8 \frac{z}{L}$  was suggested in [106]; for the unstable conditions, following Stull [17] and Arya [109],  $\Psi_M = 2 \ln\left(\frac{1+X}{2}\right) + \ln\left(\frac{1+X^2}{2}\right) - 2 \tan^{-1}(X) + \frac{\pi}{2}$  is used, where  $X = \left(1 - 15 \frac{z}{L}\right)^{1/4}$ .

Similarly, a wall model for the surface heat flux is used for the stable conditions as follows,

$$q_{3,wall} = \left(\frac{u_* \kappa (\theta_s - \tilde{\theta})}{\ln(z/z_0) - \Psi_H}\right)^2, \quad (4.6)$$

where  $\theta_s$  is the prescribed surface temperature,  $\tilde{\theta}$  is the instantaneous local temperature at the first point of the wall, and  $\Psi_H = -7.8 \frac{z}{L}$  is used for the stable conditions [108, 36] (although  $\Psi_H = 2 \ln\left(\frac{1+X^2}{2}\right)$  was proposed for the unstable conditions [17, 109], it is not used here since  $q_{3,wall}$  is proscribed). Eqs. 4.5 and 4.6 are linked in a nonlinear way and they are solved by an iteration process in the simulations.

## 4.4 Validations of WiTTS under Various Stability Conditions

In this section, the version of WiTTS including the Coriolis and stability effects is validated by simulating the following two cases: the first is a buoyancy-driven convective planetary boundary layer (PBL) used in Moeng and Sullivan [110], where the turbulence generated by buoyancy is dominant; The second case is a moderately stable ABL following the GABLS (GEWEX Atmospheric Boundary Layer Study) initiative [106], where the turbulence generated by wind shear is dominant. Both cases are without wind turbines.

### 4.4.1 Convective planetary boundary layer

Following [110], the domain size is  $5 \text{ km} \times 5 \text{ km} \times 2 \text{ km}$  in the  $x$ ,  $y$  and  $z$  directions with the resolution of  $N_x \times N_y \times N_z = 96 \times 96 \times 96$ , respectively. The total physical time of the simulation is 9000 s, the surface heat flux  $q_{3,wall} = 0.24 \text{ Km/s}$ , geostrophic wind speeds  $(U_g, V_g) = (10, 0) \text{ m/s}$  and Coriolis frequency  $f_c = 1 \times 10^{-4} \text{ s}^{-1}$ . The initial potential temperature is 300 K below the initial boundary layer height of 937 m and increases by a total of 8 K across  $6\Delta z$ , and it increases with a lapse rate of 3 K/km above. More details of the problem setup can be found in [110]. Two  $Pr_{SGS}$  values of 0.5 and 1.0 are tested here. Time- and horizontal-averaged simulation results from both WiTTS and the literature are compared in Fig. 4.1. In general, the current LES data match well with the literature. Note that the momentum fluxes are normalized by the square of the Deardorff convective velocity  $w_*$  defined as [110]

$$w_* = \left( \frac{g}{\theta_0} q_{3,wall} z_i \right)^{1/3}. \quad (4.7)$$

Here,  $z_i$  is the PBL height diagnosed using the “maximum gradient method” [1] at every time step. A relatively large deviation of the mean spanwise velocity  $V$  is observed in the lower part of the PBL. The LES results from WiTTS are not very sensitive to the value of  $Pr_{SGS}$  for the convective PBL, where the turbulence diffusivity is strong. Even when the literature data are not available, such as in Fig. 4.1 (b) and (d), the profiles from both  $Pr_{SGS} = 0.5$  and 1.0 are well collapsed, although small

Model	References
CORA	Sullivan et al. [111] and Koren [112]
IMUK	Raasch and Etling [113] and Raasch and Schröter [114]
LLNL	Kosovic [115]
UIB	Cuxart et al. [116]
WU	Cuijpers and Duynkerke [117] and Dosio et al. [118]
MO	Brown et al. [119] and Beare and MacVean [120]

**Table 4.1:** References for some models in the GABLS cases.

deviations in  $\Theta$  are observed at about  $z/z_i = 1.0$ , where the vertical gradient of  $\Theta$  is large. A slightly better match of the normalized momentum flux is observed for  $Pr_{SGS} = 1.0$  than that for  $Pr_{SGS} = 0.5$  (Fig. 4.1 (c)). Therefore, in the rest of this study of unstable ABL,  $Pr_{SGS} = 1.0$  will be used. Hereafter,  $\langle \dots \rangle$  represents a horizontal average, overbar denotes the time average, and the time- and horizontal-averaged velocities and potential temperature are presented in the upper cases, and the tilde hat is omitted for the resolved properties for simplicity.

#### 4.4.2 Stable atmospheric boundary layer: the GABLS case

Compared to the convective PBL, the simulation of a stable ABL is well known to be more challenging, since turbulence dissipation is suppressed and therefore the results are more sensitive to numerical errors. According to the GABLS description, the domain size is  $400 \text{ m} \times 400 \text{ m} \times 400 \text{ m}$  in the  $x, y$  and  $z$  directions, with a initial potential temperature profile consisting of a mixed layer (with potential temperature 265 K) up to 100 m with an overlying inversion of strength 0.01 K/m above. Prescribed surface cooling of 0.25 K/h, geostrophic wind speed of  $(U_g, V_g) = (8, 0) \text{ m/s}$  and the Coriolis frequency of  $f_c = 1.39 \times 10^{-4} \text{ s}^{-1}$  (corresponding to latitude  $73^\circ \text{ N}$ ) are applied for 9 h, and the statistics are performed over the last hour. A large amount of data are available from various participants of the GABLS project and can be found online at <http://gabls.metoffice.com/>, and some of them are selected here to compare with the WiTTS results, as shown in Table 4.1. A good summary and intercomparison of

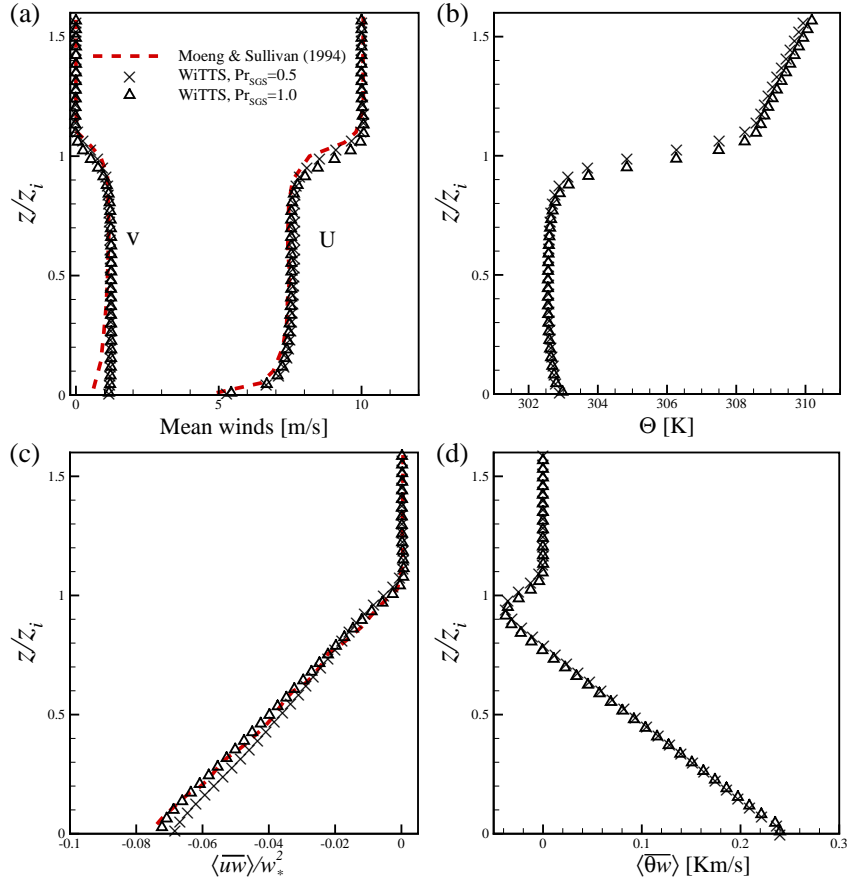


**Figure 4.1:** Vertical profiles of time- and horizontal-averaged (a) wind speeds, (b) potential temperature  $\Theta$ , (c) normalized total momentum flux (resolved + SGS terms) and (d) total heat flux (resolved + SGS terms) of the Convective PBL using two  $Pr_{SGS}$  values compared with the data from literature [1]. Note that the literature data were not available in (b) and (d).

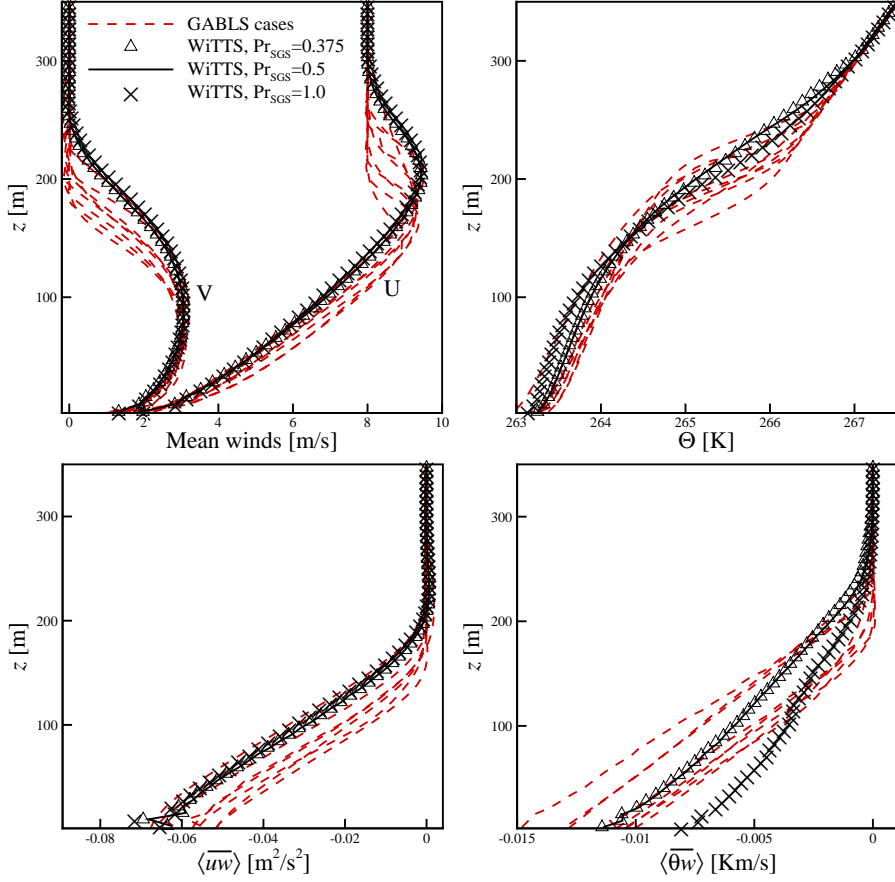


**Figure 4.2:** Vertical profiles of time- and horizontal-averaged (a) wind speeds, (b) potential temperature  $\Theta$ , (c) total momentum flux (resolved + SGS terms) and (d) total heat flux (resolved + SGS terms) of the stable ABL simulations using three  $Pr_{SGS}$  values compared with the data from the GABLS cases.

those models have been given in [106]. In all simulations, resolution of 6.25 m in each direction is used monotonically. Three  $Pr_{SGS}$  values (0.375, 0.5 and 1.0) are considered here in the current LES for comparison.

In Fig. 4.2, several time- and horizontal-averaged profiles, i.e., the mean winds (streamwise and spanwise components), mean potential temperature, momentum flux  $\langle \overline{uw} \rangle$  and heat flux  $\langle \overline{\theta w} \rangle$ , are compared between the current results and the GABLS cases. Unlike the convective PBL in Section 4.4.1, a clear dependence of the results on the values of  $Pr_{SGS}$  is observed. When  $Pr_{SGS} = 0.375$  and 0.5 are used, the results

are almost collapsed and fall within the envelop of the GABLS cases. Meanwhile, for  $Pr_{SGS} = 1.0$ , large discrepancies are observed especially for profiles of  $\Theta$  and heat flux. Therefore, in the rest of this study of stable ABL,  $Pr_{SGS} = 0.5$  will be used.

The wind directions have been clearly veered at different heights due to the Coriolis effect and an obvious low-level jet (LLJ) is formed in  $U$  at about 200 m, which is one of the distinctive characteristics in the stable ABL caused by the momentum balance between the Coriolis force and vertical divergence of momentum flux [121], whereas the spanwise component  $V$  has a maximum below 100 m. The vertical profiles of the mean temperature reveal varying curves with height, while a linear behaviour is observed in the momentum and heat fluxes. Those complex features have been successfully captured by WiTTS. Moreover, various models produced scattered results for both mean and turbulence properties. Consistent with the observations in [106], the main deviations occur at the top of the boundary layer, but less in the lower part where the wind turbines may sit in. Given the difficulty of simulating the stable ABL, which is very sensitive to the numerical configuration, the current results indicate a notable success of WiTTS.

#### 4.5 Atmospheric Boundary Layers without Wind Turbines

The simulations are divided into two stages: first, the precursor stage, in which the fully developed ABL is generated without the presence of any wind turbine. The horizontal periodicity is assumed at this stage. Second, the formal stage, in which the wind turbines are added and the flow information from the precursor simulations is provided as initial and inflow conditions.

In this section, the atmospheric boundary layers simulated in the precursor stage are introduced. The computational domain size is  $L_x \times L_y \times L_z = 640 \text{ m} \times 640 \text{ m} \times 640 \text{ m}$  in the streamwise, spanwise and vertical directions, respectively, with the number of grid points  $N_x \times N_y \times N_z = 96 \times 96 \times 96$ . The transport and variability from flow scales larger than the domain size are neglected. Three different stability conditions are considered, i.e. stable, neutral, and unstable. For stable and unstable conditions,

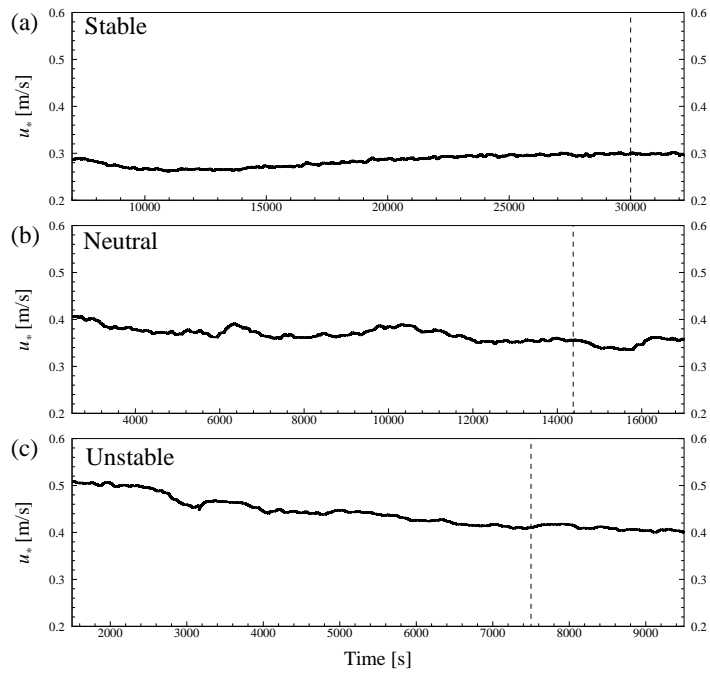


**Figure 4.3:** History of  $u_*$  averaged over the horizontal plane for (a) stable, (b) neutral and (c) unstable ABLs. The black dashed lines represent the starting time of performing statistics and formal simulations.

the initial potential temperature profile is prescribed to be 300 K constantly from the ground up to 200 m with an overlying inversion of strength 0.01 K/m aloft, while in the neutral the constant 300 K is prescribed everywhere. The Coriolis frequency is set to be  $f = 1.03 \times 10^{-4} \text{ s}^{-1}$  for all conditions. The geostrophic wind is fixed as  $U_g = 11.0 \text{ m/s}$  and  $V_g = 0.0 \text{ m/s}$  in the streamwise and spanwise directions above 450 m by a Rayleigh damping layer, which also absorbs the gravity waves [36, 106]. The periodic boundary condition is used in all horizontal directions, and the stress-free/flux-free condition is used at the upper boundary. For the bottom boundary, the surface temperature decreases with a constant rate of  $-0.25 \text{ K/h}$  in the stable ABL, and the constant surface heat flux  $q_{3,\text{wall}} = +0.04 \text{ Km/s}$  is used for the unstable condition.  $Pr_{SGS} = 0.5$  and  $1.0$  are used in the stable and unstable ABLs, respectively, according to the sensitivity tests from Section 4.4. The physical time is about 9.3 hours in the stable ABL, 6.5 hours in the neutral ABL, and 5.0 hours in the unstable ABL, respectively, and statistics are performed over roughly the last 2000 s for all conditions, where the simulations are in quasi-equilibrium, as shown in Fig. 4.3.

In Fig. 4.4 (a), the vertical profiles of the time- and spatial-averaged horizontal velocity components are plotted for the three stability conditions. Although the geostrophic wind is fixed above, the variability in the lower part of the boundary layer is seen according to the stability. For the streamwise component  $U$ , which is dominant over the three components ( $W$  is not shown), the wind shear increases with more stable conditions, which is consistent with Abkar and Porté-Agel [103]. Moreover, the wind veering, i.e., change of wind directions at different heights caused by the balance between the Coriolis, shear stress, and geostrophic forcing, is most noticeable in the stable ABL, especially at the height of the rotor region of the wind turbine. To force the wind turbine to face the wind direction at hub height, following Lu and Porté-Agel [36], we rotate the horizontal wind field accordingly in the formal simulations. The rotated wind speed profiles are shown in Fig. 4.4 (b), where the subscript  $R$  means “rotated”. After the rotation, the spanwise component  $V_R$  is null at hub height but has opposite signs above and below the hub height (negative above and positive below

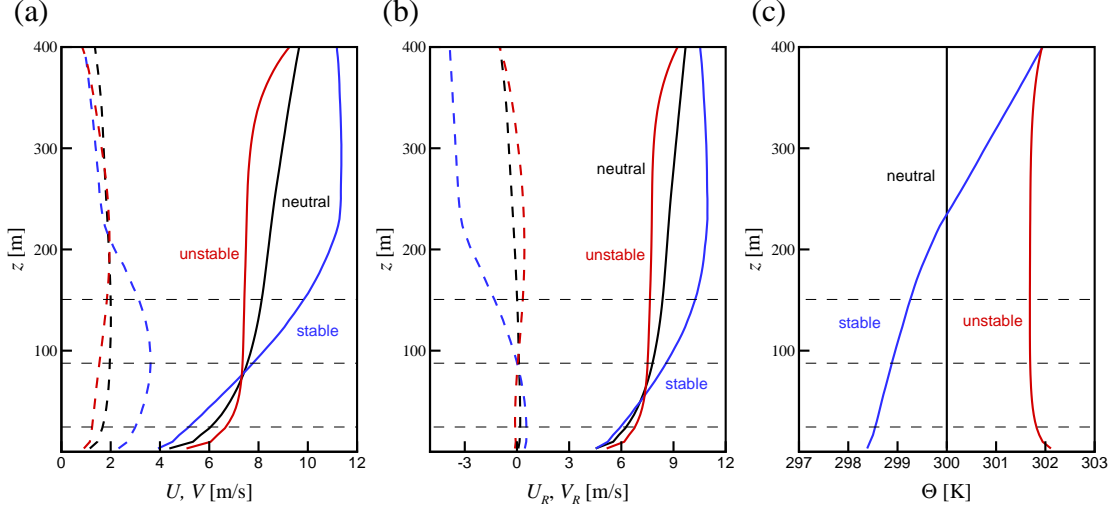


**Figure 4.4:** Vertical profiles of time- and horizontal-averaged (a) velocity components  $U$  (solid lines) and  $V$  (dashed lines), (b) rotated velocity components  $U_R$  (solid lines) and  $V_R$  (dashed lines), and (c) potential temperature  $\Theta$  for stable (blue), neutral (black), and unstable (red) ABLs. The thin dashed black lines represent the top-tip, hub, and bottom-tip levels of the wind turbine, respectively.

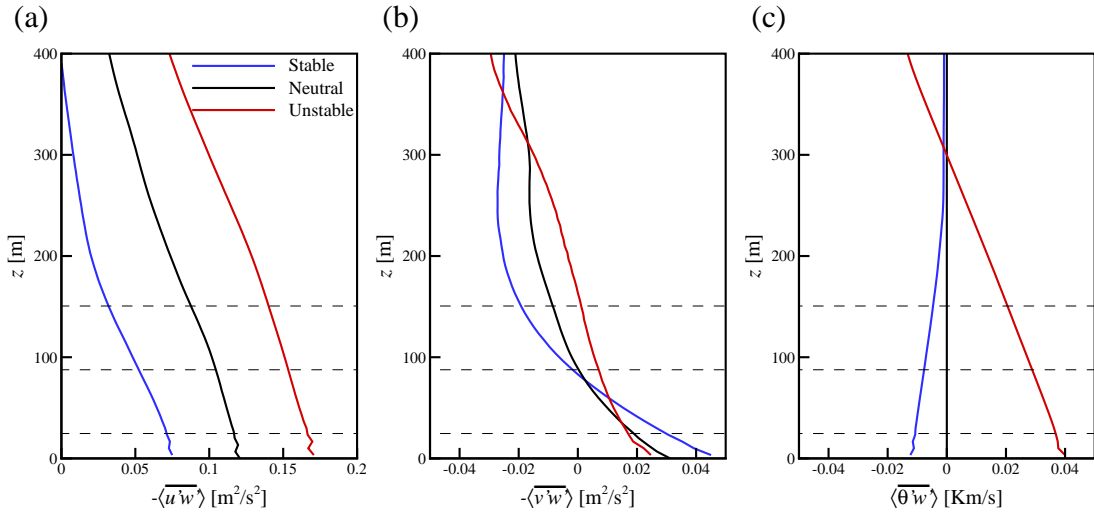


**Figure 4.5:** Vertical profiles of time- and horizontal-averaged kinematic shear stresses (a)  $-\langle u'w' \rangle$ , (b)  $-\langle v'w' \rangle$ , and (c) heat flux  $\langle \theta'w' \rangle$  for ABLs under various stability conditions. The thin dashed black lines represent the top-tip, hub, and bottom-tip levels of the wind turbine, respectively.

Stability	$U_{hub}$ (m/s)	$U_{hub}^R$ (m/s)	$\alpha$ (degree)	$\tau_{wall}$ (m <sup>2</sup> /s <sup>2</sup> )	$q_{3,wall}$ (Km/s)	$L$ (m)
Stable	8.24	8.42	23.5	0.084	-0.0115	156.4
Neutral	7.6	7.8	14.9	0.13	0.0	$\infty$
Unstable	7.4	7.5	10.9	0.17	0.04	-137.9

**Table 4.2:** Some parameters of the various stability conditions. Here,  $U_{hub}$  and  $U_{hub}^R$  are the mean streamwise velocities at the hub height before and after the rotation, respectively,  $\alpha$  is the rotation angle, and  $\tau_{wall} = (\tau_{13,wall}^2 + \tau_{23,wall}^2)^{1/2}$  is the total wall shear stress.  $L$  is the Obukhov length.

for the stable and neutral conditions, but positive above and negative below in the unstable ABL). The streamwise component  $U_R$  at hub height has the maximum value in the stable ABL and it is slightly higher in the neutral than in the unstable case. The vertical profiles of time- and spatial-averaged potential temperature under the three stability conditions are plotted in Fig. 4.4 (c). A large temperature gradient appears in the lower part of the stable ABL, whereas the profile is almost constant in the unstable ABL due to the stronger turbulence mixing and the higher mixing layer compared to the stable case.

The vertical profiles of time- and spatial- averaged total shear stresses and heat flux for the three stability conditions are plotted in Fig. 4.5. They are calculated by the summation of the resolved, SGS, and wall-model components. The profiles of the streamwise stress  $\tau_{13}$  (Fig. 4.5 (a)) show a linear behavior for all conditions, but the magnitude decreases for more stable conditions. Due to the wind veering, the averaged spanwise stress  $\tau_{23}$  is non-zero near the ground (Fig. 4.5 (b)), which is largest in magnitude in the stable ABL. The heat flux (Fig. 4.5 (c)) is zero in the neutral ABL as expected, but negative in the stable ABL and positive in the unstable ABL. More parameters are presented in Table 4.2.

## 4.6 Atmospheric Boundary Layers with Wind Turbines

In formal runs, two cases are investigated under the three stability conditions:

- A) An isolated single turbine;
- B) A wind farm consisting of five turbines aligned in the streamwise direction.

Both cases use non-periodic boundary conditions where the inflow and initial conditions come from the precursor simulations, as shown in Section 4.5. As mentioned earlier, in all cases the horizontal wind components are rotated in order for the wind turbines to face the maximum wind speed at hub height. Hereafter, all results are based on the rotated coordinates and the subscript  $R$  is dropped for simplicity.

The wind turbine used here is the RePower 5 MW horizontal-axis wind turbine. The hub height is 87.6 m and the diameter of the rotor is  $D = 126$  m. The tip speed ratio is fixed as  $\lambda = \Omega \frac{D}{2} / U_D = 5.3$  for all simulations, where  $\Omega$  is the rotational speed of the rotor, and  $U_D$  is the streamwise velocity average over the rotor-disk region  $0.5D$  upstream.

#### 4.6.1 Single-turbine wakes

The single-turbine simulations use the same domain size and resolution as the precursor simulations except in the  $x$  direction, where the domain is elongated to  $L_x = 1920$  m with  $N_x = 288$  correspondingly. The initial condition is generated by simply duplicating the flow field in the  $x$  direction from the precursor simulations, thanks to the periodic boundary conditions used. The wind turbine is located at  $x_0 = 250$  m,  $y_0 = 320$  m. The data of the last hour from the precursor simulations are used as inflow conditions, and the statistics are performed over the last half hour for all simulations here.

Consistent with Abkar and Porté-Agel [103], the normalized time-averaged resolved velocity  $\bar{u}/U_{hub}$ , where the overbar denotes the time average and  $U_{hub}$  is the time- and space-averaged inlet wind speed at hub height, shows a strong dependence on the atmospheric stability (Fig. 4.6). The wake is longest in the stable ABL (Fig. 4.6 (a)) due to reduced turbulence mixing, is shorter in the neutral ABL (Fig. 4.6 (b)), and it recovers fastest when the ABL is unstable (Fig. 4.6 (c)) where the ambient turbulence is enhanced by buoyant convection.

As shown in Fig. 4.6, in the stable ABL, the wake barely expands in the vertical direction and the lower edge of the wake does not contact with the ground. In the

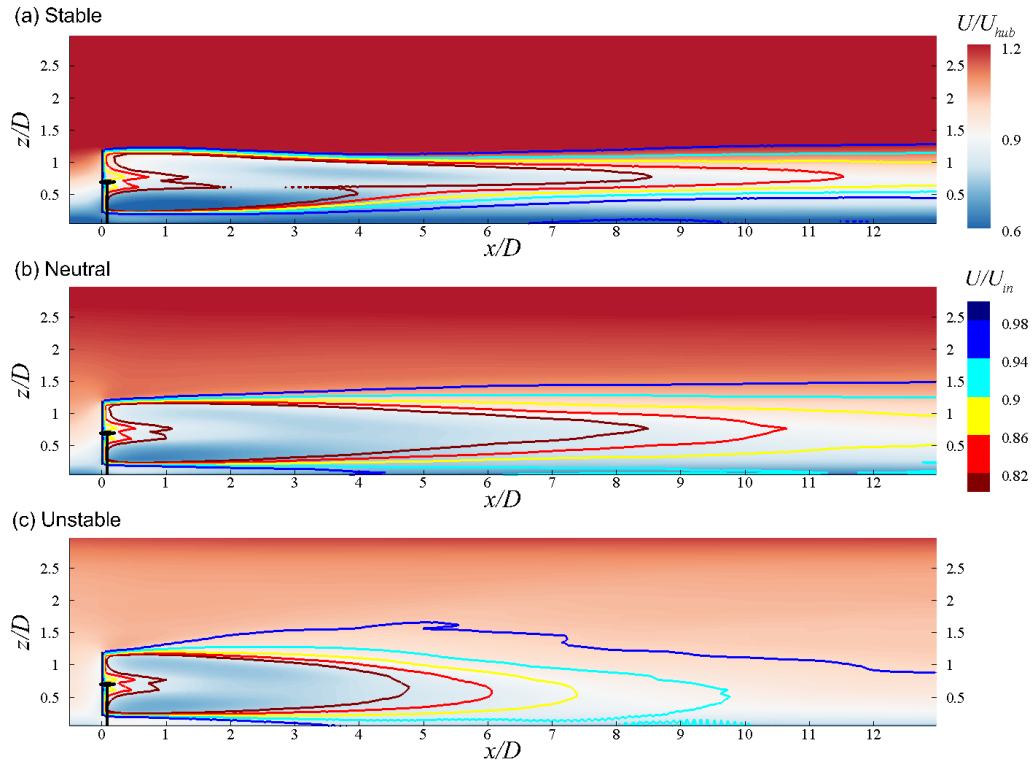


**Figure 4.6:** Contours of non-dimensional time-averaged streamwise velocity component  $\bar{u}/U_{hub}$  in the vertical central plane of single turbine wakes under various stability conditions. The colored lines represent the streamwise velocity relative to  $U_{in}$ , the time-averaged values at the same  $(y, z)$  coordinates but at  $x/D \approx -2.0$ .

neutral ABL, the wake slowly expands in the vertical direction and the contact with the ground occurs at about  $4.0D$ . In the unstable ABL, the vertical expansion of the wake is fast in the near wake region and the contact happens around  $3.0D$ . The wake reaches a maximum height at about  $5 - 6D$ , after which it decreases as a result of the wake recovery.

Complex 3D structures are formed in the wind turbine wakes as shown in mean velocity components in the  $y - z$  planes (Fig. 4.7), due to both wake rotation and wind veering. In the stable ABL, a strong vertical gradient of the lateral velocity component exists, i.e.,  $\bar{v}$  is negative above the hub-height level, and positive below, due to the wind veering, as discussed in Section 4.5. Correspondingly, the wake is significantly stretched in the lateral direction (opposite above and below the hub height level) with the wake propagation, which is also found in [36]. The stretching of the wake enhances its lateral mixing, which also helps the recovery of THE velocity deficit. The stretch is less evident in the neutral and unstable ABLs due to weaker wind veering and faster turbulence mixing. Note that, in the unstable ABL, the stretching is in the opposite direction than in the stable ABL, but at  $x/D = 10.0$  the velocity deficit is much weaker.

Moreover, the wake rotation plays an important role in skewing the velocity deficit distribution in the near wake regions ( $x/D = 1.2$  in Fig. 4.7). The velocity deficit is larger on one side of the rotor region coinciding with upward motions of the velocity vectors. As the mean wind is vertically sheared, the upward motion advects air with lower momentum from lower heights to upper heights, while the opposite occurs on the other side. Since the mean wind shear increases with more stable conditions, the skewness is strongest in the stable ABL. At further downstream, the wake rotation is gradually dissipated but it lasts much longer in the stable ABL.

In most wake models [73, 75, 74, 92, 19, 103], the self-similarity of the mean velocity deficit in the wake has been used as a fundamental assumption and has been verified yielding a Gaussian shape by previous LES studies without consideration of the Coriolis force [19, 103]. However, the Gaussian-type self-similarity assumption becomes questionable considering the skewing and stretching of the wakes. As shown in the left

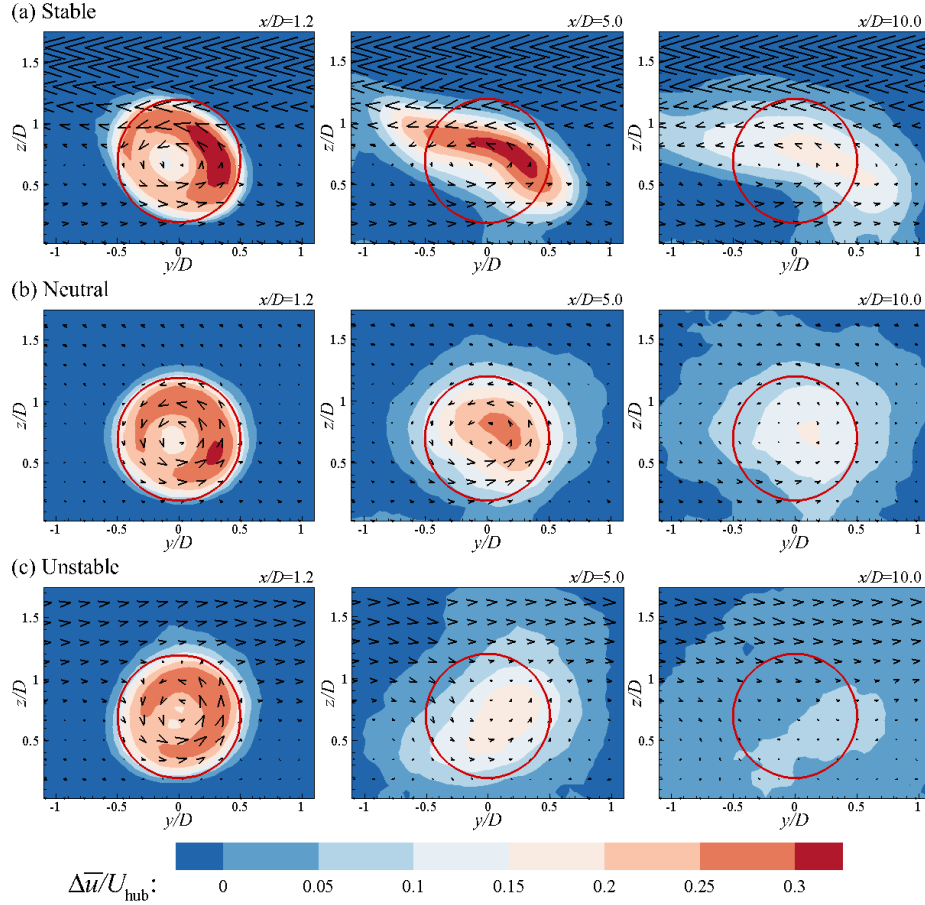


**Figure 4.7:** Structures of single turbine wakes in the  $y - z$  planes at several downstream locations for various stability conditions. The contours are the time-averaged streamwise velocity deficit  $\Delta\bar{u}/U_{hub}$  and the velocity vectors (only lateral and vertical velocity components, i. e.,  $\bar{v}$  and  $\bar{w}$ ) are plotted at every  $3 \times 3$  points. The rotor region of the turbine is represented by the red circle.

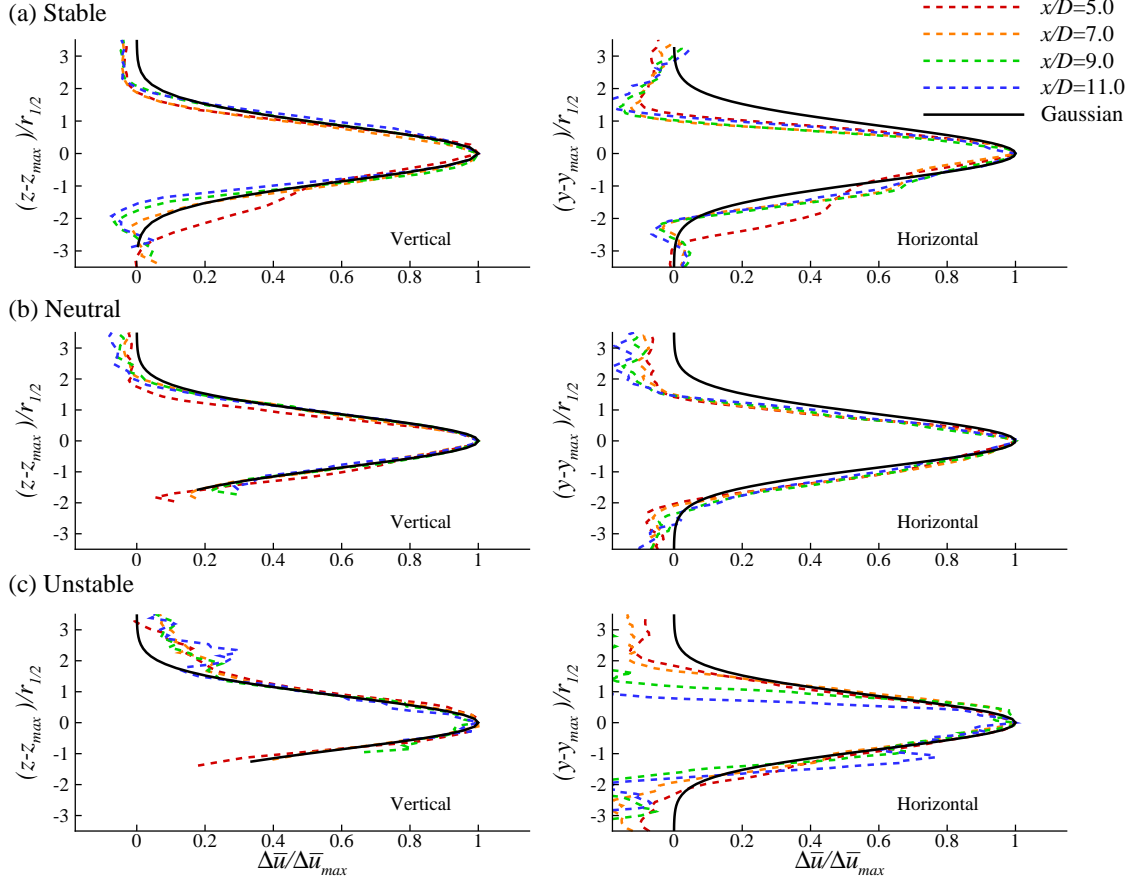


**Figure 4.8:** Self-similarity profiles of time-averaged resolved streamwise velocity deficit of single turbine wakes under various stability conditions in the vertical central plane (left column) and in the horizontal plane at hub-height level (right column). The velocity deficits are normalized by the maximum value of each profile, and the y-axis is the distance to the location where the maximum value occurs and normalized by the half-width  $r_{1/2}$ . The analytical Gaussian profile is presented by the black solid line.

column of Fig. 4.8, in the vertical direction, the normalized profiles collapse well to the Gaussian profile, although deviations near the ground surface and the upper edge of the wake are discernible due to strong vertical wind shear, consistent with previous observations [19].

On the other hand, in the horizontal plane at the hub-height level (right column of Fig. 4.8), when the ABL is stable, the normalized velocity deficit profile at the distance of  $x/D = 5$  still reveals a significant “near-wake” impact that differs drastically from further downstream profiles. At far-wake regions, the profiles are almost collapsed, but to a shape skewed from the Gaussian profile as a result of the lateral stretching. In the neutral ABL, since the wind veering is much weaker, the normalized profiles are much closer to the Gaussian function, although deviations are still discernible. In the unstable ABL, the magnitudes of velocity deficits are weak in the far-wake regions and turbulence is strong, which causes some wiggling in the profiles, but the deviations are observable. In general, the Gaussian-type self-similarity is not valid when stability and wind veering are important.

Statistically, for a time-averaged property  $\phi(x, y, z)$  in the wake (e.g., streamwise velocity deficit), the following calculation can be performed in every  $y - z$  plane:

$$\phi_M = \frac{\int_{-\infty}^{\infty} \int_{-\infty}^{\infty} \phi dydz}{\int_{-\infty}^{\infty} \int_{-\infty}^{\infty} dydz}, \quad (4.8)$$

$$\mu_y = \frac{\int_{-\infty}^{\infty} \int_{-\infty}^{\infty} (y - y_c) \phi dydz}{\int_{-\infty}^{\infty} \int_{-\infty}^{\infty} \phi dydz}, \quad \mu_z = \frac{\int_{-\infty}^{\infty} \int_{-\infty}^{\infty} (z - z_c) \phi dydz}{\int_{-\infty}^{\infty} \int_{-\infty}^{\infty} \phi dydz}, \quad (4.9)$$

$$\sigma_y^2 = \frac{\int_{-\infty}^{\infty} \int_{-\infty}^{\infty} (y - y_c - \mu_y)^2 \phi dydz}{\int_{-\infty}^{\infty} \int_{-\infty}^{\infty} \phi dydz}, \quad \sigma_z^2 = \frac{\int_{-\infty}^{\infty} \int_{-\infty}^{\infty} (z - z_c - \mu_z)^2 \phi dydz}{\int_{-\infty}^{\infty} \int_{-\infty}^{\infty} \phi dydz}, \quad (4.10)$$

$$\Gamma_y = \frac{\int_{-\infty}^{\infty} \int_{-\infty}^{\infty} (y - y_c - \mu_y)^3 \phi dydz}{\int_{-\infty}^{\infty} \int_{-\infty}^{\infty} \phi dydz}, \quad \Gamma_z = \frac{\int_{-\infty}^{\infty} \int_{-\infty}^{\infty} (z - z_c - \mu_z)^3 \phi dydz}{\int_{-\infty}^{\infty} \int_{-\infty}^{\infty} \phi dydz}, \quad (4.11)$$

where  $y_c$  and  $z_c$  are  $y$  and  $z$  coordinates of the rotor center,  $\phi_M$  is the mean value of the variable in the plane,  $\mu_y$  and  $\mu_z$  denote deviations of the function center from the rotor center,  $\sigma_y^2$  and  $\sigma_z^2$  are variances in the  $y$  and  $z$  directions, and  $\Gamma_y$  and  $\Gamma_z$  are the

skewness in the  $y$  and  $z$  directions. The variances represent the growth of the wake, and the skewness is a quantification of the asymmetry of the wake from the Gaussian distribution.

As presented in Fig. 4.9 (a), the differences in mean velocity deficits caused by stability are not clear in the very near wake regions (e.g., before  $0.6D$ ), but they are more revealed downstream. For most of the downstream region, wake recovery is fastest in the unstable ABL. Meanwhile, the mean velocity deficit is higher in the stable ABL than in the neutral ABL, but the two curves becomes very close in the far wake regions (e.g.,  $> 10D$ ). In Fig. 4.9 (b), clear deviations of the deficit center from the rotor center are revealed in the far wake regions. In the vertical direction, the deviation is related to vertical wind shear and ground effect, while in the lateral direction, the deviation is mainly caused by wind veering and wake rotation.

Constrained by the vertical wind shear in the ABL and by the ground surface, the wake expansion is faster in the lateral direction than in the vertical direction under all stability conditions, represented by the larger values of  $\sigma_y$  than  $\sigma_z$  in Fig. 4.9 (c). Due to the strong turbulent mixing, both  $\sigma_y$  and  $\sigma_z$  are amplified in the unstable ABL than in the neutral ABL. In the stable ABL, however, the expansion is strongest in the lateral direction but smallest in the vertical direction (“squished shape”), corresponding to the strongest effects of vertical wind shear and lateral wind veering. As shown in Fig. 4.9 (d), skewness of the wake from the Gaussian shape is most drastic in the stable ABL, especially in the lateral direction, consistent with Fig. 4.8. The unstable ABL induces relatively strong skewness in the vertical direction due to its quick contact with the ground surface. The skewness in the neutral ABL is almost negligible.

Next, turbulence properties of the wind turbine wake and their correlations to the stability conditions are discussed. In Figs. 4.10 and 4.11, the resolved added turbulence kinetic energy (TKE) and total kinematic shear stress  $-\overline{u'w'}$  are plotted at several downstream  $y-z$  planes. The resolved added TKE (will be referred to as added TKE hereafter for simplicity) is defined as the difference between the resolved TKE in the domain and that from the inflow. In general, the added TKE is more concentrated

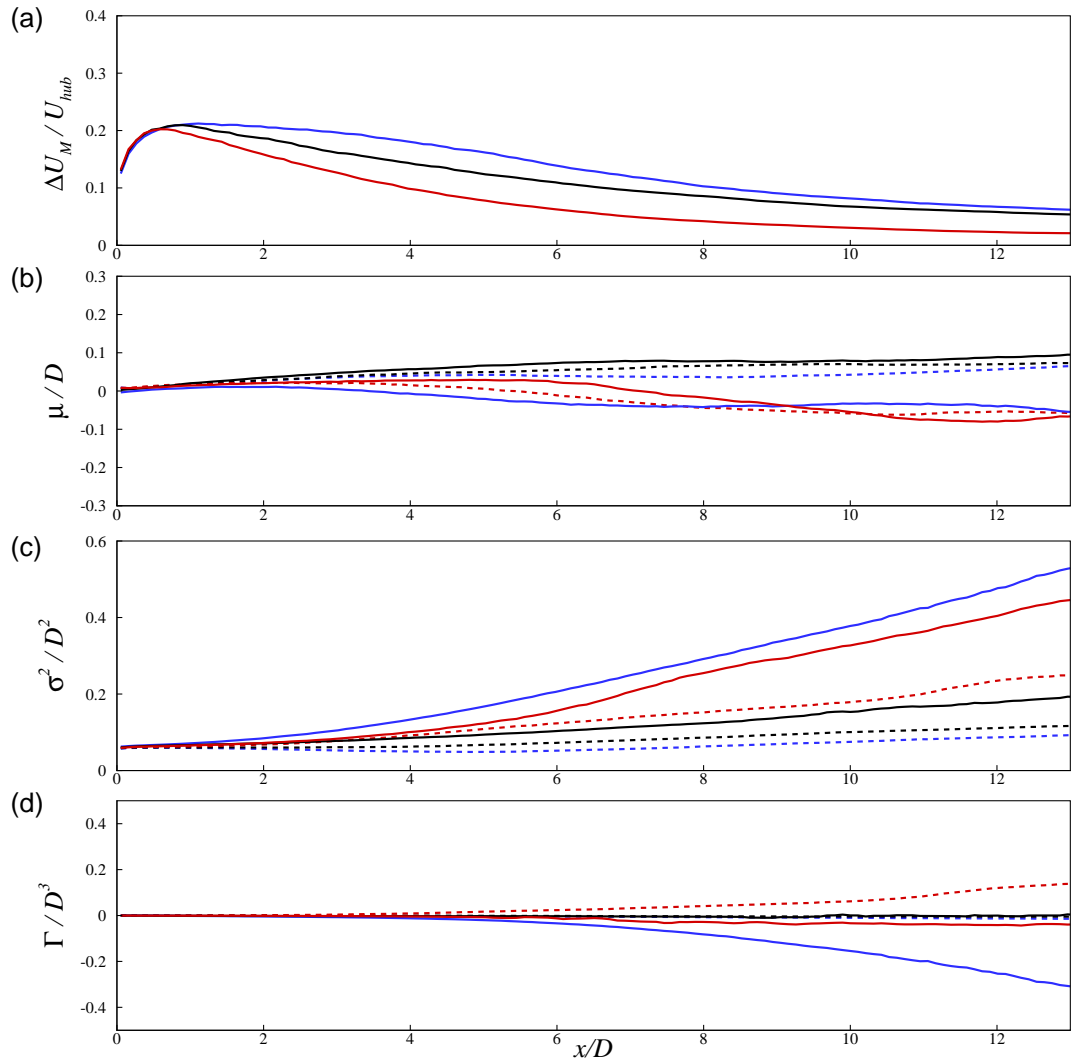


**Figure 4.9:** Statistics of single turbine wakes under stable (blue), neutral (black), and unstable (red) conditions, for: (a) mean streamwise velocity deficit  $\Delta \bar{u}_M$  normalized by  $U_{hub}$ ; (b) mean coordinates of the wake normalized by  $D$ ; (c) variances normalized by  $D^2$ ; and (d) skewness normalized by  $D^3$ . From (b) to (d), the solid lines are variables in the lateral direction and dashed lines are in the vertical direction.

above the hub height level, while the shear stress has opposite signs above and below the hub height levels. Different complex 3D features according to stability conditions are revealed in both the distributions of the added TKE and shear stress.

Specifically, when the ABL is stable, the bulk of the enhanced added TKE in the wake rarely reaches the top-tip level, but strongly expands in the lateral direction. The peak added TKE (i.e., the maximum value in the whole domain) occurs around  $7D$ . A good correlation between the shear stress and the added TKE is observed, indicating that the shear production is dominant in the TKE budget; in the neutral ABL, the large added TKE in the wake occurs approximately at the upper edges of the rotor region. The peak added TKE, as well as the peak shear stress (i.e., the maximum value in magnitude), are located roughly around  $5D$ . The strong turbulence in the unstable ABL induces strongest dissipations of the added TKE and shear stress, which are discernibly convected in the vertical direction. The peak added TKE and peak shear stress are observed at locations close to the turbine (before  $3D$ ) among all stability conditions. In addition, the magnitude of the peak added TKE increases with the stability in the ABL.

Due to the various stability conditions, distinctive instantaneous vortical structures in the wind turbine wakes are revealed in terms of the  $Q$ -criterion [122] (Fig. 4.12), where a positive value of  $Q$ :

$$Q = \frac{1}{2} \left( |\Omega_{ij}|^2 - |S_{ij}|^2 \right) > 0, \quad (4.12)$$

indicates that the Euclidean norm of the vorticity tensor  $\Omega_{ij}$  dominates over that of the rate of strain  $S_{ij}$  [123]. The  $Q$  criterion is a Galilean invariant vortex definition, with the additional condition that the pressure is lower than the ambient value [124]. In the stable ABL, after some distance downstream where the helical tip vortices break down, a series of coherent hairpin-like structures are observed, approximately aligned along the streamwise direction, which produce important secondary turbulence in the wake contributing to the high TKE in the far wake regions. These coherent vortical structures are believed to be triggered by the Kelvin-Helmholtz (K-H) instability, similar to

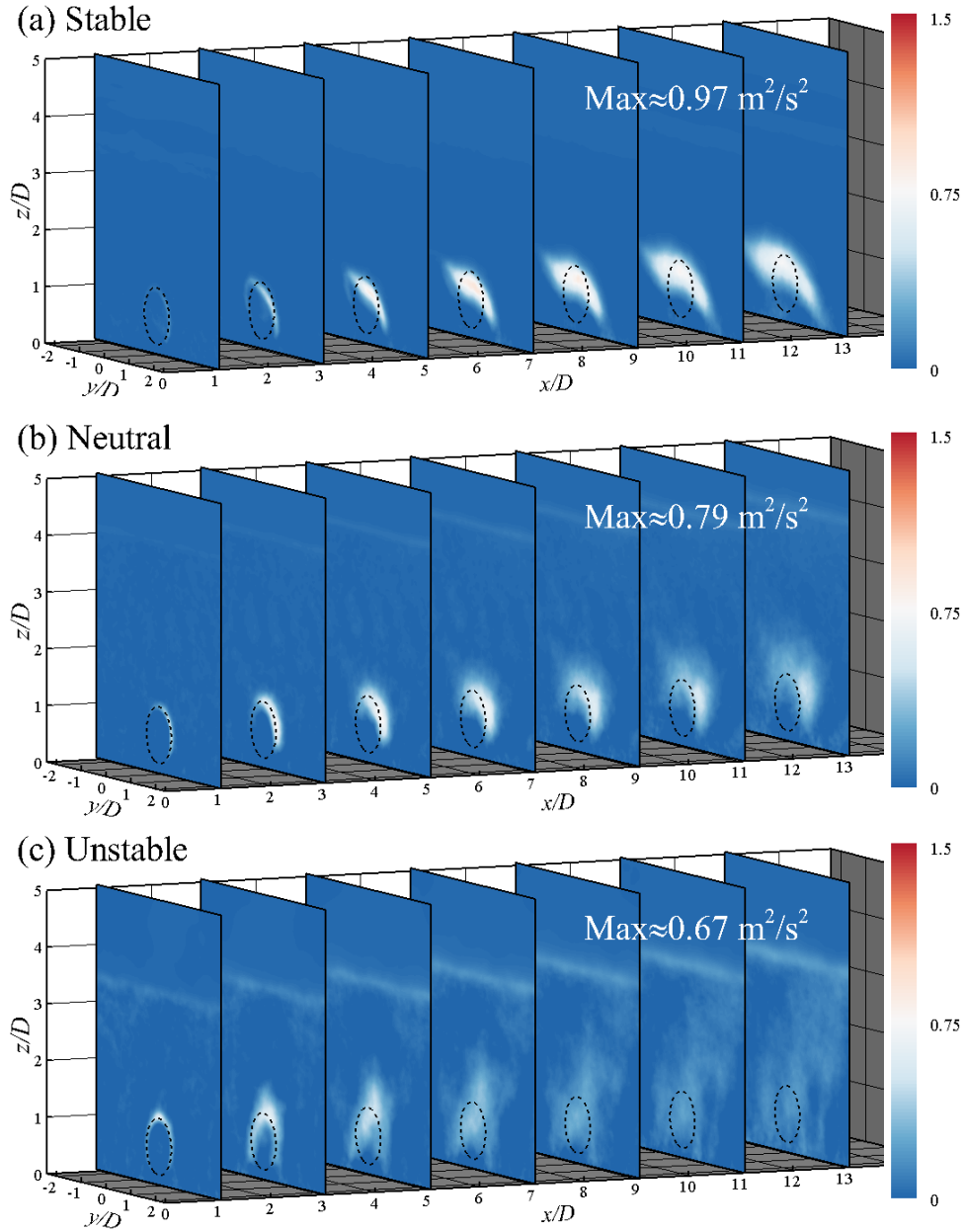


**Figure 4.10:** Time-averaged resolved added TKE [ $\text{m}^2/\text{s}^2$ ] in several downstream  $y-z$  planes of single turbine wakes under various stability conditions. The planes reside at  $x/D = 1, 3, 5, 7, 9, 11$  and  $13$ , respectively. The dashed circles show the rotor area in each plane. The maximum value of resolved added TKE over the whole domain is also shown in each case.

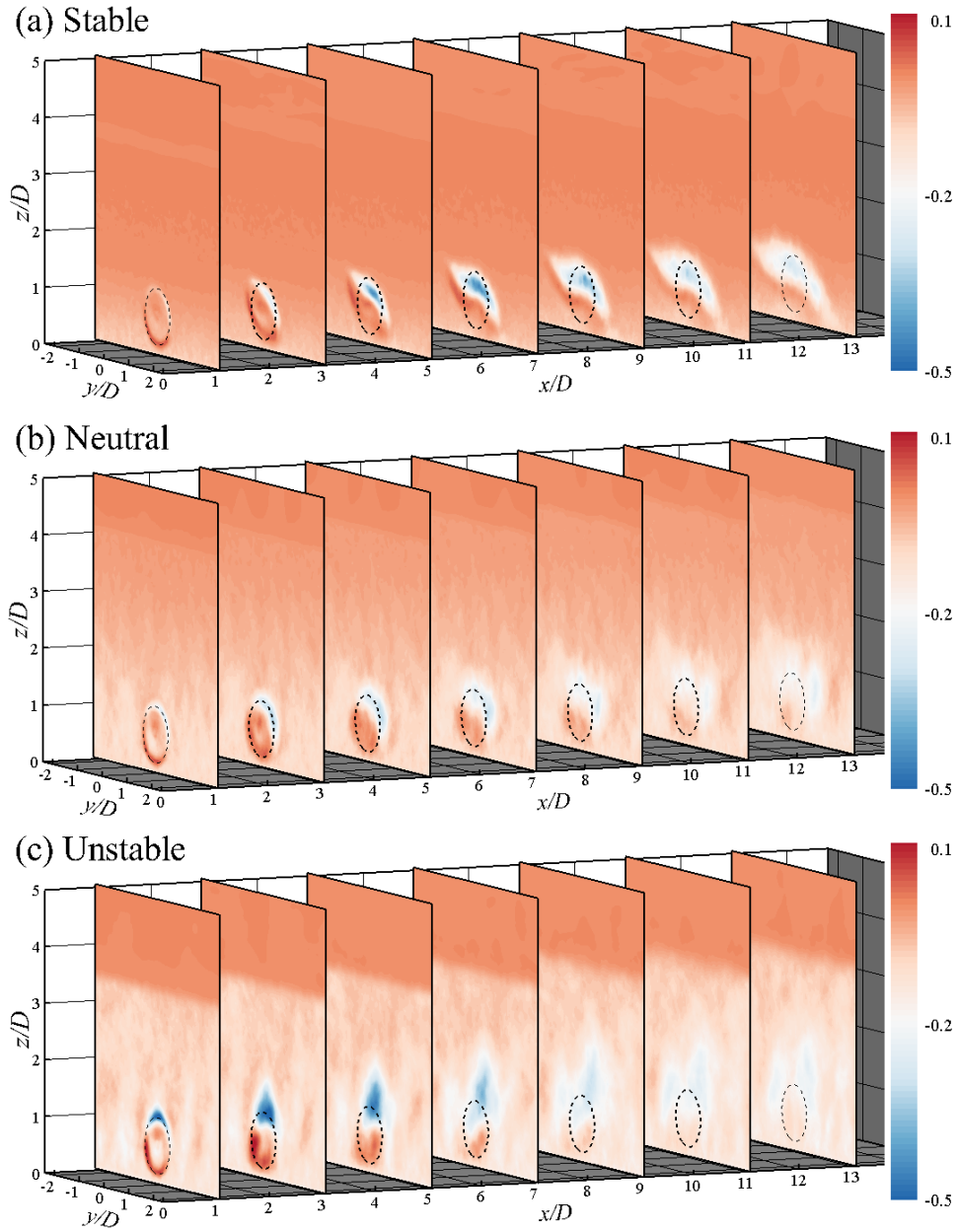


**Figure 4.11:** Time-averaged total kinematic shear stress  $-\overline{u'w'}$  [ $m^2/s^2$ ] in several downstream  $y - z$  planes of single turbine wakes under various stability conditions. The planes reside at  $x/D = 1, 3, 5, 7, 9, 11$  and  $13$ , respectively. The dashed circles show the rotor area in each plane.

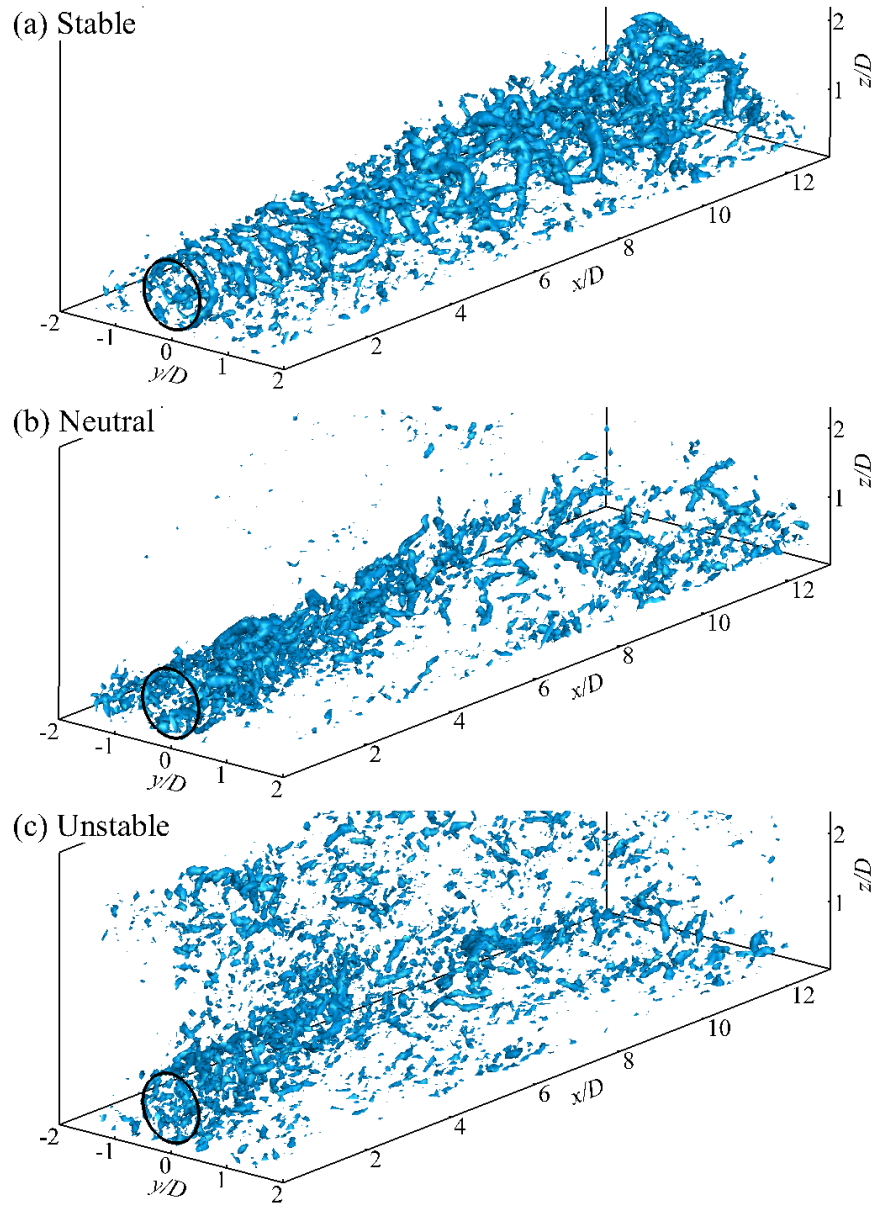


**Figure 4.12:** Instantaneous vortical structures for single turbine wakes under various stability conditions. The iso surfaces are  $Q = 0.01 \text{ s}^{-2}$ . The rotor of turbine is represented by the black solid circle, and only a portion of the computational domain is shown.

those observed in the high-Reynolds-number, stably stratified, turbulent wakes after a towed bluff body [125]. In the neutral and unstable ABLs, those coherent vortical structures are absent and structures with finer scales dominate. In the neutral ABL, the structures are more concentrated near the wake regions, whereas they are more spread out in the whole domain by strong convection motions in the unstable ABL.

The corresponding instantaneous vertical velocity component  $w$  are plotted in the horizontal plane at hub height in Fig. 4.13 at the same time instants shown in Fig. 4.12. In the stable ABL, different features are observed in the near/intermediate wake and far wake regions, i.e., the opposite directions of  $w$  occur on the two sides of the center line representing the rotation of the wake up to about  $6D$ , after which the alternating directions of  $w$  become aligned in the streamwise direction, as manifested by the roll-up vortices generated and evolving due to the K-H instability. In contrast, the variability of the wakes in the lateral direction (wake meandering) is more apparent in the neutral and unstable ABLs, where large-scale turbulent motions are formed.

The potential temperature distributions due to wind turbine wakes are presented in Fig. 4.14 under stable and unstable conditions. In terms of the time-averaged potential temperature deficit  $\Delta\bar{\theta} = \bar{\theta} - \bar{\theta}_{in}$  (where the script *in* denotes the values in the inflow  $y - z$  plane), clear spatial variations at  $O(10^{-1})$  K are observed in the wake in the stable ABL, correlated to the mean flow structures. Caused by the counter clockwise (with respect to the streamwise direction) mean wake rotation and wind veering (please refer to Fig. 4.7), a warming forms on the side of the rotor region where the downward motion of mean flow brings warmer air down from above, while a cooling happens on the other side where the opposite advection occurs. Away from the rotor region, the temperature variation is reduced. Aloft, the air is slightly cooled, while near the ground surface the temperature can either increase or decrease depending on local flow patterns with strong interactions with the ground surface. On the other hand, as shown in Fig. 4.14 (b), the redistribution of temperature is much weaker (at about  $O(10^{-3})$  K to  $O(10^{-2})$  K) and more uniform in the unstable ABL, where both velocity and temperature are well mixed even without the presence of wind turbine.

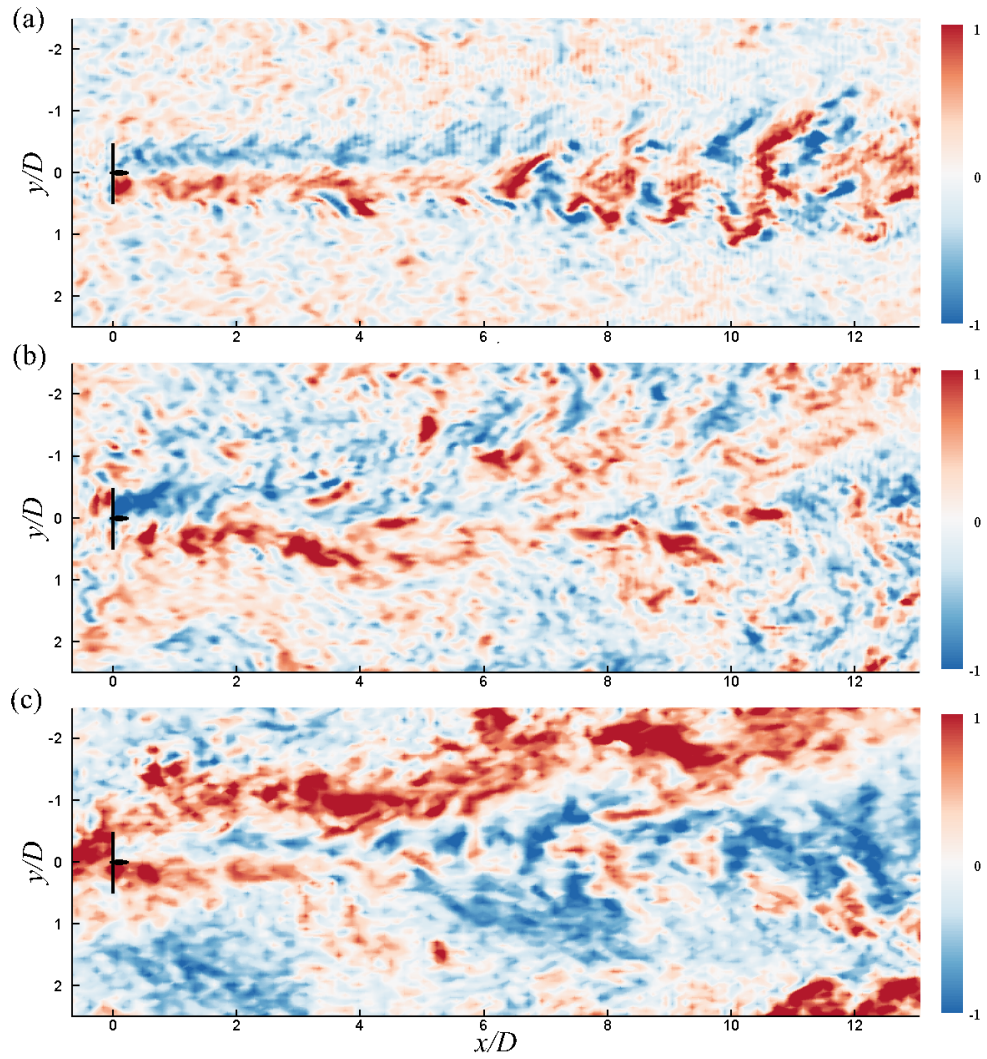


**Figure 4.13:** Contour plots of instantaneous vertical velocity component  $w$  [m/s] in the horizontal plane at the hub height for single turbine wakes under various stability conditions. The time instants are the same as plotted in Fig. 4.12.

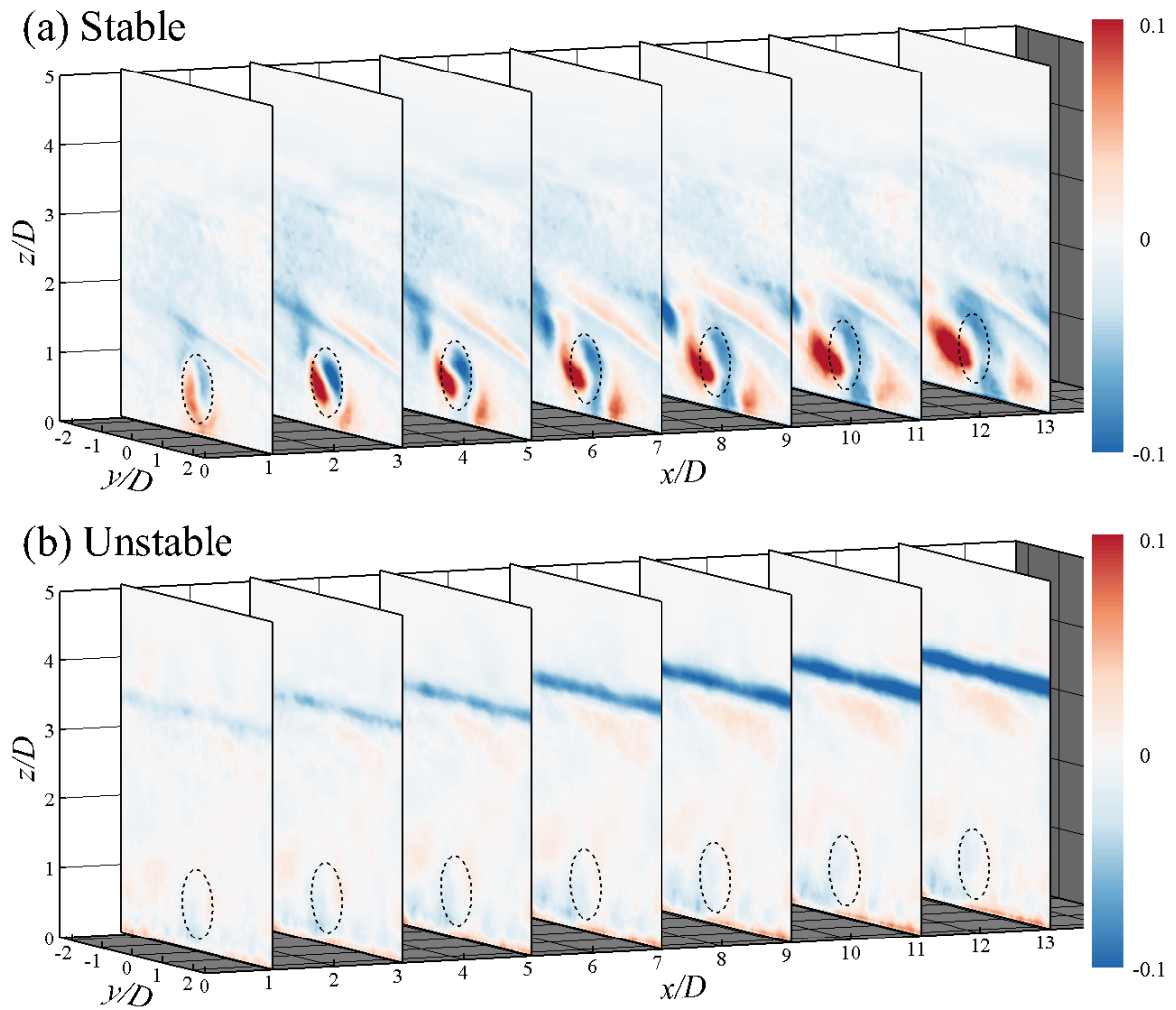


**Figure 4.14:** Time-averaged potential temperature deficit  $\Delta\bar{\theta}$  [K] in several downstream  $y - z$  planes of single turbine wakes under various stability conditions. The planes reside at  $x/D = 1, 3, 5, 7, 9, 11$  and  $13$ , respectively. The dashed circles show the rotor area in each plane.

Consistent with Lu and Porté-Agel [104], a relatively strong decrease of temperature occurs roughly at the height of ABL and a weak warming inside the ABL, especially near the ground surface, are observed as a result of downward heat flux from aloft to the lower regions. Note that a small cooling also occurs locally near the ground surface corresponding to the mean wake rotation.

#### 4.6.2 Wind farm simulations

In this section, we consider a wind farm of 5 turbines aligned in the rotated streamwise direction, in order to study the wake interactions under various stability conditions. The distance between two neighboring turbines is  $4D$ . The same computational domain and resolution are used as in the single turbine simulations, except that the streamwise length here is 2560 m with 384 grid points.

As discussed in Wu and Porté-Agel [97], the cumulative effect of multiple wakes under neutral conditions form a “wind-farm wake” with two regions: in the first region below the top-tip level (called the “core region” hereafter), a statistical equilibrium state is formed roughly after the third turbine; and a larger downwind variation is experienced due to expansion of the wakes in the second region above the turbines (called the “outer region” hereafter).

In general, those two regions are also observed here, as shown in Fig. 4.15, where the contours of time-averaged velocity deficit are presented. In the stable ABL, the vertical expansion of the wake is severely restricted, to the point that the height of the upper edge becomes almost constant for the last three turbines and the lower edge barely contacts with the ground. In the neutral ABL, the upper edge of the wake grows in an almost linear way and most of the wake comes in contact with the ground, and an equilibrium is reached in the core region roughly from the fourth turbine. In the unstable ABL, unlike the single turbine case (Fig. 4.6), the wake height continuously increases (except some local reductions at the rotors) but with a reduced rate once the equilibrium state is reached, roughly at the fourth turbine. The local reduction is

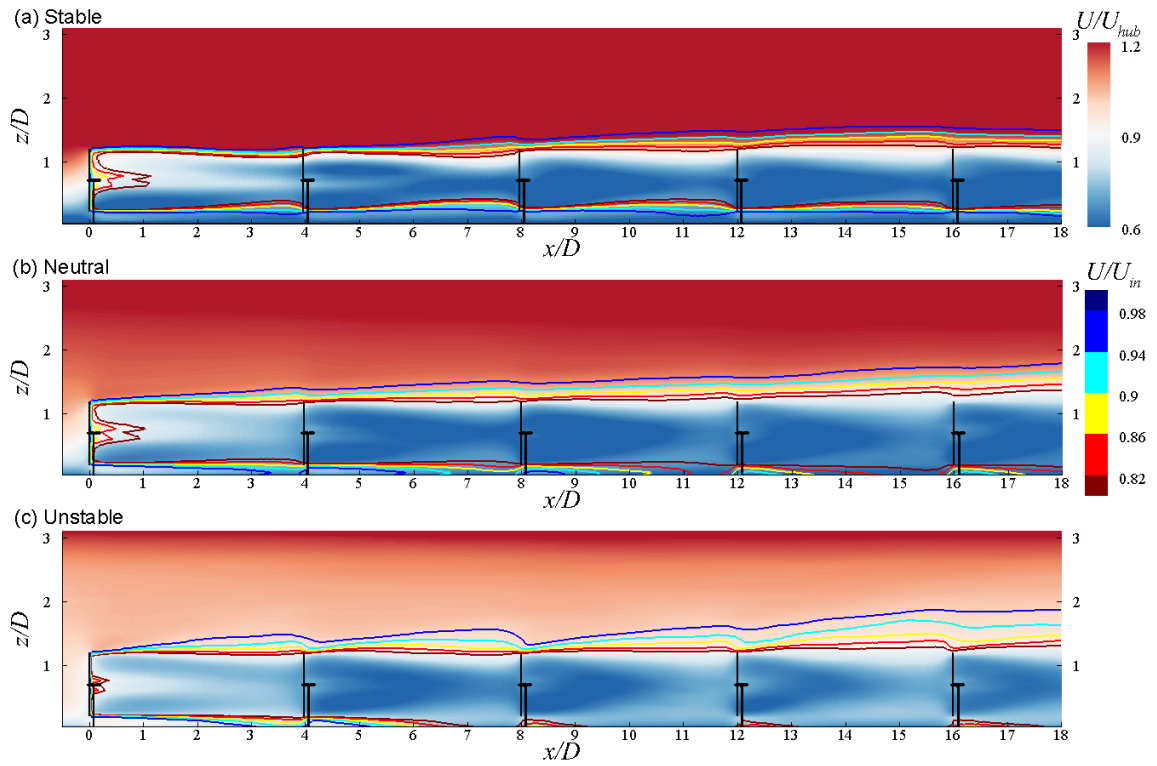


**Figure 4.15:** Contours of non-dimensional time-averaged streamwise velocity component  $U/U_{hub}$  in the vertical central plane for a wind farm under various stability conditions. The colored lines represent the streamwise velocity relative to  $U_{in}$ , the time-averaged upstream values at the corresponding heights.

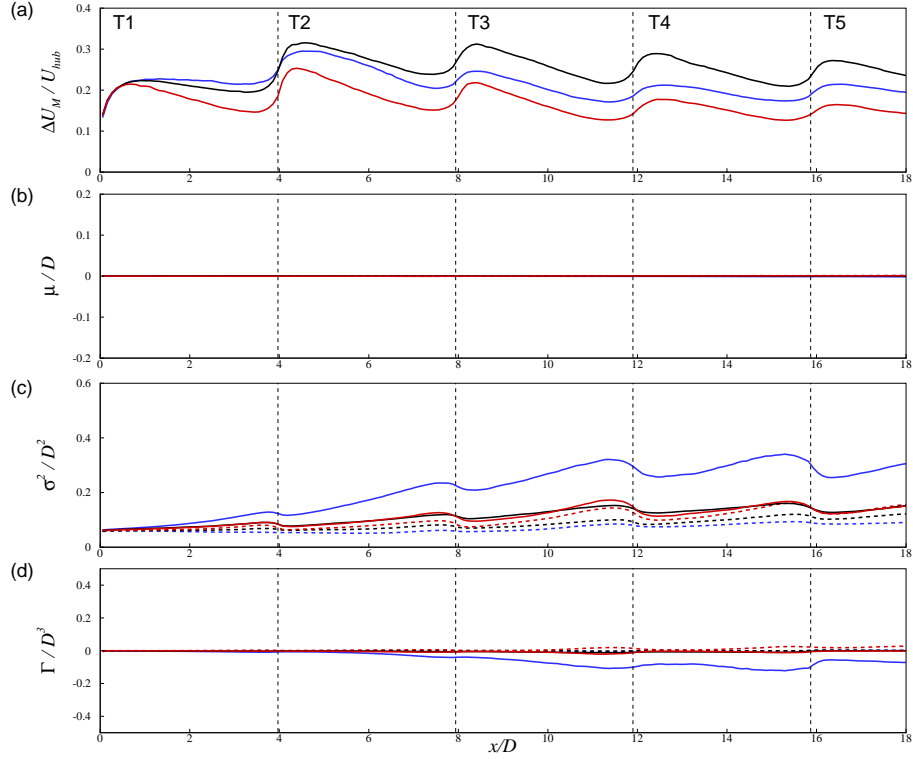


**Figure 4.16:** Statistics of wind farm wakes under stable (blue), neutral (black), and unstable (red) conditions, for: (a) mean streamwise velocity deficit  $\Delta \bar{u}_M$  normalized by  $U_{hub}$ ; (b) mean coordinates of the wake normalized by  $D$ ; (c) variances normalized by  $D^2$ ; and (d) skewness normalized by  $D^3$ . From (b) to (d), the solid lines are variables in the lateral direction and dashed lines are in the vertical direction. The thin black dashes lines represent the locations of the turbines (i.e., T2 to T5, and T1 is at  $x/D = 0.0$ ).

attributed to the local acceleration of the wind speed at the rotor tips due to a sudden velocity decrease (hence lower pressure) in the following wake.

The statistics of the mean streamwise velocity deficit in the wind farm wakes are calculated (see Eqns. 4.8 to 4.11) and plotted in Fig. 4.16. Compared to the single turbine wakes, there are several points worth mentioning here. First, as shown in Fig. 4.16 (a), the normalized mean velocity deficits are largest after the second turbine for all stability conditions, but an equilibrium is reached further downstream. Second, the mean velocity deficit after the second turbine is higher in the neutral ABL

than in the stable ABL, which is the contrary of the single turbine case, while the unstable condition still has the lowest deficit. Third, Fig. 4.16 (b) shows that the deficit centers in the wind farm wakes well collapse to the centerline of rotors, i.e., the deviations are almost negligible. Fourth, as shown in Fig. 4.9 (c) and (d), both the variances and skewness are much smaller in the wind farm cases than in their single turbine counterparts under all stability conditions, implying narrower wake expansions as well as less (but still discernible) deformations, especially in the stable ABL. The reductions can be attributed to two reasons: immature wake developments (i.e., the wakes in the wind farm have much less time and distance to develop between two streamwisely aligned turbines) and strongly enhanced turbulence mixing.

Compared to the single turbine case, the enhanced wind shear and the stronger velocity deficit produce much larger turbulence in the wind farm wakes regardless of the stability condition, as shown in terms of added TKE in Fig. 4.17. The added TKE in the wind farm wakes is strongest in the stable ABL and weakest in the unstable ABL. In addition, the peak added TKE occurs much later compared to the single turbine wakes, as a result of sequentially added turbulence production from each turbine in the array until the gradual reach of the equilibrium state further downstream. Also due to the equilibrium state, the values of the peak added TKE in the wind farm cases are nonlinearly increased by a factor of around 2.5 from the single turbine cases (not by a factor of 5 as one would expect from 5 turbines versus 1). Moreover, in all stability conditions, the distributions of added TKE are less spread out but more confined at the upper edge of the rotor region, although the deformation due to wind veering is still noticeable.

The instantaneous vortical structures at some selected time instants in the wind farm cases are shown in Fig. 4.18. Due to enhanced turbulence, a great amount of vortical structures with a wide range of scales are generated in the wind farm wakes under all stability conditions. Compared with the single turbine case, in the stable ABL, the coherent hairpin-line vortices are more revealed between the second and the fourth turbine, but gradually break up after that due to interactions with small-scale

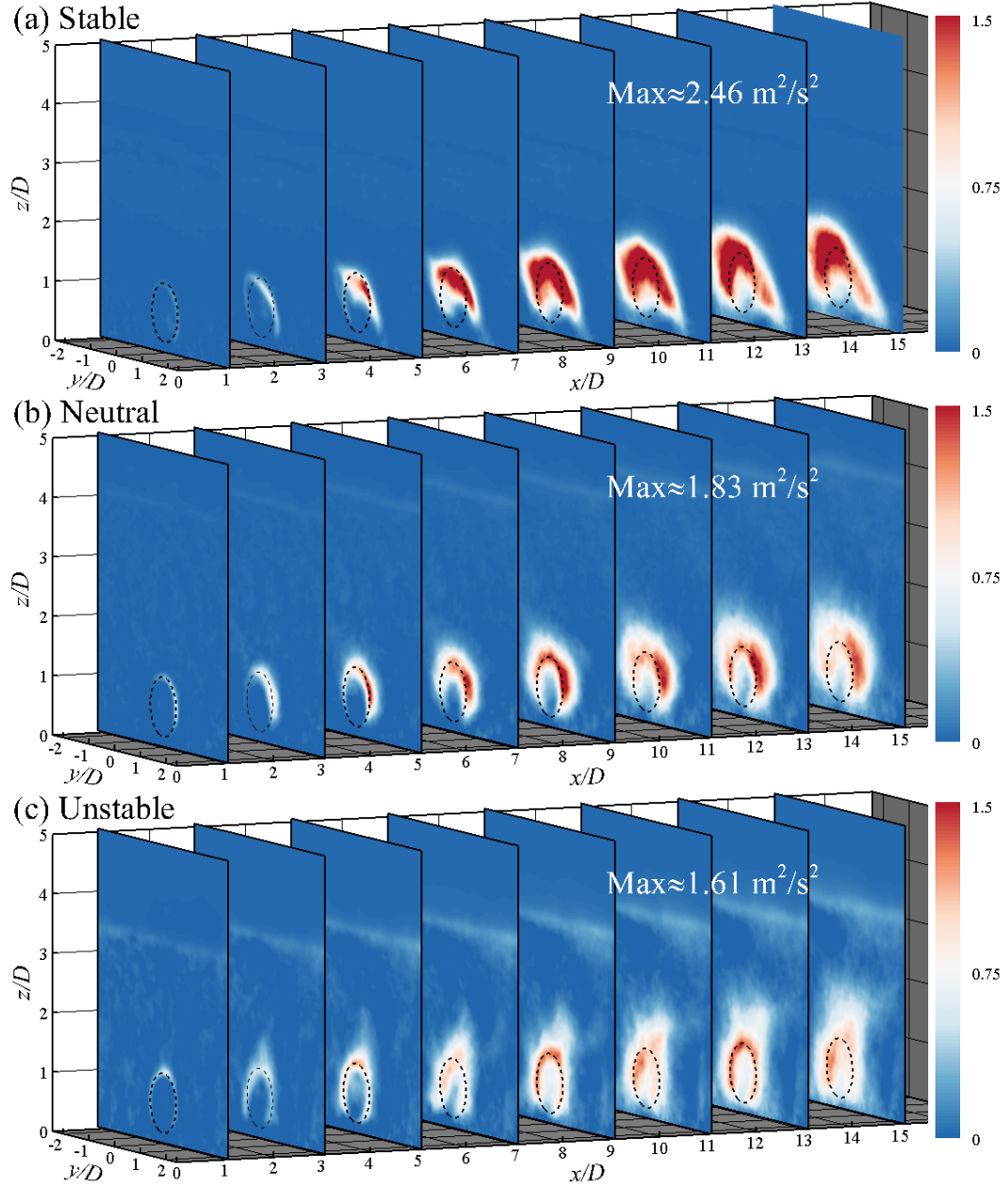


**Figure 4.17:** Time-averaged added TKE [ $\text{m}^2/\text{s}^2$ ] in several downstream  $y - z$  planes of wind farm wakes under various stability conditions. The planes reside at  $x/D = 1, 4, 7, 10, 13$  and  $16$ , respectively. The dashed circles show the rotor area in each plane. The maximum value of resolved added TKE over the whole domain is also shown in each case.

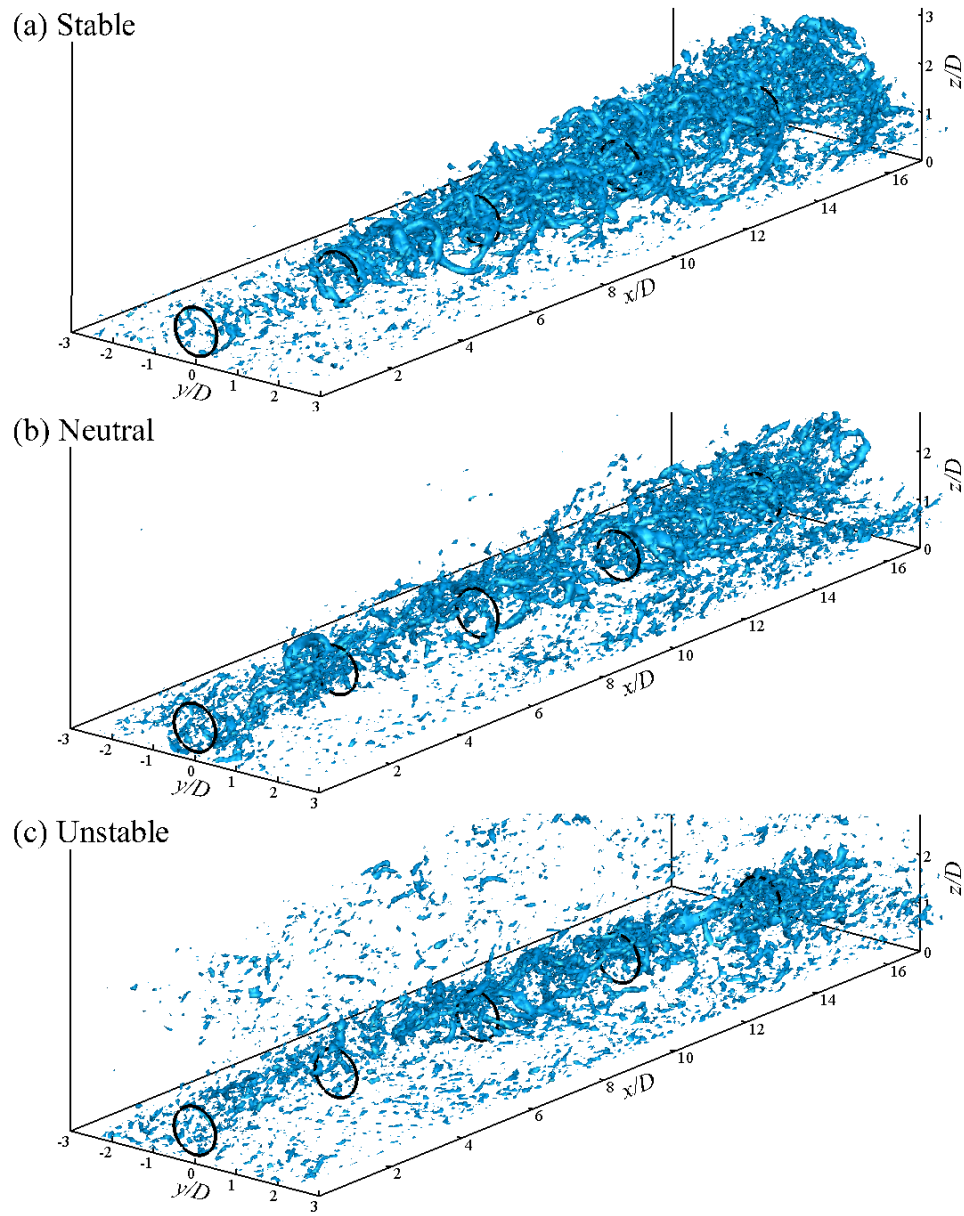


**Figure 4.18:** Instantaneous vortical structures for a wind farm wake under various stability conditions. The time instants are the same as shown in Fig. 4.12 and the iso surfaces  $Q = 0.015 \text{ s}^{-2}$  are plotted.

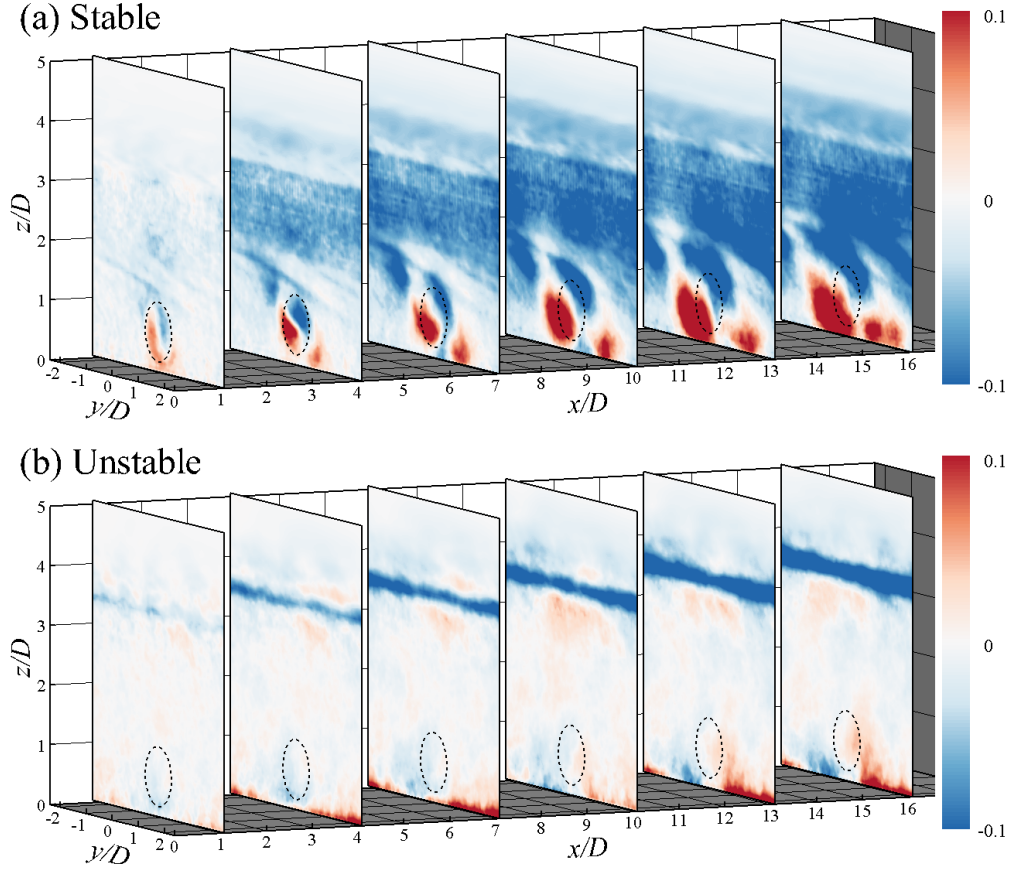


**Figure 4.19:** Time-averaged potential temperature change  $\Delta\theta$  [K] in several downstream  $y - z$  planes of wind farm wakes under various stability conditions. The planes reside at  $x/D = 1, 4, 7, 10, 13$  and  $16$ , respectively. The dashed circles show the rotor area in each plane.

vortical filaments. For the neutral and unstable conditions, some large vortical filaments are also formed possibly by two mechanisms: the merging of small-scale vortices and the breakup of the hairpin-like structures due to strong turbulent stretching and mixing [126].

Compared to the single turbine case, the patterns of temperature redistribution are almost maintained but their magnitudes are considerably augmented in the wind farm case, as shown in Fig. 4.19. Just like the mean flow, the temperature distribution also reveals an equilibrium behavior at the last two turbines. With the presence of the

wind farm, in the stable ABL, the air above the hub height level is cooled and the air below is warmed, with some local variations. In the unstable ABL, the temperature variations near the ground surface are more revealed as a result of enhanced mean flow motions.

Finally, it is important to investigate how the power generation of the wind farm is affected by the various stability conditions. Here, the extracted power by each turbine is simply estimated by

$$P = U_r \times T, \quad (4.13)$$

where  $U_r$  is the resolved streamwise velocity averaged over the rotor disk of each turbine, and  $T$  is the total thrust force obtained by the actuator-line model (including the nacelle, although its effect is very small). There are two factors that are strongly linked to mean wind power extraction: mean upstream wind speed at the rotor region and ambient turbulence level in the ABL. Higher mean upstream wind speed means higher available wind energy density, while higher turbulence levels reduce wake losses in the wind farm. However, it is hard to have those two factors to be favorable simultaneously in a real wind farm. Note that, with fixed geostrophic forcing, the mean wind speed at the hub height increases with the stability in the ABL, whereas the turbulence level changes in the opposite direction. The trade-off between those two factors arise from the subtle relationship between the atmospheric stability and wind power extraction.

In Fig. 4.20, both time-averaged absolute and relative powers extracted by the wind farm are plotted, where the relative power is with respect to the first turbine. It is clear that the absolute power extracted by the first turbine of the wind farm is well correlated to the mean wind speed variation due to stability (Fig. 4.20 (a)), i.e. largest in the stable and smallest in the unstable. The power drop from the first turbine to the second is drastic but the change becomes relatively small in the rest of the wind farm [4] as a result of the approaching of the equilibrium state in the core regions. With remarkably higher upstream wind speed in the stable ABL (the hub height wind speed is about 8% and 12% higher than those in the neutral and unstable ABLs, respectively), largest overall absolute power is extracted (about 34%

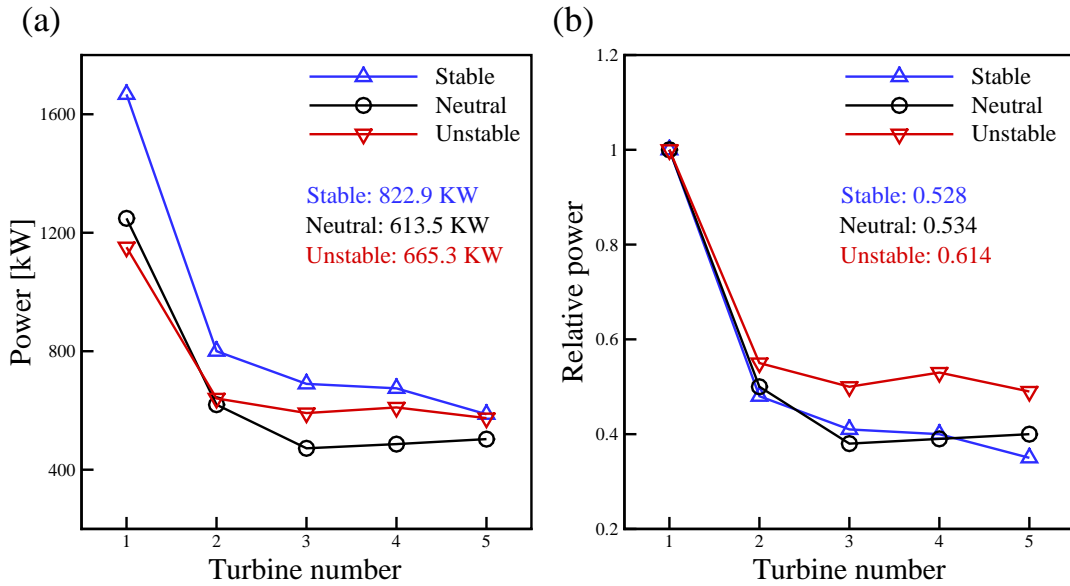


**Figure 4.20:** Time-averaged relative power extractions of the wind farm under various stability conditions: (a) absolute power and (b) relative power with respect to the first turbine.

and 24% higher than in the neutral and unstable ABLs, respectively). Although the mean upstream wind speed is slightly higher in the neutral ABL than in the unstable, the overall absolute power extraction is lower as a result of slower wake recovery in the neutral ABL with weaker atmospheric turbulence. In fact, the overall relative power extraction (Fig. 4.20 (b)) is highest in the unstable ABL and lowest in the stable ABL, which highlights the influence of wake recovery, and shows a good correlation with the corresponding turbulence levels in the ABL.

## 4.7 Conclusions

Clear correlations between the properties of turbine wakes and the atmospheric stability conditions are revealed by large-eddy simulations. Both a single turbine wake and wind farm wakes are studied. For the single turbine wake, the stability-related turbulence and vertical wind shear in the ABL significantly contribute to the wake growth and its recovery. Coupled with the wind veering due to Coriolis forcing and

the wake rotation due to turbine motion, the wake shape can be remarkably deformed during its propagation, especially in the stable ABL. As a result, the commonly-used hypothesis of Gaussian-type self similarity is violated. In addition, wave-like oscillations and coherent vortical structures are observed in the far-wake regions in the stable ABL. Clear spatial variations of temperature are observed in the stable ABL due to the wake effects, which are correlated to the mean flow patterns, whereas the influence on temperature is much weaker in the unstable ABL.

Compared to the single turbine wake, the velocity deficits and turbulence are much larger in the wind farm wakes. On the other hand, the deformations and asymmetries are not as strong in the wind farm wakes, due to less development and stronger turbulence mixing. Corresponding to the wave-like oscillation of the wakes in the stable condition, a peak at relatively low frequency is observed in the wind power spectrum. The mean power extraction of the wind farm is also strongly stability dependent. It is hard to conclude which stability condition is most favorable for the power extraction, because it is strongly dependent on the subtle trade off between mean upstream wind speed and ambient turbulence level under various stability conditions. This suggests that the energy efficiency of a wind farm can be improved by increasing turbulence while keeping a high hub-height wind speed (for instance, add obstacles or vertical axis wind turbines on the ground), especially when the ABL is stable or neutral.

Several limits of the current work are worth mentioning here, which will be considered in future studies. First, although clear trends are revealed, only a few stability conditions and a constant Coriolis frequency are considered, which are not enough to perform comprehensive quantifications. Second, constant surface temperature or heat flux conditions are prescribed here, which may not be realistic since they can vary in wakes, as shown in [36, 104]. Third, some of our preliminary results (not shown here) indicate that the rotational direction of the turbine may play an important role in the wake properties by interacting with the wind veering (especially in the stable ABL where the wind veering is most significant), which will be further studied. Moreover, instead of focusing on the quasi-steady state of the ABL, the diurnal as well as spatial

variations will be studied in future. Last but not least, more wind directions and wind farm layouts will be investigated, which are known to affect power generation. Nevertheless, the current study suggests that the wake properties, hence the wind farm performance, are a very complex but delicate topic, which can vary significantly from morning to evening, from summer to winter, from Netherland to India, or from the northern to the southern hemisphere. One has to be cautious to use some universal models or hypothesis to study this problem.

## Chapter 5

### CONCLUSIONS

In this dissertation, a finite-difference LES code is developed to study the interactions between wind turbine wakes and the atmospheric boundary layer. From the LES results, it was found that the growth of a wind turbine wake is not isotropic but constrained in the vertical direction by the underlying mean wind shear and by the ground. Moreover, influenced by atmospheric stability and Coriolis effect, complex 3d flow structures with substantial stretching and skewing are generated in the wind turbine wakes, challenging the commonly used assumption of Gaussian-type self-similarity.

The atmospheric stability plays an important role in estimations of wind energy generation. On one hand, the available wind speed varies with stability, i.e., the wind speed is higher at the rotor region when the ABL is stable (for a fixed geostrophic wind and surface roughness). On the other hand, the wake recovery varies with stability, i.e., wakes recover faster (thus the wake losses are minimized) when the ABL is unstable due to its strong turbulence mixing. As a competition of those two factors, it is not possible to conclude which stability condition is favored from the perspective of energy output in a wind farm.

Wind turbine wakes alter the temperature distribution in downstream, mainly by mean flow advection rather than by turbulence mixing. The variation in temperature is more noticeable in the stable ABL, where the wake rotation advects the highly sheared temperature profile. In the unstable ABL, the spatial variation of temperature due to wind turbine wakes is much weaker. Near the ground surface, an overall tendency of warming is observed in both stability conditions, but cooling can also happen locally depending on the specific flow patterns.

The observations made here provide new insights on wind turbine wakes and their interactions with the ABL, which can be used in developing wake models, optimizing wind farm layouts, reducing fatigue load and power fluctuation, and understanding potential environmental impacts. Since the ABL is a complex system, which involves various mechanisms that may influence wind energy, the current study is still far from sufficient to provide a comprehensive understanding. Considering the fast growth of wind energy globally, this study represents an additional small step towards increasing the power efficiency while reducing its cost, financially and environmentally, in order to make wind energy more competitive over traditional fossil fuels.

## BIBLIOGRAPHY

- [1] PP. Sullivan, CH. Moeng, B. Stevens, DH. Lenschow, and SD. Mayor. Structure of the entrainment zone capping the convective atmospheric boundary layer. *J. Atmos. Sci.*, **55**:3042–3064, 1998.
- [2] Global wind report: Annual market update 2014. Global Wind Energy Council, 2015.
- [3] RJ. Barthelmie, G. Larsen, S. Pryor, H. Jørgensen, H. Bergström, W. Schlez, K. Rados, B. Lange, P. Vølund, S. Neckelmann, S. Mogensen, G. Schepers, T. Hegberg, L. Folkerts, and M. Magnusson. Endow (efficient development of offshore wind farms): modelling wake and boundary layer interactions. *Wind Energy*, **7**:225–245, 2004.
- [4] RJ. Barthelmie, SC. Pryor, ST. Frandsen, KS. Hansen, JG. Schepers, K. Rados, W. Schlez, A. Neubert, LE. Jensen, and S. Neckelmann. Quantifying the Impact of Wind Turbine Wakes on Power Output at Offshore Wind Farms. *J. Atmos. Oceanic Technol.*, **27**:1302–1317, 2010.
- [5] RJ. Barthelmie and LE. Jensen. Evaluation of wind farm efficiency and wind turbine wakes at the nysted offshore wind farm. *Wind Energy*, **13**:573–586, 2010.
- [6] CL. Archer, S. Mirzaeisefat, and S. Lee. Quantifying the sensitivity of wind farm performance to array layout options using large-eddy simulation. *Geophys. Res. Lett.*, **40**:4963–4970, 2013.
- [7] MJ. Churchfield, S. Lee, J. Michalakes, and PJ. Moriarty. A numerical study of the effects of atmospheric and wake turbulence on wind turbine dynamics. *J. Turbulence*, **13**:N14, 2012.

- [8] MJ. Churchfield, S. Lee, PJ. Moriarty, LA. Martínez, S. Leonardi, G. Vijayakumar, and JG. Brasseur. A large-eddy simulation of wind-plant aerodynamics. 50th AIAA Aerospace Sciences Meeting including the New Horizons Forum and Aerospace Exposition; *Nashville, Tennessee*, 09-12 January 2012.
- [9] MRV. Sta. Maria and MZ. Jacobson. Investigating the Effect of Large Wind Farms on Energy in the Atmosphere. *Energies*, **2**:816–838, 2009.
- [10] DB. Barrie and DB. Kirk-Davidoff. Weather response to a large wind turbine array. *Atmos. Chem. Phys.*, **10**:769–775, 2010.
- [11] C. Wang and RG. Prinn. Potential climatic impacts and reliability of very large-scale wind farms. *Atmos. Chem. Phys.*, **10**:2053–2061, 2010.
- [12] SB. Roy and JJ. Traiteur. Impacts of wind farms on surface air temperatures. *Proc. Natl. Acad. Sci.*, **107**((42)):17899–17904, 2010.
- [13] SB. Roy. Simulating impacts of wind farms on local hydrometeorology. *J. Wind Eng. Ind. Aerodyn.*, **99**:491–498, 2011.
- [14] L. Zhou, Y. Tian, S. Baidya Roy, C. Thorncroft, and LF. Bosart. Impacts of wind farms on land surface temperature. *Nature Climate Change*, **2**:539–543, 2012.
- [15] AC. Fitch, JK. Lundquist, and JB Olson. Mesoscale influences of wind farms throughout a diurnal cycle. *Mon. Wea. Rev.*, **141**:2173–2198, 2013.
- [16] LJ. Vermeer, JN. Sørensen, and A. Crespo. Wind turbine wake aerodynamics. *Prog. Aerosp. Sci.*, **39**:467–510, 2003.
- [17] RB. Stull. *An introduction to boundary layer meteorology*. Kluwer Academic Publishers, Dordrecht, 1988.
- [18] S. Xie, N. Ghaisas, and CL. Archer. Sensitivity issues in finite-difference large-eddy simulations of the atmospheric boundary layer with dynamic subgrid-scale models. *Boundary-Layer Meteorol.*, **157**:421–445, 2015.

- [19] S. Xie and CL. Archer. Self-similarity and turbulence characteristics of wind turbine wakes via large-eddy simulation. *Wind Energy*, **18**:1815–1838, 2015.
- [20] JW. Deardorff. A numerical study of three-dimensional turbulence channel flow at large Reynolds numbers. *J. Fluid Mech.*, **41**:453–480, 1970.
- [21] C. Moeng. A large-eddy simulation model for the study of planetary boundary-layer turbulence. *J. Atmos. Sci.*, **46**:2311–2330, 1984.
- [22] J. Smagorinsky. General circulation experiments with the primitive equations: I. the basic experiment. *Mon. Weather Rev.*, **91**((3)):99–164, 1963.
- [23] M. Germano, U. Piomelli, and WH. Cabot. A dynamic subgrid-scale eddy viscosity model. *Phys. Fluids A*, **3**:1760–1765, 1991.
- [24] DK. Lilly. A proposed modification of the germano subgrid-scale closure method. *Phys. Fluids A*, **4**:633–635, 1992.
- [25] KS. Yang and JH. Ferziger. Large-eddy simulation of turbulent obstacle flow using a dynamic subgrid-scale mode. *AIAA Journal*, **31**(8):1406–1413, 1993.
- [26] U. Piomelli. High Reynolds number calculations using the dynamic subgrid scale stress model. *Phys. Fluids A*, **5**:1484–1490, 1993.
- [27] Y. Zang, RL. Street, and JR. Koseff. A dynamics mixed subgrid-scale model and its application to turbulent recirculating flows. *Phys. Fluids A*, **5**(12):3186–3196, 1993.
- [28] C. Meneveau, T. Lund, and W. Cabot. A lagrangian dynamic subgrid-scale model of turbulence. *J. Fluid Mech.*, **319**:353–385, 1996.
- [29] P. Sagaut. *Large eddy simulation for incompressible flows: an introduction (Third Edition)*. Springer, Heidelberg, Germany, 144–146 pp, 2006.

- [30] C. Meneveau and J. Katz. Scale-invariance and turbulence models for large-eddy simulation. *Annu. Rev. Fluid Mech.*, **32**:1–32, 2000.
- [31] F. Porté-Agel, C. Meneveau, and MB. Parlange. A scale-dependent dynamic model for large-eddy simulation: application to a neutral atmospheric boundary layer. *J. Fluid Mech.*, **415**:261–284, 2000.
- [32] E. Bou-Zeid, MB. Parlange, and C. Meneveau. A scale-dependent lagrangian dynamic model for large eddy simulation of complex turbulent flows. *Phys. Fluids*, **17**:025105, 2005.
- [33] E. Bou-Zeid, N. Vercauteren, MB. Parlange, and C. Meneveau. Scale dependence of subgrid-scale model coefficients: An a priori study. *Phys. Fluids*, **20**:115106, 2008.
- [34] M. Calaf, C. Meneveau, and J. Meyers. Large eddy simulation study of fully developed wind-turbine array boundary layers. *Phys. Fluids*, **22**:015110, 2010.
- [35] M. Calaf, MB. Parlange, and C. Meneveau. Large eddy simulation study of scalar transport in fully developed wind-turbine array boundary layers. *Phys. Fluids*, **23**:126603, 2011.
- [36] H. Lu and F. Porté-Agel. Large-eddy simulation of a very large wind farm in a stable atmospheric boundary layer. *Phys. Fluids*, **23**:065101, 2011.
- [37] YT. Wu and F. Porté-Agel. Large-eddy simulation of wind-turbine wakes: evaluation of turbine parametrisations. *Boundary-Layer Meteorol.*, **138**:345–366, 2011.
- [38] A. Sescu and C. Meneveau. A control algorithm for statistically stationary large-eddy simulations of thermally stratified boundary layers. *Q. J. R. Meteorol. Soc.*, **140**(683):2017—2022, 2014.

- [39] D. Yang, C. Meneveau, and L. Shen. Large-eddy simulation of offshore wind farm. *Phys. Fluids*, **26**(2):025101, 2014.
- [40] WC. Skamarock, JB. Klemp, J. Dudhia, DO. Gill, DM. Barker, MG. Duda, XY. Huang, W. Wang, and JG. Powers. A Description of the Advanced Research WRF Version 3. *NCAR, Boulder, CO.*, 2008.
- [41] M. Xue, KK. Droegemeier, and V. Wond. The Advanced Regional Prediction System (ARPS): A multi-scale nonhydrostatic atmospheric simulation and prediction model. Part I: Model dynamics and verification. *Meteorol. Atmos. Phys.*, **75**:161–193, 2000.
- [42] M. Xue, KK. Droegemeier, and V. Wond. The Advanced Regional Prediction System (ARPS): A multi-scale nonhydrostatic atmospheric simulation and prediction model. Part II: Model physics and applications. *Meteorol. Atmos. Phys.*, **76**:143–165, 2001.
- [43] DA. Shetty, TC. Fisher, AR. Chunekar, and SH. Frankel. High-order incompressible large-eddy simulation of fully inhomogeneous turbulent flows. *J. Comput. Phys.*, **229**:8802–8822, 2013.
- [44] PE. DesJardin and SH. Frankel. Large eddy simulation of a nonpremixed reacting jet: Application and assessment of subgrid-scale combustion models. *Phys. Fluids*, **10**:2298–2314, 1998.
- [45] FK. Chow and P. Moin. A further study of numerical errors in large-eddy simulations. *J. Comput. Phys.*, **184**:366—380, 2003.
- [46] Y. Morinishi, TS. Lund, OV. Vasilyev, and P. Moin. Fully conservative higher order finite difference schemes for incompressible flow. *J. Comput. Phys.*, **143**:90–124, 1998.

- [47] TS. Lund and HJ. Kaltenbach. Experiments with explicit filtering for LES using a finitedifference method. *Annunual Research Briefs, Center for Turbulence Research, Stanford University*, pages 91–105, 1995.
- [48] J. Gullbrand and FK. Chow. The effect of numerical errors and turbulence models in large-eddy simulations of channel flow, with and without explicit filtering. *J. Fluid Mech.*, **495**:323—341, 2003.
- [49] FK. Chow, RL. Street, M. Xue, and JH. Ferziger. Explicit Filtering and Reconstruction Turbulence Modeling for Large-Eddy Simulation of Neutral Boundary Layer Flow. *J. Atmos. Sci.*, **62**:2058—2077, 2005.
- [50] G. Kirkil, J. Mirocha, E. Bou-Zeid, FK. Chow, and Kosović. Implementation and evaluation of dynamic subfilter-scale stress models for large-eddy simulation using WRF. *Mon. Weather Rev.*, **140**:266–284, 2011.
- [51] E. Balaras, C. Benocci, and U. Piomelli. Finite-difference computations of high Reynolds number flows using the dynamic subgrid-scale model. *Theor. Comput. Fluid. Dyn.*, **7**:207–216, 1995.
- [52] FM. Najjar and DK. Tafti. Study of discrete test filters and finite difference approximations for the dynamic subgridscale stress model. *Phys. Fluids*, **8**:1076–1088, 1996.
- [53] DK. Lilly. The representation of small-scale turbulence in numerical simulation experiments. In *Proc. IBM Scientific Computing Symposium on Environmental Sciences*, page 195, 1967.
- [54] A. Scotti, C. Meneveau, and DK. Lilly. Generalized Smagorinsky model for anisotropic grids. *Phys. Fluids*, **5**:2306–2308, 1993.
- [55] FH. Harlow and JE. Welch. Numerical calculation of time-dependent viscous incompressible flow of fluid with free surface. *Phys. Fluids*, **8**:2182–2189, 1965.

- [56] T. Zang. On the rotation and skew-symmetric forms for incompressible flow simulations. *Appl. Numer. Math.*, **7**:27—40, 1991.
- [57] GA. Blaisdell, ET. Spyropoulos, and JH. Qin. The effect of the formulation of nonlinear terms on aliasing errors in spectral methods. *Appl. Numer. Math.*, **21**(3):207—219, 1996.
- [58] AG. Kravchenko and P. Moin. On the effect of numerical errors in large eddy simulations of turbulent flows. *J. Comput. Phys.*, **131**(2):310—322, 1997.
- [59] J. Kim and P. Moin. Application of a fractional-step method to incompressible navier-stokes equations. *J. Comput. Phys.*, **59**:308–323, 1985.
- [60] A. McAdams, E. Sifakis, and J. Teran. A parallel multigrid poisson solver for fluids simulation on large grids. *Proceedings of Eurographics/ ACM SIGGRAPH Symposium on Computer Animation*, pages 65–74, 2010.
- [61] JG. Brasseur and T. Wei. Designing large-eddy simulation of the turbulent boundary layer to capture law-of-the-wall scaling. *Phys. Fluids*, **22**:021303, 2010.
- [62] AE. Perry, S. Henbest, and MS. Chong. A theoretical and experimental study of wall turbulence. *J. Fluid Mech.*, **165**:163–199, 1986.
- [63] SA. Orszag. On the elimination of aliasing in finite-difference schemes by filtering high-wavenumber components. *J. Atmos. Sci.*, **28**:1074—1074, 1971.
- [64] G. De Stefano and OV. Vasilyev. Sharp cutoff versus smooth filtering in large eddy simulation. *Phys. Fluids*, **14**(1):362–369, 2002.
- [65] PJ. Mason. Large-eddy simulation of the convective atmospheric boundary layer. *J. Atmos. Sci.*, **46**:1492–1516, 1989.
- [66] N. Hutchins and I. Marusic. Evidence of very long meandering features in the logarithmic region of turbulent boundary layers. *J. Fluid Mech.*, **579**:1–28, 2007.

- [67] A. Smits, B. McKeon, and I. Marusic. High-reynolds number wall turbulence. *Annu. Rev. Fluid Mech.*, **43**:353–375, 2011.
- [68] Global wind statistics 2012. Global Wind Energy Council, 02 2013.
- [69] A. Crespo, J. Hernández, and S. Frandsen. Survey of modelling methods for wind turbine wakes and wind farms. *Wind Energy*, **2**:1–24, 1999.
- [70] A. Crespo and J. Hernández. Turbulence characteristics in wind-turbine wakes. *J. Wind Eng. Ind. Aerodyn.*, **61**:71–85, 1996.
- [71] PBS. Lissaman. Energy effectiveness of arbitrary arrays of wind turbines. *J. Energy*, **3**:323–328, 1979.
- [72] PEJ. Vermeulen. An experimental analysis of wind turbine wakes. Proceedings of the 3rd International Symposium on Wind Energy System, *Lyngby, Denmark*, pages 431–450, August 1980.
- [73] NO. Jensen. A note on wind turbine interaction. Technical Report Risø-M-2411, RisøNational Laboratory, Roskilde, Denmark, November 1983.
- [74] S. Frandsen, R. Barthelmie, S. Pryor, O. Rathmann, S. Larsen, J. Høstrup, and M. Thøgersen. Analytical modelling of wind speed deficit in large offshore wind farms. *Wind Energy*, **9**:39–53, 2006.
- [75] I. Katic. A simple model for cluster efficiency. Proceedings of the European wind energy association conference and exhibition; *Rome, Italy*, **75**:407–409, 1986.
- [76] N. Troldborg. Actuator line modeling of wind turbine wakes. PhD Thesis; *Technical University of Denmark.*, 2008.
- [77] PM. Sforza, P. Sheering, and M. Smorto. Three-dimensional wakes of simulated wind turbines. *AIAA Journal*, **19**:1101–1107, 1981.

- [78] JF. Ainslie. Calculating the field in the wake of wind turbines. *J. Wind Eng. Ind. Aerodyn.*, **27**:213–224, 1988.
- [79] JN. Sørensen and WZ. Shen. Numerical modeling of wind turbine wakes. *J. Fluid Mech.*, **124**:393–399, 2002.
- [80] JN. Sørensen, WZ. Shen, and X. Mundate. Analysis of wake states by a full-field actuator disc model. *Wind Energy*, **1**:73–88, 1998.
- [81] A. Jimenez, A. Crespo, E. Migoya, and J. Garcia. Advances in large-eddy simulation of a wind turbine wake. *Journal of Physics: Conference Series*, **75**:012041, 2007.
- [82] S. Ivanell, JN. Sørensen, R. Mikkelsen, and D. Henningson. Analysis of numerically generated wake structures. *Wind Energy*, **12**:63–80, 2009.
- [83] LP. Chamorro and F. Porté-Agel. Effects of thermal stability and incoming boundary-layer flow characteristics on wind-turbine wakes: a wind-tunnel study. *Boundary-Layer Meteorol.*, **136**:515–533, 2010.
- [84] N. Troldborg, JN. Sørensen, and R. Mikkelsen. Actuator line simulation of wake of wind turbine operating in turbulent inflow. *The Science of Making Torque from Wind*, *Journal of Physics: Conference Series*, **75**:012063, 2007.
- [85] A. Crespo, F. Manuel, D. Moreno, E. Fraga, and J. Hernández. Numerical analysis of wind turbine wakes. *Proceedings of the Delphi Workshop on Wind Energy Applications, Delphi, Greece*, pages 15–25, 1985.
- [86] J. Manwell, J. McGowan, and A. Rogers. *Wind energy explained: theory, design and application*, 577 pp. Wiley, New York, 2002.
- [87] R. Mikkelsen. Actuator disc methods applied to wind turbines. PhD Dissertation, *Technical University of Denmark*, 2003.

- [88] LA. Martinez, S. Leonardi, MJ. Churchfield, and PJ. Moriarty. A comparison of actuator disk and actuator line wind turbine models and best practices for their use. 50th AIAA Aerospace Sciences Meeting including the New Horizons Forum and Aerospace Exposition; *Nashville, Tennessee*, pages 09–12, January 2012.
- [89] MJ. Churchfield and S. Lee. Sowfa: High-fidelity analysis of fluid physics and structural response using large-eddy simulations and fast. <http://wind.nrel.gov/designcodes/simulators/SOWFA/>.
- [90] H. Tennekes and JL. Lumley. *A First Course in Turbulence*. The MIT Press, Cambridge, MA, 1972.
- [91] SB. Pope. *Turbulent Flows*. Cambridge University Press, Cambridge, UK, 2000.
- [92] M. Bastankhah and F. Porté-Agel. A new analytical model for wind-turbine wakes. *Renewable Energy*, **70**:1160123, 2014.
- [93] YT. Wu and F. Porté-Agel. Atmospheric turbulence effects on wind-turbine wakes: an les study. *Energies*, **5**:5340–5362, 2012.
- [94] DC. Quarton. Wake turbulence characterization. Final Report from Garrad Hassan and Partners to the Energy Technology Support Unit of the Department of Energy of the UK, Contract No. ETSUWN 5096, 1989.
- [95] Hassan U. A wind tunnel investigation of the wake structure within small wind turbine farms. *E/5A/CON/5113/1890*. UK Department of Energy, ETSU, 1992.
- [96] H. Hu, Z. Yang, and P. Sarkar. Dynamic wind loads and wake characteristics of a wind turbine model in an atmospheric boundary layer wind. *Exp. Fluids*, **52**:1277–1294, 2012.
- [97] YT. Wu and F. Porté-Agel. Simulation of turbulent flow inside and above wind farms: model validation and layout effects. *Boundary-Layer Meteorol.*, **146**:181–205, 2013.

- [98] S. Wharton and JK. Lundquist. Atmospheric stability affects wind turbine power collection. *Environ. Res. Lett.*, **7**:014005, 2012.
- [99] S. Wharton and JK. Lundquist. Assessing atmospheric stability and its impacts on rotor-disk wind characteristics at an onshore wind farm. *Wind Energy*, **15**:525–546, 2012.
- [100] BJ. Vanderwende and JK. Lundquist. The modification of wind turbine performance by statistically distinct atmospheric regimes. *Environ. Res. Lett.*, **7**:034035, 2012.
- [101] K. Bhaganagar and M. Debnath. Implications of stably stratified atmospheric boundary layer turbulence on the near-wake structure of wind turbines. *Energies*, **7**:5740–5763, 2014.
- [102] K. Bhaganagar and M. Debnath. The effects of mean atmospheric forcings of the stable atmospheric boundary layer on wind turbine wake. *J. Renewable Sustainable Energy*, **7**:013124, 2015.
- [103] M. Abkar and F. Porté-Agel. Influence of atmospheric stability on wind-turbine wakes: A large-eddy simulation study. *Phys. Fluids*, **27**:035104, 2015.
- [104] H. Lu and F. Porté-Agel. On the impact of wind farms on a convective atmospheric boundary layer. *Boundary-Layer Meteorol.*, DOI: 10.1007/s10546-015-0049-1, 2015.
- [105] N. Ghaisas, CL. Archer, and S. Xie. Evaluation of layout and atmospheric stability effects in wind farms using large-eddy simulation. *submitted to Renew. Energ.*, 2015.
- [106] R.J. Beare, MK. MacVean, AAM. Holtslag, J. Cuxart, I. Esau, JC. Golaz, MA. Jimenez, M. Khairoutdinov, B. Kosovic, D. Lewellen, TS. Lund, JK. Lundquist,

- A. McCabe, AF. Moene, Y. Noh, S. Raasch, and P. Sullivan. An intercomparison of large-eddy simulations of the stable boundary layer. *Boundary-Layer Meteorol.*, **118**:247–272, 2006.
- [107] R. Stoll and F. Porté-Agel. Large-eddy simulation of the stable atmospheric boundary layer using dynamic models with different averaging schemes. *Boundary-Layer Meteorol.*, **126**((1)):1–28, 2008.
- [108] S. Basu and F. Porté-Agel. Large-eddy simulation of stably stratified atmospheric boundary layer turbulence: a scale-dependent dynamic modeling approach. *J. Atmos. Sci.*, **63**:2074–2091, 2006.
- [109] SP. Arya. *Introduction to micrometeorology*. Academic Press, 2001.
- [110] CH. Moeng and PP. Sullivan. A Comparison of Shear- and Buoyancy-Driven Planetary Boundary Layer Flows. *J. Atmos. Sci.*, **51**:999–1022, 1994.
- [111] PP. Sullivan, JC. McWilliams, and CH. Moeng. A subgrid-scale model for large-eddy simulation of planetary boundary-layer flows. *Boundary-Layer Meteorol.*, **71**:247–276, 1994.
- [112] B. Koren. A robust upwind discretization method for advection, diffusion and source terms. *Notes Numer. Fluid Mech.*, **45**:117–138, 1993.
- [113] S. Raasch and D. Etling. Numerical simulations of rotating turbulent thermal convection. *Beitr. Phys. Atmos.*, **64**:185–199, 1991.
- [114] S. Raasch and M. Schröter. Palm—a large-eddy simulation model performing on massively parallel computers. *Meteorol. Z.*, **10**:363–372, 2001.
- [115] B. Kosovic. Subgrid-scale modelling for the large-eddy simulation of high-reynolds-number boundary layers. *J. Fluid Mech.*, **336**:151–182, 1997.

- [116] J. Cuxart, P. Bougeault, and JL. Redelsperger. A turbulence scheme allowing for mesoscale and large-eddy simulations. *Quart. J. Roy. Meteorol. Soc.*, **126**:1–30, 2000.
- [117] JWM. Cuijpers and PG. Duynkerke. Large eddy simulation of trade wind cumulus clouds. *J. Atmos. Sci.*, **50**:3894–3908, 1993.
- [118] A. Dosio, JVG. de Arellano, AAM. Holtslag, and PJH. Builtjes. Dispersion of a passive tracer in buoyancy- and shear-driven boundary layers. *J. Appl. Meteorol.*, **42**:1116–1130, 2003.
- [119] AR. Brown, SH. Derbyshire, and PJ. Mason. Large-eddy simulation of stable atmospheric boundary layers with a revised stochastic subgrid model. *Quart. J. Roy. Meteorol. Soc.*, **120**:1485–1512, 1994.
- [120] RJ. Beare and MK. MacVean. Resolution sensitivity and scaling of large-eddy simulations of the stable boundary layer. *Boundary-Layer Meteorol.*, **112**:257–281, 2004.
- [121] FTM. Nieuwstadt. The turbulent structure of the stable, nocturnal boundary layer. *J. Atmos. Sci.*, **41**:2202–2216, 1984.
- [122] JCR. Hunt, A. Wray, and P. Moin. Eddies, stream, and convergence zones in turbulent flows. Technical Report CTR-S88, Center for Turbulence Research, Stanford University, 1988.
- [123] G. Haller. An objective definition of a vortex. *J. Fluid Mech.*, **525**:126, 2005.
- [124] J. Jeong and F Hussain. On the identification of a vortex. *J. Fluid Mech.*, **285**:69–94, 1995.
- [125] PJ. Diamessis, GR. Spedding, and JA. Domaradzki. Similarity scaling and vorticity structure in high-Reynolds-number stably stratified turbulent wakes. *J. Fluid Mech.*, **671**:52–95, 2011.

- [126] ND. Sandham and L. Kleiser. The late stages of transition to turbulence in channel flow. *J. Fluid Mech.*, **245**:319–348, 1992.

## Appendix A

### DYNAMIC SGS MODELS

#### A.1 Planar-averaged scale-invariant (PASI) SGS model

Germano's identity can be written as

$$L_{ij} = \overline{\widetilde{u}_i \widetilde{u}_j} - \widetilde{u}_i \widetilde{u}_j = T_{ij} - \bar{\tau}_{ij}, \quad (\text{A.1})$$

where  $\overline{(\cdot)}$  denotes a test filtering with filter width of  $\bar{\Delta} = \alpha\Delta$  and  $\alpha$  is usually taken as 2;  $L_{ij}$  is the resolved stress; and  $T_{ij} = \overline{\widetilde{u}_i \widetilde{u}_j} - \widetilde{u}_i \widetilde{u}_j$  is the SGS stress at the test filter scale. The Smagorinsky model is used for the deviatoric part of  $T_{ij}$  as follows,

$$T_{ij} - \frac{1}{3}T_{kk}\delta_{ij} = -2(C_S\alpha\Delta)^2|\widetilde{S}|\widetilde{S}_{ij}. \quad (\text{A.2})$$

Next Eqs. 2.3 and A.2 are substituted into Eq. A.1 to obtain the error

$$e_{ij} = L_{ij} - C_{S,\Delta}^2 M_{ij}, \quad (\text{A.3})$$

where

$$M_{ij} = 2\Delta^2 \left( \overline{|\widetilde{S}|\widetilde{S}_{ij}} - \alpha^2\beta|\widetilde{S}|\widetilde{S}_{ij} \right), \quad (\text{A.4})$$

and

$$\beta = C_{S,\alpha\Delta}^2 / C_{S,\Delta}^2. \quad (\text{A.5})$$

The parameter  $\beta$  is the ratio between the coefficients at the test filter scale and at the filter scale. By minimization of the error using a least-square approach, and assuming that  $\beta = 1$  (i.e.  $C_S$  is scale-invariant) [24], the Smagorinsky coefficient at the test filter scale is obtained as

$$C_S^2 = \frac{\langle L_{ij} M_{ij} \rangle}{\langle M_{ij} M_{ij} \rangle}, \quad (\text{A.6})$$

where  $\langle \cdot \rangle$  is a spatial average along the horizontal direction that eliminates numerical instability.

## A.2 Lagrangian-averaged scale-invariant (LASI) SGS model

On the basis of the PASI model, for general inhomogeneous turbulence where a spatial average is problematic, Meneveau et al. [28] developed a weighted Lagrangian time average along the fluid trajectory as follows

$$C_S^2 = \frac{\mathcal{J}_{LM}}{\mathcal{J}_{LM}}, \quad (\text{A.7})$$

with

$$\mathcal{J}_{LM} = \int_{-\infty}^t L_{ij} M_{ij}(\mathbf{x}(t'), t') W(t - t') dt' \quad (\text{A.8})$$

and

$$\mathcal{J}_{MM} = \int_{-\infty}^t M_{ij} M_{ij}(\mathbf{x}(t'), t') W(t - t') dt', \quad (\text{A.9})$$

where  $W(t - t') = (1/T)\exp((t - t')/T)$  is the weighting function and  $T$  is chosen as  $T = 1.5\Delta(\mathcal{J}_{LM}\mathcal{J}_{MM})^{-1/8}$ . The exponential form of  $W(t - t')$  allows using forward relaxation-transport equations to replace the backward time integrals as follows

$$\frac{D\mathcal{J}_{LM}}{Dt} = \frac{\partial\mathcal{J}_{LM}}{\partial t} + \tilde{\mathbf{u}} \cdot \mathcal{J}_{LM} = \frac{1}{T_\Delta}(L_{ij}M_{ij} - \mathcal{J}_{LM}) \quad (\text{A.10})$$

and

$$\frac{D\mathcal{J}_{MM}}{Dt} = \frac{\partial\mathcal{J}_{MM}}{\partial t} + \tilde{\mathbf{u}} \cdot \mathcal{J}_{MM} = \frac{1}{T_\Delta}(M_{ij}M_{ij} - \mathcal{J}_{MM}). \quad (\text{A.11})$$

By using first-order numerical time and space schemes, Eq. A.10 and A.11 can be solved easily and economically to update  $\mathcal{J}_{LM}$  and  $\mathcal{J}_{MM}$  at each timestep.

## A.3 Lagrangian-averaged scale-dependent (LASD) SGS model

The assumption of scale-invariance of  $C_S$ , i. e.  $\beta = 1$ , is questionable. Porté-Agel et al. [31] and Bou-Zeid et al. [32] introduced scale-dependent approaches by using a second test filter at scale  $\hat{\Delta} = \alpha^2\Delta$  to calculate  $\beta$  dynamically. Following the Bou-Zeid et al. approach, by applying the Germano identity and minimizing the error at the second test filter scale, the coefficient at this scale can be obtained as

$$C_{S,\alpha^2\Delta}^2 = \frac{\mathcal{J}_{QN}}{\mathcal{J}_{NN}}, \quad (\text{A.12})$$

where  $\mathcal{J}_{QN}$  and  $\mathcal{J}_{NN}$  are Lagrangian-averaged  $Q_{ij}N_{ij}$  and  $N_{ij}N_{ij}$ , respectively, and  $Q_{ij} = \widehat{u}_i\widehat{u}_j - \widetilde{u}_i\widetilde{u}_j$ ,  $N_{ij} = 2\Delta^2\left(|\widetilde{S}|\widetilde{S}_{ij} - \alpha^4\beta^2|\widehat{S}|\widehat{S}_{ij}\right)$ . Assuming that  $\beta$  is scale-invariant (this assumption is more reasonable than the scale-invariant assumption of  $C_S$ ), such that  $\beta = C_{S,\alpha^2\Delta}^2/C_{S,\alpha\Delta}^2 = C_{S,\alpha\Delta}^2/C_{S,\Delta}^2$ , implies that,

$$C_{S,\Delta}^2 = C_{S,\alpha\Delta}^2/\beta = \frac{\mathcal{J}_{LM}/\mathcal{J}_{MM}}{\left(\frac{\mathcal{J}_{QN}/\mathcal{J}_{MM}}{\mathcal{J}_{NN}/\mathcal{J}_{LM}}\right)}. \quad (\text{A.13})$$

#### A.4 Test and second test filters in the physical space

The spatial filtering to a variable  $f$  at location  $\mathbf{x}$  is defined as the following convolution form

$$\widetilde{f}(\mathbf{x}) = \int_{-\infty}^{+\infty} \widetilde{G}(\mathbf{x}, \mathbf{x}')f(\mathbf{x}')d\mathbf{x}', \quad (\text{A.14})$$

where  $\widetilde{G}$  is the filter kernel satisfying the property of

$$\int_{-\infty}^{+\infty} \widetilde{G}(\mathbf{x}, \mathbf{x}') = 1. \quad (\text{A.15})$$

Here, in conjunction with the finite-difference methods, two filters, i. e. box (or top-hat) filter and Gaussian filter, are tested for their simplicity and wide use in applications. Specifically, for a filter width  $\widetilde{\Delta}_i$ , the kernel of the 1D box filter is written as

$$\widetilde{G}(x_i - x'_i) = \begin{cases} \frac{1}{\widetilde{\Delta}_i}, & \text{if } |x_i - x'_i| \leq \frac{\widetilde{\Delta}_i}{2}; \\ 0, & \text{otherwise.} \end{cases} \quad (\text{A.16})$$

Note that in the finite-difference discretization, the box filtering is implicitly applied at the filter width of the grid spacing [52]. For the 1D Gaussian filter, the kernel is

$$\widetilde{G}(x_i - x'_i) = \left(\frac{\gamma}{\pi\widetilde{\Delta}_i^2}\right)^{1/2} \exp\left(\frac{-\gamma|x_i - x'_i|^2}{\widetilde{\Delta}_i^2}\right), \quad (\text{A.17})$$

where  $\gamma = 6$  is generally used [91, 61]. Here, the filtering is performed in a 2D manner along the horizontal directions in the physical space, i. e.

$$\widetilde{f}(\mathbf{x}) = \int_{-\infty}^{+\infty} \widetilde{G}(x_1 - x'_1)\widetilde{G}(x_2 - x'_2)f(\mathbf{x}')d\mathbf{x}'. \quad (\text{A.18})$$

Following previous finite-difference LES, the trapezoidal rule is used to calculate the discrete integral [27, 51, 52].

**Appendix B**  
**COPYRIGHT PERMISSION**

## SPRINGER LICENSE TERMS AND CONDITIONS

Jan 21, 2016

This is a License Agreement between SHENGBAI XIE ("You") and Springer ("Springer") provided by Copyright Clearance Center ("CCC"). The license consists of your order details, the terms and conditions provided by Springer, and the payment terms and conditions.

**All payments must be made in full to CCC. For payment instructions, please see information listed at the bottom of this form.**

License Number	3793750372506
License date	Jan 21, 2016
Licensed content publisher	Springer
Licensed content publication	Boundary Layer Meteorology
Licensed content title	Sensitivity Issues in Finite-Difference Large-Eddy Simulations of the Atmospheric Boundary Layer with Dynamic Subgrid-Scale Models
Licensed content author	Shengbai Xie
Licensed content date	Jan 1, 2015
Volume number	157
Issue number	3
Type of Use	Thesis/Dissertation
Portion	Full text
Number of copies	1
Author of this Springer article	Yes and you are the sole author of the new work
Order reference number	None
Title of your thesis / dissertation	A NUMERICAL STUDY OF WIND TURBINE WAKES UNDER VARIOUS ATMOSPHERIC STABILITY CONDITIONS
Expected completion date	Feb 2016
Estimated size(pages)	131
Total	0.00 USD
Terms and Conditions	

### Introduction

The publisher for this copyrighted material is Springer. By clicking "accept" in connection with completing this licensing transaction, you agree that the following terms and conditions apply to this transaction (along with the Billing and Payment terms and conditions established by Copyright Clearance Center, Inc. ("CCC"), at the time that you opened your Rightslink account and that are available at any time at <http://myaccount.copyright.com>).

### Limited License

With reference to your request to reuse material on which Springer controls the copyright, permission is granted for the use indicated in your enquiry under the following conditions:

- Licenses are for one-time use only with a maximum distribution equal to the number stated

in your request.

- Springer material represents original material which does not carry references to other sources. If the material in question appears with a credit to another source, this permission is not valid and authorization has to be obtained from the original copyright holder.

- This permission

- is non-exclusive

- is only valid if no personal rights, trademarks, or competitive products are infringed.

- explicitly excludes the right for derivatives.

- Springer does not supply original artwork or content.

- According to the format which you have selected, the following conditions apply accordingly:

- **Print and Electronic:** This License include use in electronic form provided it is password protected, on intranet, or CD-Rom/DVD or E-book/E-journal. It may not be republished in electronic open access.

- **Print:** This License excludes use in electronic form.

- **Electronic:** This License only pertains to use in electronic form provided it is password protected, on intranet, or CD-Rom/DVD or E-book/E-journal. It may not be republished in electronic open access.

For any electronic use not mentioned, please contact Springer at [permissions.springer@spi-global.com](mailto:permissions.springer@spi-global.com).

- Although Springer controls the copyright to the material and is entitled to negotiate on rights, this license is only valid subject to courtesy information to the author (address is given in the article/chapter).

- If you are an STM Signatory or your work will be published by an STM Signatory and you are requesting to reuse figures/tables/illustrations or single text extracts, permission is granted according to STM Permissions Guidelines: <http://www.stm-assoc.org/permissions-guidelines/>

For any electronic use not mentioned in the Guidelines, please contact Springer at [permissions.springer@spi-global.com](mailto:permissions.springer@spi-global.com). If you request to reuse more content than stipulated in the STM Permissions Guidelines, you will be charged a permission fee for the excess content.

Permission is valid upon payment of the fee as indicated in the licensing process. If permission is granted free of charge on this occasion, that does not prejudice any rights we might have to charge for reproduction of our copyrighted material in the future.

-If your request is for reuse in a Thesis, permission is granted free of charge under the following conditions:

This license is valid for one-time use only for the purpose of defending your thesis and with a maximum of 100 extra copies in paper. If the thesis is going to be published, permission needs to be reobtained.

- includes use in an electronic form, provided it is an author-created version of the thesis on his/her own website and his/her university's repository, including UMI (according to the definition on the Sherpa website: <http://www.sherpa.ac.uk/romeo/>);

- is subject to courtesy information to the co-author or corresponding author.

Geographic Rights: Scope

Licenses may be exercised anywhere in the world.

Altering/Modifying Material: Not Permitted

Figures, tables, and illustrations may be altered minimally to serve your work. You may not alter or modify text in any manner. Abbreviations, additions, deletions and/or any other alterations shall be made only with prior written authorization of the author(s).

Reservation of Rights

Springer reserves all rights not specifically granted in the combination of (i) the license details provided by you and accepted in the course of this licensing transaction and (ii) these terms and conditions and (iii) CCC's Billing and Payment terms and conditions.

#### License Contingent on Payment

While you may exercise the rights licensed immediately upon issuance of the license at the end of the licensing process for the transaction, provided that you have disclosed complete and accurate details of your proposed use, no license is finally effective unless and until full payment is received from you (either by Springer or by CCC) as provided in CCC's Billing and Payment terms and conditions. If full payment is not received by the date due, then any license preliminarily granted shall be deemed automatically revoked and shall be void as if never granted. Further, in the event that you breach any of these terms and conditions or any of CCC's Billing and Payment terms and conditions, the license is automatically revoked and shall be void as if never granted. Use of materials as described in a revoked license, as well as any use of the materials beyond the scope of an unrevoked license, may constitute copyright infringement and Springer reserves the right to take any and all action to protect its copyright in the materials.

#### Copyright Notice: Disclaimer

You must include the following copyright and permission notice in connection with any reproduction of the licensed material:

"Springer book/journal title, chapter/article title, volume, year of publication, page, name(s) of author(s), (original copyright notice as given in the publication in which the material was originally published) "With permission of Springer"

In case of use of a graph or illustration, the caption of the graph or illustration must be included, as it is indicated in the original publication.

#### Warranties: None

Springer makes no representations or warranties with respect to the licensed material and adopts on its own behalf the limitations and disclaimers established by CCC on its behalf in its Billing and Payment terms and conditions for this licensing transaction.

#### Indemnity

You hereby indemnify and agree to hold harmless Springer and CCC, and their respective officers, directors, employees and agents, from and against any and all claims arising out of your use of the licensed material other than as specifically authorized pursuant to this license.

#### No Transfer of License

This license is personal to you and may not be sublicensed, assigned, or transferred by you without Springer's written permission.

#### No Amendment Except in Writing

This license may not be amended except in a writing signed by both parties (or, in the case of Springer, by CCC on Springer's behalf).

#### Objection to Contrary Terms

Springer hereby objects to any terms contained in any purchase order, acknowledgment, check endorsement or other writing prepared by you, which terms are inconsistent with these terms and conditions or CCC's Billing and Payment terms and conditions. These terms and conditions, together with CCC's Billing and Payment terms and conditions (which are incorporated herein), comprise the entire agreement between you and Springer (and CCC) concerning this licensing transaction. In the event of any conflict between your obligations established by these terms and conditions and those established by CCC's Billing and Payment terms and conditions, these terms and conditions shall control.

#### Jurisdiction

All disputes that may arise in connection with this present License, or the breach thereof,

shall be settled exclusively by arbitration, to be held in the Federal Republic of Germany, in accordance with German law.

V 12AUG2015

**Questions? [customercare@copyright.com](mailto:customercare@copyright.com) or +1-855-239-3415 (toll free in the US) or +1-978-646-2777.**

---

---

## JOHN WILEY AND SONS LICENSE TERMS AND CONDITIONS

Jan 21, 2016

This Agreement between SHENGBAI XIE ("You") and John Wiley and Sons ("John Wiley and Sons") consists of your license details and the terms and conditions provided by John Wiley and Sons and Copyright Clearance Center.

License Number	3793741285261
License date	Jan 21, 2016
Licensed Content Publisher	John Wiley and Sons
Licensed Content Publication	Wind Energy
Licensed Content Title	Self-similarity and turbulence characteristics of wind turbine wakes via large-eddy simulation
Licensed Content Author	Shengbai Xie,Cristina Archer
Licensed Content Date	Aug 18, 2014
Pages	24
Type of use	Dissertation/Thesis
Requestor type	Author of this Wiley article
Format	Electronic
Portion	Full article
Will you be translating?	No
Title of your thesis / dissertation	A NUMERICAL STUDY OF WIND TURBINE WAKES UNDER VARIOUS ATMOSPHERIC STABILITY CONDITIONS
Expected completion date	Feb 2016
Expected size (number of pages)	131
Requestor Location	SHENGBAI XIE 5994 Schroeder Rd Apt D  MADISON, WI 53711 United States Attn: SHENGBAI XIE
Billing Type	Invoice
Billing Address	SHENGBAI XIE 5994 Schroeder Rd Apt D  MADISON, WI 53711 United States Attn: SHENGBAI XIE
Total	0.00 USD
Terms and Conditions	

## TERMS AND CONDITIONS

This copyrighted material is owned by or exclusively licensed to John Wiley & Sons, Inc. or one of its group companies (each a "Wiley Company") or handled on behalf of a society with which a Wiley Company has exclusive publishing rights in relation to a particular work (collectively "WILEY"). By clicking "accept" in connection with completing this licensing transaction, you agree that the following terms and conditions apply to this transaction (along with the billing and payment terms and conditions established by the Copyright Clearance Center Inc., ("CCC's Billing and Payment terms and conditions"), at the time that you opened your RightsLink account (these are available at any time at <http://myaccount.copyright.com>).

### Terms and Conditions

- The materials you have requested permission to reproduce or reuse (the "Wiley Materials") are protected by copyright.
- You are hereby granted a personal, non-exclusive, non-sub licensable (on a stand-alone basis), non-transferable, worldwide, limited license to reproduce the Wiley Materials for the purpose specified in the licensing process. This license, **and any CONTENT (PDF or image file) purchased as part of your order**, is for a one-time use only and limited to any maximum distribution number specified in the license. The first instance of republication or reuse granted by this license must be completed within two years of the date of the grant of this license (although copies prepared before the end date may be distributed thereafter). The Wiley Materials shall not be used in any other manner or for any other purpose, beyond what is granted in the license. Permission is granted subject to an appropriate acknowledgement given to the author, title of the material/book/journal and the publisher. You shall also duplicate the copyright notice that appears in the Wiley publication in your use of the Wiley Material. Permission is also granted on the understanding that nowhere in the text is a previously published source acknowledged for all or part of this Wiley Material. Any third party content is expressly excluded from this permission.
- With respect to the Wiley Materials, all rights are reserved. Except as expressly granted by the terms of the license, no part of the Wiley Materials may be copied, modified, adapted (except for minor reformatting required by the new Publication), translated, reproduced, transferred or distributed, in any form or by any means, and no derivative works may be made based on the Wiley Materials without the prior permission of the respective copyright owner. **For STM Signatory Publishers clearing permission under the terms of the [STM Permissions Guidelines](#) only, the terms of the license are extended to include subsequent editions and for editions in other languages, provided such editions are for the work as a whole in situ and does not involve the separate exploitation of the permitted figures or extracts**, You may not alter, remove or suppress in any manner any copyright, trademark or other notices displayed by the Wiley Materials. You may not license, rent, sell, loan, lease, pledge, offer as security, transfer or assign the Wiley Materials on a stand-alone basis, or any of the rights granted to you hereunder to any other person.
- The Wiley Materials and all of the intellectual property rights therein shall at all times remain the exclusive property of John Wiley & Sons Inc, the Wiley Companies, or their respective licensors, and your interest therein is only that of having possession of and the right to reproduce the Wiley Materials pursuant to Section 2 herein during the

continuance of this Agreement. You agree that you own no right, title or interest in or to the Wiley Materials or any of the intellectual property rights therein. You shall have no rights hereunder other than the license as provided for above in Section 2. No right, license or interest to any trademark, trade name, service mark or other branding ("Marks") of WILEY or its licensors is granted hereunder, and you agree that you shall not assert any such right, license or interest with respect thereto

- NEITHER WILEY NOR ITS LICENSORS MAKES ANY WARRANTY OR REPRESENTATION OF ANY KIND TO YOU OR ANY THIRD PARTY, EXPRESS, IMPLIED OR STATUTORY, WITH RESPECT TO THE MATERIALS OR THE ACCURACY OF ANY INFORMATION CONTAINED IN THE MATERIALS, INCLUDING, WITHOUT LIMITATION, ANY IMPLIED WARRANTY OF MERCHANTABILITY, ACCURACY, SATISFACTORY QUALITY, FITNESS FOR A PARTICULAR PURPOSE, USABILITY, INTEGRATION OR NON-INFRINGEMENT AND ALL SUCH WARRANTIES ARE HEREBY EXCLUDED BY WILEY AND ITS LICENSORS AND WAIVED BY YOU.
- WILEY shall have the right to terminate this Agreement immediately upon breach of this Agreement by you.
- You shall indemnify, defend and hold harmless WILEY, its Licensors and their respective directors, officers, agents and employees, from and against any actual or threatened claims, demands, causes of action or proceedings arising from any breach of this Agreement by you.
- IN NO EVENT SHALL WILEY OR ITS LICENSORS BE LIABLE TO YOU OR ANY OTHER PARTY OR ANY OTHER PERSON OR ENTITY FOR ANY SPECIAL, CONSEQUENTIAL, INCIDENTAL, INDIRECT, EXEMPLARY OR PUNITIVE DAMAGES, HOWEVER CAUSED, ARISING OUT OF OR IN CONNECTION WITH THE DOWNLOADING, PROVISIONING, VIEWING OR USE OF THE MATERIALS REGARDLESS OF THE FORM OF ACTION, WHETHER FOR BREACH OF CONTRACT, BREACH OF WARRANTY, TORT, NEGLIGENCE, INFRINGEMENT OR OTHERWISE (INCLUDING, WITHOUT LIMITATION, DAMAGES BASED ON LOSS OF PROFITS, DATA, FILES, USE, BUSINESS OPPORTUNITY OR CLAIMS OF THIRD PARTIES), AND WHETHER OR NOT THE PARTY HAS BEEN ADVISED OF THE POSSIBILITY OF SUCH DAMAGES. THIS LIMITATION SHALL APPLY NOTWITHSTANDING ANY FAILURE OF ESSENTIAL PURPOSE OF ANY LIMITED REMEDY PROVIDED HEREIN.
- Should any provision of this Agreement be held by a court of competent jurisdiction to be illegal, invalid, or unenforceable, that provision shall be deemed amended to achieve as nearly as possible the same economic effect as the original provision, and the legality, validity and enforceability of the remaining provisions of this Agreement shall not be affected or impaired thereby.
- The failure of either party to enforce any term or condition of this Agreement shall not constitute a waiver of either party's right to enforce each and every term and condition of this Agreement. No breach under this agreement shall be deemed waived or

excused by either party unless such waiver or consent is in writing signed by the party granting such waiver or consent. The waiver by or consent of a party to a breach of any provision of this Agreement shall not operate or be construed as a waiver of or consent to any other or subsequent breach by such other party.

- This Agreement may not be assigned (including by operation of law or otherwise) by you without WILEY's prior written consent.
- Any fee required for this permission shall be non-refundable after thirty (30) days from receipt by the CCC.
- These terms and conditions together with CCC's Billing and Payment terms and conditions (which are incorporated herein) form the entire agreement between you and WILEY concerning this licensing transaction and (in the absence of fraud) supersedes all prior agreements and representations of the parties, oral or written. This Agreement may not be amended except in writing signed by both parties. This Agreement shall be binding upon and inure to the benefit of the parties' successors, legal representatives, and authorized assigns.
- In the event of any conflict between your obligations established by these terms and conditions and those established by CCC's Billing and Payment terms and conditions, these terms and conditions shall prevail.
- WILEY expressly reserves all rights not specifically granted in the combination of (i) the license details provided by you and accepted in the course of this licensing transaction, (ii) these terms and conditions and (iii) CCC's Billing and Payment terms and conditions.
- This Agreement will be void if the Type of Use, Format, Circulation, or Requestor Type was misrepresented during the licensing process.
- This Agreement shall be governed by and construed in accordance with the laws of the State of New York, USA, without regards to such state's conflict of law rules. Any legal action, suit or proceeding arising out of or relating to these Terms and Conditions or the breach thereof shall be instituted in a court of competent jurisdiction in New York County in the State of New York in the United States of America and each party hereby consents and submits to the personal jurisdiction of such court, waives any objection to venue in such court and consents to service of process by registered or certified mail, return receipt requested, at the last known address of such party.

## **WILEY OPEN ACCESS TERMS AND CONDITIONS**

Wiley Publishes Open Access Articles in fully Open Access Journals and in Subscription journals offering Online Open. Although most of the fully Open Access journals publish open access articles under the terms of the Creative Commons Attribution (CC BY) License only, the subscription journals and a few of the Open Access Journals offer a choice of Creative Commons Licenses. The license type is clearly identified on the article.

### **The Creative Commons Attribution License**

The [Creative Commons Attribution License \(CC-BY\)](#) allows users to copy, distribute and transmit an article, adapt the article and make commercial use of the article. The CC-BY

license permits commercial and non-

### **Creative Commons Attribution Non-Commercial License**

The [Creative Commons Attribution Non-Commercial \(CC-BY-NC\) License](#) permits use, distribution and reproduction in any medium, provided the original work is properly cited and is not used for commercial purposes.(see below)

### **Creative Commons Attribution-Non-Commercial-NoDerivs License**

The [Creative Commons Attribution Non-Commercial-NoDerivs License](#) (CC-BY-NC-ND) permits use, distribution and reproduction in any medium, provided the original work is properly cited, is not used for commercial purposes and no modifications or adaptations are made. (see below)

### **Use by commercial "for-profit" organizations**

Use of Wiley Open Access articles for commercial, promotional, or marketing purposes requires further explicit permission from Wiley and will be subject to a fee.

Further details can be found on Wiley Online Library

<http://olabout.wiley.com/WileyCDA/Section/id-410895.html>

### **Other Terms and Conditions:**

**v1.10 Last updated September 2015**

**Questions? [customercare@copyright.com](mailto:customercare@copyright.com) or +1-855-239-3415 (toll free in the US) or +1-978-646-2777.**